Prepared in cooperation with the Florida Flood Hub for Applied Research and Innovation

# Development of Projected Depth-Duration-Frequency Curves for Precipitation in Florida, 2020–59 and 2050–89

Scientific Investigations Report 2025–5111

**U.S. Department of the Interior**
**U.S. Geological Survey**

**Cover.** Chipola River, Florida, in flood on July 10, 2013. Photograph by Alan Cressler (U.S. Geological Survey, retired).

# Development of Projected Depth-Duration-Frequency Curves for Precipitation in Florida, 2020–59 and 2050–89

By Michelle M. Irizarry-Ortiz

Prepared in cooperation with the Florida Flood Hub for Applied Research and Innovation

Scientific Investigations Report 2025–5111

**U.S. Department of the Interior**
**U.S. Geological Survey**

U.S. Geological Survey, Reston, Virginia: 2026

Suggested citation:
Irizarry-Ortiz, M.M., 2026, Development of projected depth-duration-frequency curves for precipitation in Florida, 2020–59 and 2050–89: U.S. Geological Survey Scientific Investigations Report 2025–5111, 75 p., https://doi.org/10.3133/sir20255111.

Associated data for this publication:
Irizarry-Ortiz, M.M., and Haider, S.M., 2023, Change factors to derive projected future precipitation depth-duration-frequency (DDF) curves at 242 National Oceanic and Atmospheric Administration (NOAA) Atlas 14 stations in Florida (ver. 3.0, August 2025): U.S. Geological Survey data release, https://doi.org/10.5066/P9Q3LEIL.

ISSN 2328-0328 (online)

# Acknowledgments

The author gratefully acknowledges the Florida Flood Hub for Applied Research and Innovation for its cooperation, technical input, and for providing data and funding for this project. The South Florida Water Management District and the Sea Level Solutions Center in the Institute of Environment at Florida International University are also thanked for collaborating on this project.

The World Climate Research Programmer’s Working Group on Coupled Modelling, which is responsible for the Coupled Model Intercomparison Project (CMIP), is acknowledged for CMIP5 datasets, and the climate modeling groups (listed in the data release associated with this report; Irizarry-Ortiz and Haider, 2023) are thanked for producing and making available their model output. For the Coupled Model Intercomparison Project, the U.S. Department of Energy's Program for Climate Model Diagnosis and Intercomparison provides coordinating support and led development of software infrastructure in partnership with the Global Organization for Earth System Science Portals. The Multivariate Adaptive Constructed Analogs dataset MACAv2-LIVNEH was produced under the Northwest Climate Adaptation Science Center U.S. Geological Survey (USGS) Grant Number G12AC20495. The dataset MACAv2-METDATA was produced with funding from the Regional Approaches to Climate Change project and the Southeast Climate Science Center. The U.S. Department of Defense Environmental Security Technology Certification Program is acknowledged for its support of the North America Coordinated Regional Downscaling Experiment data archive. The author is also grateful to Jupiter Intelligence (https://www.jupiterintel.com) for providing the files and methodology necessary for implementing their analog resampling and statistical scaling method. The author is grateful to the University of California San Diego for providing data from the Localized Constructed Analogs downscaled climate dataset.

The author acknowledges the World Climate Research Programme, which, through its Working Group on Coupled Modelling, coordinated and promoted CMIP6. The climate modeling groups are thanked for producing and making available their model output, the Earth System Grid Federation (ESGF) for archiving the data and providing access, and the multiple funding agencies who support CMIP6 and ESGF. Climate scenarios used were from the National Aeronautics and Space Administration Earth Exchange Global Daily Downscaled Projections (NEX-GDDP) CMIP6 dataset, prepared by the Climate Analytics Group and National Aeronautics and Space Administration (NASA) Ames Research Center using the NASA Earth Exchange and distributed by the NASA Center for Climate Simulation (NCCS).

The author is grateful to the USGS Advanced Research Computing team for providing access to the Denali supercomputer, which was used for running most of the R code used in this project. Finally, many thanks to two reviewers, Anupama John of Florida International University and Saira Haider of the USGS, for providing useful comments and suggestions when reviewing this manuscript.

## Contents

## Figures

## Tables

## Conversion Factors

U.S. customary units to International System of Units

| Multiply | By | To obtain |
|---|---|---|
| | **Length** | |
| inch (in.) | 2.54 | centimeter (cm) |
| inch (in.) | 25.4 | millimeter (mm) |
| mile (mi) | 1.609 | kilometer (km) |
| | **Area** | |
| acre | 0.004047 | square kilometer ($km^2$) |
| square mile ($mi^2$) | 2.590 | square kilometer ($km^2$) |
| | **Flow rate** | |
| inch per month (in/mo) | 25.4 | millimeter per month (mm/mo) |

International System of Units to U.S. customary units

| Multiply | By | To obtain |
|---|---|---|
| | **Length** | |
| millimeter (mm) | 0.03937 | inch (in.) |
| centimeter (cm) | 0.3937 | inch (in.) |
| kilometer (km) | 0.6214 | mile (mi) |
| | **Area** | |
| square kilometer ($km^2$) | 247.1 | acre |
| square kilometer ($km^2$) | 0.3861 | square mile ($mi^2$) |
| | **Flow rate** | |
| millimeter per month (mm/mo) | 0.03937 | inch per month (in/mo) |

Temperature in degrees Celsius (°C) may be converted to degrees Fahrenheit (°F) as follows: °F = (1.8 × °C) + 32.

Temperature in degrees Fahrenheit (°F) may be converted to degrees Celsius (°C) as follows: °C = (°F – 32) / 1.8.

## Datum

Horizontal coordinate information is referenced to the World Geodetic System 1984 (WGS84) datum.

## Supplemental Information

Precipitation depth totals are given in inches (in.), and precipitation intensities are given in inches per day (in/d).

# Abbreviations

| | |
|---|---|
| AEP | annual exceedance probability |
| AIC | Akaike Information Criterion |
| ARF | areal reduction factor |
| BCCA | Bias-Corrected Constructed Analog |
| BCSD | Bias-Correction Spatial Disaggregation |
| CDD | cumulative dry days |
| CDF | cumulative distribution function |
| CDO | Climate Data Operators |
| CIDA | Center for Data Analytics |
| CMIP5 | Coupled Model Intercomparison Project Phase 5 |
| CMIP6 | Coupled Model Intercomparison Project Phase 6 |
| CML | constrained maximum likelihood |
| CORDEX | Coordinated Regional Downscaling Experiment |
| DDF | depth-duration-frequency |
| ETCCDI | Expert Team on Climate Change Detection and Indices |
| EVT | extreme value theory |
| GCM | general circulation model |
| GHG | greenhouse gas |
| GMFD | Global Meteorological Forcing Dataset |
| GOF | goodness-of-fit |
| GP | generalized Pareto |
| IPCC | Intergovernmental Panel on Climate Change |
| IVSS | interannual variability skill score |
| JupiterWRF | Jupiter Intelligence Weather Research and Forecasting model |
| KACF | Kendall autocorrelation coefficient |
| LOCA | Localized Constructed Analogs |
| LOCA2 | Localized Constructed Analogs version 2 |
| MACA | Multivariate Adaptive Constructed Analogs |
| MCI | Model Climatology Index |
| MK | Mann-Kendall trend test |
| ML | maximum likelihood |
| MQDM | multiplicative quantile delta mapping |
| MVI | Model Variability Index |
| NA-CORDEX | North American Coordinated Regional Downscaling Experiment |

| | |
|---|---|
| NASA | National Aeronautics and Space Administration |
| NCAR | National Center for Atmospheric Research |
| NEX-GDDP | National Aeronautics and Space Administration Earth Exchange Global Daily Downscaled Projections |
| NKN | Northwest Knowledge Network |
| NOAA | National Oceanic and Atmospheric Administration |
| PDS | partial-duration series |
| POT | peaks-over-threshold |
| PRCTOT | annual total wet day precipitation |
| PRISM | Parameter-elevation Regressions on Independent Slopes Model |
| RCM | regional climate model |
| RCP | representative concentration pathway |
| RMSE | root-mean-square error |
| SFWMD | South Florida Water Management District |
| SSP | shared socioeconomic pathway |
| USGS | U.S. Geological Survey |
| WRF | Weather Research and Forecasting model |

# Development of Projected Depth-Duration-Frequency Curves for Precipitation in Florida, 2020–59 and 2050–89

By Michelle M. Irizarry-Ortiz

## Abstract

The planning, permitting, and design of stormwater-management projects require estimates of the depths of extreme precipitation for current and future events with specified durations and return periods. In this project, precipitation data from six downscaled climate datasets were used to determine changes in precipitation depth-duration-frequency curves from the period 1966–2005 to the periods 2020–59 and 2050–89. The downscaled climate datasets are from the Coupled Model Intercomparison Project Phases 5 and 6 and include (1) Coordinated Regional Downscaling Experiment (CORDEX), (2) Localized Constructed Analogs (LOCA), (3) Multivariate Adaptive Constructed Analogs (MACA), (4) Jupiter Intelligence Weather Research and Forecasting model (JupiterWRF), (5) LOCA version 2 (LOCA2), and (6) National Aeronautics and Space Administration Earth Exchange Global Daily Downscaled Projections (NEX-GDDP). Change factors—multiplicative changes in expected extreme precipitation magnitude from a historical to future period—were computed for grid cells containing National Oceanic and Atmospheric Administration Atlas 14 stations in Florida. Change factors for specific durations and return periods were developed to scale the National Oceanic and Atmospheric Administration Atlas 14 historical depth-duration-frequency values to the periods 2020–59 and 2050–89 on the basis of changes in extreme precipitation derived from six downscaled climate datasets.

Overall, a large variation in change factors across downscaled climate datasets was found, with change factors generally being greater than 1 and increasing with return period. In general, median change factors were found to range within 1.01–1.58 for 2020–59 and 1.01–1.63 for 2050–89, depending on the downscaled climate dataset, region, duration, and return period, indicating a projected overall increase in future extreme-precipitation events. When data from all datasets are considered together, median change factors range within 1.04–1.18 for the period 2020–59 and within 1.04–1.23 for the period 2050–89, depending on the region, duration, and return period. Spatial patterns in median change factors were found to vary by dataset.

## Introduction

The planning, permitting, and design of stormwater-management projects require estimates of current and future precipitation amounts, expressed as depths, for specified return periods and durations. Water management districts across the State of Florida have published permitting manuals (for example, South Florida Water Management District [SFWMD], 2016; St. Johns River Water Management District, 2018), which contain specific descriptions of precipitation-depth estimates for various return periods and durations. Precipitation-depth estimates are used to quantify extreme events, such as an event that has a 1-percent chance of being equaled or exceeded in a given year, alternatively referred to as a “100-year return period.” Precipitation events are also defined by the time period over which the event is measured, such as the total precipitation accrued over a 1-, or 3-, or 7-day window of time, alternatively referred to as the “duration” of the event. One- and multi-day design storms (storms used in infrastructure design) of various return periods are published in State permitting manuals or in Federal documents such as the National Oceanic and Atmospheric Administration (NOAA) Atlas 14, volume 9, which covers the southeastern United States, including Florida (Perica and others, 2013). This publication and the stations used in the analysis are herein referred to as “NOAA Atlas 14.” These design storms have traditionally been derived by applying statistical methods to historical weather-station data that may or may not reflect extreme events occurring in more recent decades.

Flood vulnerability is affected by changes in precipitation, both extremes and duration of events that affect antecedent conditions, and the resulting changes to the hydrologic cycle. Other factors affecting flood vulnerability include changes in sea level, land use and land cover, and the presence and management of flood control infrastructure (Cardona and others, 2012; Seneviratne and others, 2012; Decker and others, 2019; Barnard and others, 2024). Florida Senate Bill 1954 (2021) (Florida Senate, 2021) titled “Statewide Flooding and Sea Level Rise Resilience” established the Florida Flood Hub for Applied Research and Innovation at the University of South Florida College of Marine Science and charged it with developing a statewide flood-vulnerability assessment. In addition to sea-level rise scenarios, the vulnerability assessment requires information about potential changes in future precipitation patterns. This information may be used to drive advanced integrated hydrologic and hydraulic models to translate future projected changes in climate, sea level, and land development into flood-vulnerability maps. To help address the needs of the flood-vulnerability assessments, the U.S. Geological Survey (USGS) and the Florida Flood Hub for Applied Research and Innovation are cooperating on a study to develop depth-duration-frequency (DDF) curves for precipitation that incorporate projections of future climate change across relevant greenhouse-gas (GHG) emission scenarios. Irizarry-Ortiz and others (2022) report factors influencing precipitation extremes in southern Florida, projected changes in these extremes, and previous DDF-curve development efforts for the State of Florida; this report expands these analyses to the entire State of Florida. The study area is shown in figure 1.

## Purpose and Scope

This report documents the development of projected DDF curves for precipitation for the State of Florida, for the periods 2020–59 and 2050–89. Hereinafter, precipitation will be implied when referring to DDF curves. As part of this study, an ensemble method was used to determine median change factors for precipitation depths as well as intermodel variability at locations throughout Florida. Change factors were determined for durations of 1, 3, and 7 days, and return periods of 5, 10, 25, 50, 100, 200, and 500 years. The 7-day duration was included to capture potential future changes in precipitation at the multiday timescale, such as high precipitation caused by stalling storms. Change factors were computed from DDF curves fit to precipitation data from six downscaled climate datasets for two 40-year periods representing future projected climate for the periods 2020–59 (centered on 2040) or 2050–89 (centered on 2070), and historical (retrospective) climate for 1966–2005 for the study area. Change factors were derived from four datasets that downscale models from the Coupled Model Intercomparison Project Phase 5 (CMIP5; Taylor and others, 2012):

- Coordinated Regional Downscaling Experiment (CORDEX; Giorgi and others, 2009; Mearns and others, 2017),
- Localized Constructed Analogs (LOCA; Pierce and others, 2014),
- Multivariate Adaptive Constructed Analogs (MACA; Abatzoglou and Brown, 2012), and
- Jupiter Intelligence Weather Research and Forecasting model (JupiterWRF; Jupiter Intelligence, 2021).

Change factors were also derived from two datasets that downscale models from the Coupled Model Intercomparison Project Phase 6 (CMIP6; Eyring and others, 2016):

- LOCA version 2 (LOCA2; Pierce and others, 2023), and
- National Aeronautics and Space Administration (NASA) Earth Exchange Global Daily Downscaled Projections (NEX-GDDP; Thrasher and others, 2021, 2022)

The CMIP6 historical simulations end in 2014; however, the common historical period 1966–2005 was used as the reference period for change factor computation for both CMIP5 and CMIP6 downscaled climate datasets. In summary, a total of six downscaled datasets (CORDEX, LOCA, MACA, JupiterWRF, LOCA2, and NEX-GDDP) were used to compute change factors.

Perica and others (2013) derived historical DDF curves from historical observations at meteorological stations in Florida, which are published in NOAA Atlas 14. The DDF curves based on partial-duration series (PDS) from NOAA can be multiplied by the change factors derived in this study to determine potential future extreme precipitation depths for events of a given duration and return period for time periods centered on 2040 and 2070.

## Terminology Used in This Report

In describing our processing and analysis, the definitions of several terms are important to clarify. In this report, the term “reanalysis” is used to refer to dynamical climate model simulations that are based on observed boundary conditions and are meant to match observed weather as precisely as possible. General circulation models (GCMs) broadly refer to global-scale dynamical climate models that are coupled atmosphere-ocean general circulation models or Earth systems models, such as used in CMIP5 and CMIP6 studies. The term “historical observations” is used to refer to weather observations used in statistical downscaling. The term “historical simulations” is used to refer to GCM and associated downscaled models that are tuned to preindustrial conditions (around 1850 or 1750 depending on reference; see Schurer and others, 2017, for a discussion) and possibly to more recent historical conditions (Mauritsen and others, 2012; Hourdin and others, 2017) but are otherwise not constrained to precisely match daily weather conditions from 1850 to the present. The term “future projections” refers to those by GCMs and associated downscaled models of future climate that assume a specific GHG emission scenario or concentration trajectory.

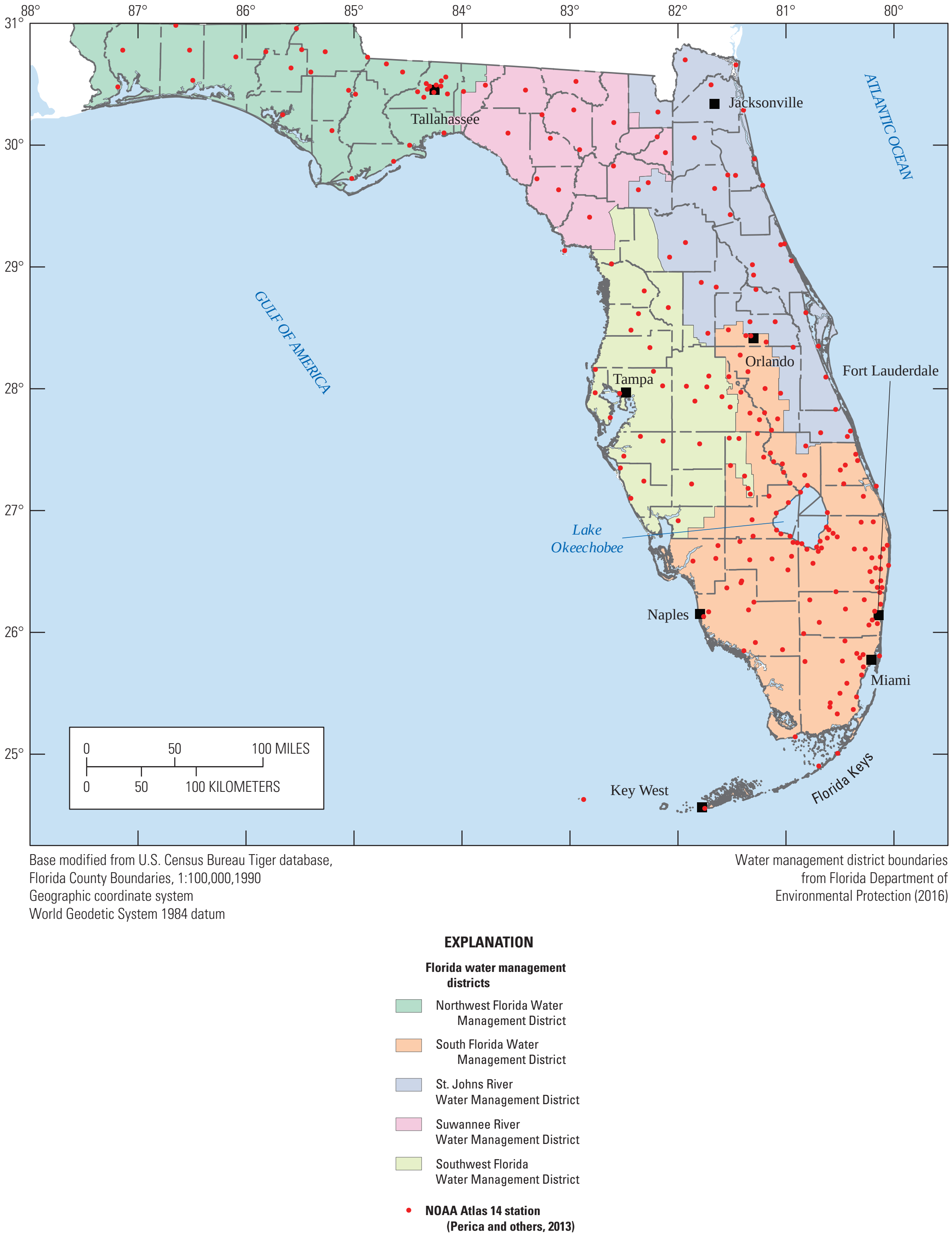

Base modified from U.S. Census Bureau Tiger database,
Florida County Boundaries, 1:100,000,1990
Geographic coordinate system
World Geodetic System 1984 datum

Water management district boundaries
from Florida Department of
Environmental Protection (2016)

**Figure 1.** Study area, National Oceanic and Atmospheric Administration (NOAA) Atlas 14 stations, and administrative and geographic features mentioned in this report.

# Datasets Used in This Study

The datasets used in this study include precipitation datasets based on observations and historical and future projected precipitation data based on statistical, dynamical, and hybrid downscaling methods applied to coarse spatial-scale output from GCMs developed as part of the World Climate Research Programme (https://www.wcrp-climate.org/) CMIP5 and CMIP6. These datasets are discussed in more detail in the following sections.

## Observational Datasets

Three observational precipitation datasets were used in this study to define a baseline for historical conditions for comparing DDF curves fitted to precipitation output from downscaled climate datasets for the historical period and for evaluating the performance of climate models in reproducing historical climate extreme indices. The observational datasets include NOAA Atlas 14 (Perica and others, 2013), which provides data at the location of weather stations, and datasets that interpolate weather-station observations to grid points: the Parameter-elevation Regressions on Independent Slopes Model (PRISM; Daly and others, 2008, 2021) and the SFWMD's Precipitation "Super-grid" (SFWMD, 2005).

### NOAA Atlas 14

The NOAA Atlas 14 dataset contains estimates of DDF and intensity-duration-frequency curves for precipitation along with associated 90-percent confidence intervals at weather stations in the United States and its territories. NOAA Atlas 14 covers the southeastern States, including Florida (volume 9 in the series of NOAA Atlas 14 reports; Perica and others, 2013). Two types of DDF curves and their confidence intervals are provided in NOAA Atlas 14. The first type is based on the annual maximum series or block-maxima approach. The second type is based on PDS and is derived by means of Langbein's formula (Langbein, 1949), which converts PDS-based average recurrence intervals to an annual exceedance probability (AEP). Selected average recurrence intervals are first converted to AEPs using Langbein's formula and then precipitation-frequency estimates are calculated for those AEPs using the same approach used in the annual maximum series analysis. Return levels (that is, the quantiles or precipitation depths associated with given return periods) derived from annual maximum series and PDS are about the same for return periods longer than 10 years.

For the southeastern United States, Perica and others (2013) found the generalized extreme value distribution to be the best among three-parameter distributions out of the five examined, to model annual maxima across the range of frequencies and durations evaluated. NOAA used the regional frequency analysis method for generalized extreme value fitting at each weather station based on the L-moments fitting method implemented one duration at a time. L-moments are a sequence of statistics that define the shape of a distribution (such as mean, skewness, and kurtosis; Hosking, 1990). The L-moments method is described in Irizarry-Ortiz and others (2022).

For this study, DDF curves based on annual maximum series and PDS along with 90-percent confidence intervals and the associated constrained annual maximum series were downloaded from NOAA's Precipitation Frequency Data Server (National Weather Service, 2020) for 242 weather stations in Florida (fig. 1). Station information is included in the data release associated with this report (Irizarry-Ortiz and Haider, 2023). Sources of weather-station data for the State of Florida used in NOAA Atlas 14 are listed in table 4.2.1 of Perica and others (2013). The period of record for these stations extends as far back as 1840 and ends in 2012 (Irizarry-Ortiz and Haider, 2023; Perica and others, 2013, appendix A.1).

Precipitation has traditionally been recorded at clock-based (constrained) intervals of 15 minutes, 1 hour, or 1 day at the 242 weather stations in Florida used in developing NOAA Atlas 14. The recording interval is also called the "base duration." Data at the base duration were accumulated over durations of interest from 5 minutes to 60 days by NOAA to develop constrained annual maximum series for each duration. Owing to the use of clock-based precipitation measurements, the constrained annual maximum series underestimates actual maxima. NOAA Atlas 14 estimated correction factors to convert the constrained annual maximum series to unconstrained annual maximum series values, which are used in DDF development. The unconstrained annual maximum series values would approximate the actual maxima for the given duration. The correction factors applied to durations of 1–4 and 7 days are shown in table 1 (Perica and others, 2013) and are similar to the theoretical correction factors determined by Weiss (1964) and to empirical values determined in other studies (Hershfield, 1961; Asquith, 1998; Overeem and others, 2008).

**Table 1.** Correction factors applied to convert constrained (clock-based) precipitation depths to unconstrained (actual maximum) precipitation depths for various durations.

| Duration (days) | Correction factor[1] |
|---|---|
| 1 | 1.12 |
| 2 | 1.04 |
| 3 | 1.03 |
| 4 | 1.02 |
| 7 | 1.01 |
| >7 | 1.00 |

[1] Perica and others (2013).

## PRISM

PRISM provides monthly and daily climate data based on interpolation of weather-station data (Daly and others, 2008, 2021). The PRISM dataset has a spatial resolution of 1/24th of a degree (approximately 4.4 kilometers [km]) and covers the conterminous United States. PRISM uses a regression model to estimate precipitation at a grid point on the basis of physiographic setting. Stations included in the regression are assigned weights based on the similarity of each station to the corresponding grid cell; similarity is defined on the basis of physiographic factors such as elevation, location, distance to the coast, and topographic facet orientation, among others (Daly and others, 2008). PRISM output of daily precipitation for Florida was downloaded for the period 1981–2019 using the prism R package (Hart and Bell, 2015). Out of the seven gridded datasets evaluated by Behnke and others (2016) (including Daymet and Livneh), PRISM best captured daily precipitation statistics and climate extremes indices at a set of independent meteorological stations from the Florida Automated Weather Network (Lusher and others, 2008).

As part of this study, PRISM daily-precipitation data were used to develop areal reduction factors (ARFs), which convert point precipitation extremes to areal precipitation extremes. PRISM was also used in this study to evaluate models for culling, which is the process by which the most reliable climate models are selected to compute change factors. The PRISM grid is shown in figure 2*A*.

## SFWMD’s Precipitation “Super-Grid”

The SFWMD’s precipitation “Super-grid” is a gridded dataset of daily precipitation, with a spatial resolution of 3.2 km, that covers most of the SFWMD, except the Florida Keys (fig. 2*B*). The SFWMD “Super-grid” dataset was developed using the TIN–10 method (SFWMD, 2005) to interpolate gage precipitation data from 1914 to 2002. Gage-corrected Next Generation Weather Radar precipitation data are used in this dataset from 2002 to 2016 (SFWMD, 2020). This dataset was developed by the SFWMD to provide complete spatial coverage and sufficient length of record for regional hydrologic modeling and trend analysis (SFWMD, 2005). In this study, the SFWMD “Super-grid” precipitation dataset was used for model culling in addition to PRISM.

# Downscaled Climate Datasets

Various efforts to downscale global climate predictions to local and regional scales have been initiated by climate research groups in the United States and abroad. In this study, historical and future projections of precipitation based on statistical, dynamical, and hybrid downscaling of GCMs were used to develop future DDF curves for Florida. The GCMs were developed as part of the World Climate Research Programme’s CMIP5 and CMIP6. The CMIP5 model data are a concatenation of historical (retrospective) GCM simulations covering the period 1850–2005 and future projections for the period 2006–2100 (Lawrence Livermore National Laboratory, 2022a). The CMIP6 historical simulation period is 1950–2014, and future projections encompass the period 2015–2100 (Lawrence Livermore National Laboratory, 2022b). Taylor and others (2012) provide an overview of the CMIP5 experimental design and Eyring and others (2016) for CMIP6. Notably, the historical CMIP5 and CMIP6 model simulations are not intended to reproduce the precise sequence of historical climate variability. GCMs are often run starting with different initial conditions to create an ensemble of possible trajectories for the historical and future climates that may result because of changes in natural variability (unforced or internal variability, also called climate noise in Taylor and others, 2012). The use of ensembles helps separate the climate change “signal” from the climate noise. Often, only one ensemble member is used for downscaling, which limits the range of events that are downscaled. Table 2 lists the number of ensemble members downscaled by each downscaled climate dataset by emission scenario. The particular ensemble members downscaled for each GCM by each of the downscaled climate datasets used in this study are listed in the data release associated with this report (Irizarry-Ortiz and Haider, 2023).

The CMIP5 future projections are based on four different representative concentration pathways (RCPs) corresponding to low (RCP2.6), medium-low (RCP4.5), medium-high (RCP6.0), and high (RCP8.5) year 2100 total radiative forcing values with respect to the preindustrial period (circa 1750; Intergovernmental Panel on Climate Change [IPCC], 2013; van Vuuren and others, 2011). The number next to the RCP label indicates the approximate increase in total radiative forcing at the end of the century (2100), in watts per meter squared, caused by GHG emissions. RCP2.6 represents a scenario of stringent climate policies to reduce GHG emissions, and the radiative forcing increase at 2100 from GHG emissions is 2.6 watts per meter squared. RCPs with higher numbers are the result of higher emissions and result in larger changes in global temperatures. RCP8.5 represents future conditions that could result from limited or no climate change mitigation, is a worst-case scenario (Hausfather and Peters, 2020), and is considered low likelihood by the IPCC (2021a); the two middle scenarios are roughly equally spaced between the low and high scenarios (Terando and others, 2020). Similar to the historical simulations, the CMIP5 future projections are also not intended to simulate the precise sequence of actual future variations in climate and may not capture the exact timing of future shifts in natural cycles. Terando and others (2020) recommend that, whenever feasible, the entire range of RCP-based scenarios be considered when assessing potential future effects; however, the choice of scenarios is limited by their availability in downscaled climate datasets. For CMIP5, only RCP4.5 and RCP8.5 are available in most downscaled climate datasets.

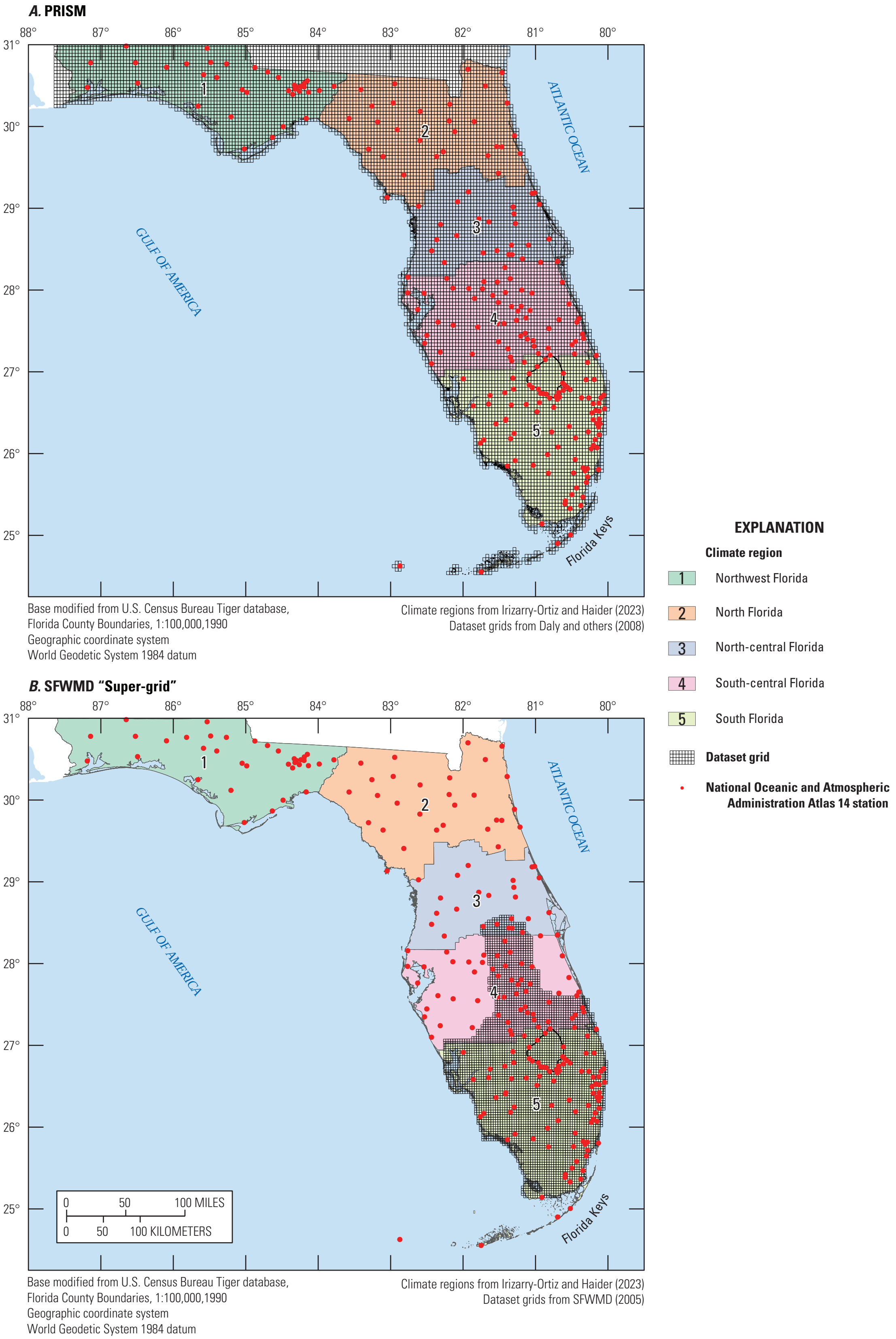

Base modified from U.S. Census Bureau Tiger database,
Florida County Boundaries, 1:100,000,1990
Geographic coordinate system
World Geodetic System 1984 datum

Climate regions from Irizarry-Ortiz and Haider (2023)
Dataset grids from Daly and others (2008)

Base modified from U.S. Census Bureau Tiger database,
Florida County Boundaries, 1:100,000,1990
Geographic coordinate system
World Geodetic System 1984 datum

Climate regions from Irizarry-Ortiz and Haider (2023)
Dataset grids from SFWMD (2005)

**Figure 2.** Climate regions and model grids for the *A*, Parameter-elevation Regressions on Independent Slopes Model (PRISM; about 4-kilometer grid spacing); and *B*, South Florida Water Management District (SFWMD) “Super-grid” datasets (about 3.2-kilometer grid spacing).

**Table 2.** Number of ensemble members downscaled by each downscaled climate dataset by emission scenario.

[SSP, shared socioeconomic pathway; RCP, representative concentration pathway; CORDEX, Coordinated Regional Downscaling Experiment; JupiterWRF, Jupiter Intelligence Weather Research and Forecasting model; LOCA, Localized Constructed Analogs; LOCA2, Localized Constructed Analogs version 2; MACA, Multivariate Adaptive Constructed Analogs; NEX-GDDP, National Aeronautics and Space Administration Earth Exchange Global Daily Downscaled Projections]

| Dataset | Emission scenario | | | | |
|---|---|---|---|---|---|
| | SSP1-2.6 | RCP4.5/SSP2-4.5 | SSP3-7.0 | RCP8.5/SSP5-8.5 | Total |
| CORDEX | 0 | 14 | 0 | 54 | 68 |
| JupiterWRF | 0 | 3 | 0 | 4 | 7 |
| LOCA | 0 | 30 | 0 | 30 | 60 |
| LOCA2 | 0 | 64 | 92 | 65 | 221 |
| MACA | 0 | 40 | 0 | 40 | 80 |
| NEX-GDDP | 32 | 34 | 28 | 35 | 129 |
| **Total** | **32** | **185** | **120** | **228** | **565** |

The CMIP6 projection scenarios are described by Eyring and others (2016) and Riahi and others (2017) and are based on the concept of shared socioeconomic pathways (SSPs), which have been developed by the energy modeling community. Updated versions of the four CMIP5 RCP scenarios are available in CMIP6 and are called SSP1-2.6, SSP2-4.5, SSP4-6.0, and SSP5-8.5, with each of these having a similar change in 2100 radiative forcing levels as their CMIP5 RCP counterparts and representing low, medium-low, medium, and high emissions scenarios, respectively. The first number next to the SSP label indicates different levels of challenges to mitigation and adaptation resulting from different potential future socioeconomic trends, as described by Riahi and others (2017), and the number after the dash indicates the approximate increase in total radiative forcing at the end of the century (2100), in watts per meter squared, caused by GHG emissions. Despite the 2100 radiative forcing being similar between a CMIP6 SSP scenario and its CMIP5 RCP counterpart, the pathways of emissions, GHG mix, and land uses vary over time between the RCP and corresponding SSP scenario. Figure 1.28 of the IPCC’s sixth assessment report (IPCC, 2021a) shows a comparison of the range of fossil fuel and industrial carbon dioxide ($CO_2$) emissions across IPCC assessments that include the RCP and SSP scenarios.

Effective radiative forcing at the end of the 21st century is slightly higher in the CMIP6 SSP than in the equivalently named CMIP5 RCP scenario (fig. 3 of Fredriksen and others, 2023). The IPCC (2023, p. 9) states with medium confidence that “the overall radiative forcing tends to be higher for the SSPs compared to the RCPs with the same level.” For this reason, results from CMIP5 and CMIP6 may not be directly comparable. The use of different GCMs or different versions of GCM models in the two CMIPs also precludes a direct comparison. CMIP6 also includes four additional SSPs representing intermediate levels of forcing between the four original scenarios such as the medium-to-high scenario SSP3-7.0. The CMIP6 model data are a concatenation of historical (retrospective) GCM simulations covering the period 1850–2014 and future projections for the period from 2015 to at least 2100. A description of the GCMs downscaled by the different downscaled climate datasets evaluated in this study can be found in the data release associated with this report (Irizarry-Ortiz and Haider, 2023).

Many GCMs are unable to simulate extremes well because of their coarse spatial resolution and their inability to capture subgrid-scale physics (Misra and others, 2011). Statistical and dynamical downscaling are two methods used to generate high-resolution (about 50-km grid spacing or less) climate projections based on coarse-resolution fields simulated by GCMs. In statistical downscaling, coarse-resolution fields (typically about 100-km grid spacing or greater) simulated by GCMs are used as predictors of high-resolution meteorological variables (Wilby and Wigley, 1997; Wilby and others, 1998). Historical observations are used to train and bias-correct the statistical-downscaling methods. Such methods are largely empirical and are based on the inherent assumption that the methods will perform equally well in the future as in the historical training period (Nover and others, 2016). In dynamical downscaling, a regional climate model (RCM) is forced by coarse-resolution boundary and initial conditions from a coarse-resolution GCM. Like a GCM, an RCM solves the physical equations, but over a limited area and discretized at finer temporal and spatial resolutions than the source GCM output. This method results in more physically based downscaling than that of statistical methods. Dynamical downscaling is more time and computer-resource-intensive than statistical downscaling, however, so RCM resolutions on the order of tens of kilometers are typically used to downscale long-term simulations. Because of modeling limitations, output from RCMs is also often bias-corrected to observations. Lastly, hybrid approaches that combine features of statistical and dynamical downscaling have been developed. These approaches combine the ability of dynamical techniques to capture the physics of the precipitation process with a reduction in computational requirements for downscaling a single or multiple GCMs (see, for example, Walton and others, 2015; Madaus and others, 2020). Irizarry-Ortiz and others (2022) discuss downscaling methods in more detail.

## LOCA

The University of California at San Diego has developed the LOCA statistical-downscaling technique (Pierce and others, 2014; Pierce, 2025) to downscale 32 GCMs from the CMIP5 archive at 1/16th arc-degree (approximately 6.6 km) spatial resolution (fig. 3*A*), covering North America from central Mexico through southern Canada. The historical period for this dataset is 1950–2005, and two future projected scenarios are available: RCP4.5 and RCP8.5 over the period 2006–2100, although data are only available through 2099 for some models. Only one ensemble member from each CMIP5 GCM is downscaled by the LOCA method. The Fourth National Climate Assessment (Avery and others, 2018) relied on the LOCA dataset as a source of downscaled climate information. For this study, daily precipitation data for the State of Florida were originally downloaded from the USGS Center for Integrated Data Analytics (CIDA) THREDDS data server, which has since been retired as a server (USGS CIDA, 2024). Pierce (2025) provides links to websites from which LOCA datasets can be downloaded. The CMIP5 models downscaled by using the LOCA method and used in this study are listed in Irizarry-Ortiz and others (2022) and the data release associated with this report (Irizarry-Ortiz and Haider, 2023).

The LOCA method is a statistical-downscaling technique that uses historical observations to add improved fine-scale detail to global climate models (Pierce and others, 2014). The statistical-downscaling methodology used for LOCA is described in detail in Pierce and others (2014, 2015), Lopez-Cantu and others (2020), and Irizarry-Ortiz and others (2022). The historical observational gridded precipitation dataset used for LOCA is the Livneh and others (2015; 6.6-km native resolution) dataset over the period 1950–2005. Pierce and others (2021) and Wootten and others (2021) found that daily precipitation extremes are muted by about 30 percent in the Livneh and others (2015) dataset over most areas of the continental United States, including Florida, and attribute this to the way Livneh and others (2015) split daily precipitation measurements across 2 days, depending on time of observation. This affects single-day events more than multiday events in both Livneh (Wootten and others, 2021) and the derived LOCA dataset. For Florida in particular, Behnke and others (2016) found that out of the seven gridded datasets evaluated, Livneh performed the worst in capturing extreme precipitation climate indices at meteorological stations that are part of the Florida Automated Weather Network (Lusher and others, 2008; University of Florida IFAS Extension, 2026).

## MACA

The University of California Merced has developed the MACA statistical-downscaling technique (Abatzoglou and Brown, 2012; University of California Merced, 2026) to downscale 20 GCMs from the CMIP5 archive to spatial resolutions of 1/24th degree (approximately 4.4 km) to 1/16th degree (approximately 6.6 km) for the continental United States. Figure 3*B*–*C* shows grid resolutions of two MACA datasets for Florida. The historical period for the MACA datasets is 1950–2005, and two future projected scenarios are available over the period 2006–99: RCP4.5 and RCP8.5. The MACA dataset is described in more detail by Abatzoglou and Brown (2012).

MACA version 2 utilizes two observational gridded “training” datasets for bias correction and analog construction: Livneh 2013 (1950–2011; 6.6-km native resolution; Livneh and others, 2013) and gridMET (1979–2012; 4.4-km native resolution; Abatzoglou, 2013). GridMET is also known as Metdata. Hereafter, the MACA data based on these two training datasets will be called MACA-Livneh and MACA-gridMET. Deficiencies in the Livneh and others (2015) observational dataset related to how observations of daily precipitation are split across consecutive days previously described for LOCA also apply to the Livneh and others (2013) dataset used in MACA (see the “Localized Constructed Analogs (LOCA)” section herein). For this study, daily precipitation data for the State of Florida for MACA-gridMET were downloaded from the USGS CIDA THREDDS data server, which has since been retired as a server (USGS CIDA, 2024). MACA-gridMET data are available at Abatzoglou and Hegewisch (2016). Daily precipitation data for the State of Florida for MACA-Livneh were downloaded from the Northwest Knowledge Network (NKN) THREDDS data server (NKN, 2021). The CMIP5 models downscaled by MACA and used in this study are listed in Irizarry-Ortiz and others (2022) and in the data release associated with this report (Irizarry-Ortiz and Haider, 2023).

The MACA technique is a statistical-downscaling method that directly incorporates synoptic daily weather fields from GCMs using a “weather-typing” approach to resolve subsynoptic or mesoscale features. The overall procedure for downscaling precipitation is detailed in Lopez-Cantu and others (2020) and Irizarry-Ortiz and others (2022). The MACA method was validated across the western United States by Abatzoglou and Brown (2012) using daily data from the European Centre for Medium-Range Weather Forecasts ERA-Interim reanalysis (Simmons and others, 2007) dataset in place of a GCM for the period 1989–2008.

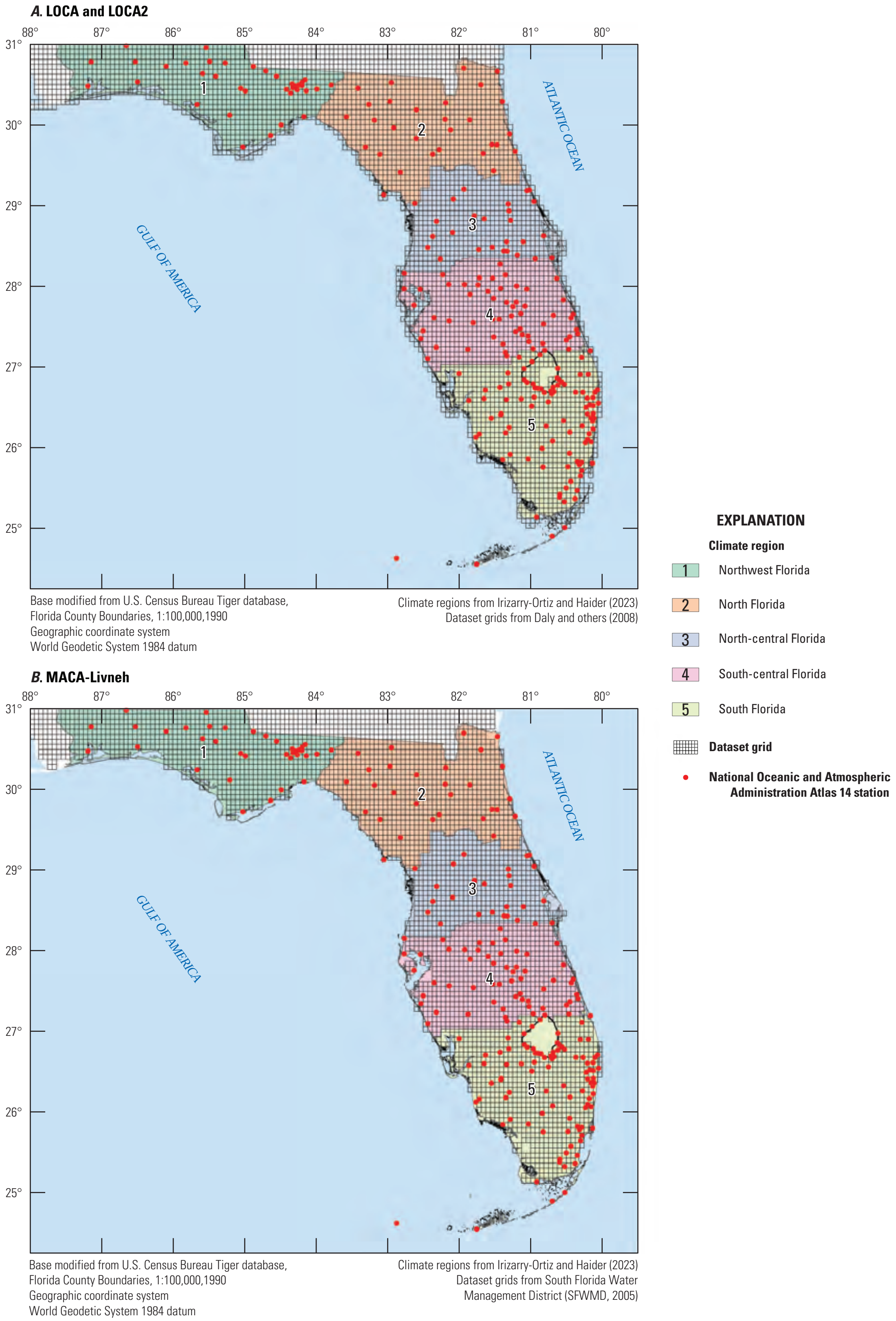

Base modified from U.S. Census Bureau Tiger database,
Florida County Boundaries, 1:100,000,1990
Geographic coordinate system
World Geodetic System 1984 datum

Climate regions from Irizarry-Ortiz and Haider (2023)
Dataset grids from Daly and others (2008)

Base modified from U.S. Census Bureau Tiger database,
Florida County Boundaries, 1:100,000,1990
Geographic coordinate system
World Geodetic System 1984 datum

Climate regions from Irizarry-Ortiz and Haider (2023)
Dataset grids from South Florida Water
Management District (SFWMD, 2005)

**Figure 3.** Grids for the, *A*, Localized Constructed Analogs (LOCA) and LOCA version 2 (LOCA2); *B*, Multivariate Adaptive Constructed Analogs (MACA) Livneh; *C*, MACA-gridMET; *D*, Coordinated Regional Downscaling Experiment (CORDEX) NAM-22i; *E*, CORDEX NAM-44i; *F*, National Aeronautics and Space Administration (NASA) Earth Exchange Global Daily Downscaled Projections (NEX-GDDP); *G*, Jupiter Intelligence Weather Research and Forecasting (JupiterWRF) model; and *H*, North America Weather Research and Forecasting (WRF) model datasets.

***C.* MACA-gridMET**

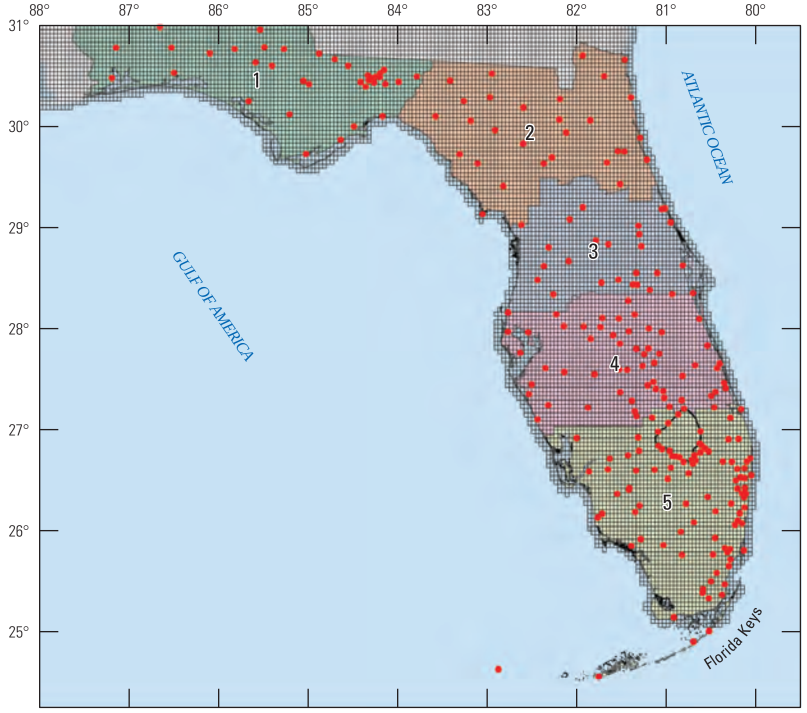

Base modified from U.S. Census Bureau Tiger database, Florida County Boundaries, 1:100,000,1990
Geographic coordinate system
World Geodetic System 1984 datum

Climate regions from Irizarry-Ortiz and Haider (2023)
Dataset grids from U.S. Geological Survey (USGS, 2021a, b)

***D.* CORDEX NAM-22i**

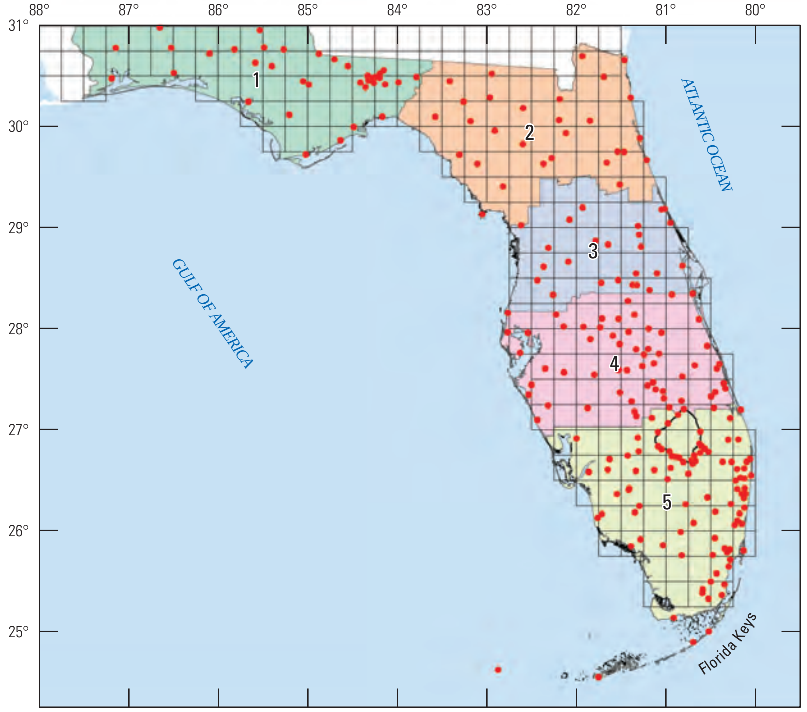

Base modified from U.S. Census Bureau Tiger database, Florida County Boundaries, 1:100,000,1990
Geographic coordinate system
World Geodetic System 1984 datum

Climate regions from Irizarry-Ortiz and Haider (2023)
Dataset grids from Mearns and others (2017)

**EXPLANATION**

**Climate region**

| | |
|---|---|
| 1 | Northwest Florida |
| 2 | North Florida |
| 3 | North-central Florida |
| 4 | South-central Florida |
| 5 | South Florida |
| ▦ | **Dataset grid** |
| ● | **National Oceanic and Atmospheric Administration Atlas 14 station** |

**Figure 3.**—Continued

***E.* CORDEX NAM-44i**

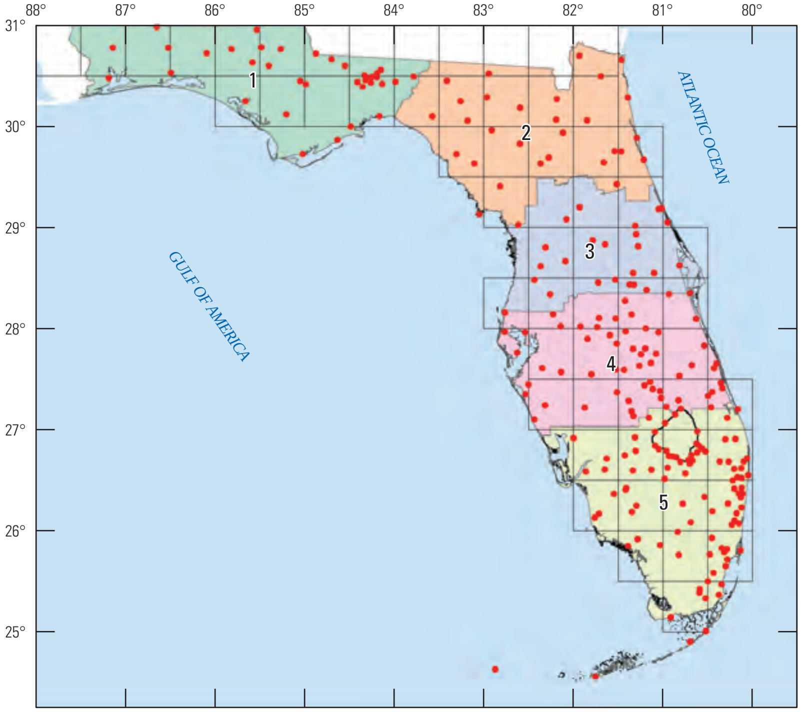

Base modified from U.S. Census Bureau Tiger database,
Florida County Boundaries, 1:100,000,1990
Geographic coordinate system
World Geodetic System 1984 datum

Climate regions from Irizarry-Ortiz and Haider (2023)
Dataset grids from Mearns and others (2017)

***F.* NEX-GDDP**

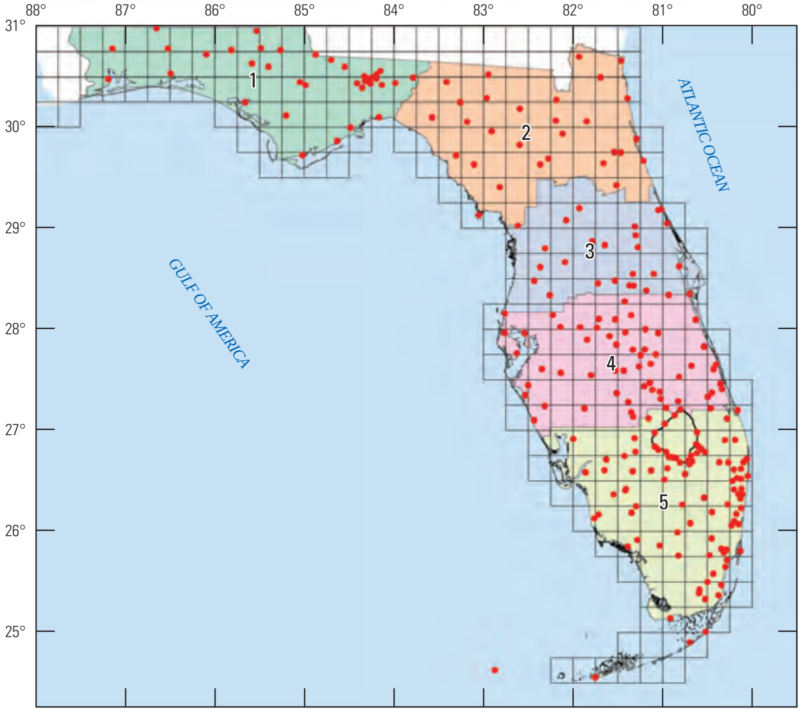

Base modified from U.S. Census Bureau Tiger database,
Florida County Boundaries, 1:100,000,1990
Geographic coordinate system
World Geodetic System 1984 datum

Climate regions from Irizarry-Ortiz and Haider (2023)
Dataset grids from Thrasher and others (2021)

**EXPLANATION**

**Climate region**

1 Northwest Florida
2 North Florida
3 North-central Florida
4 South-central Florida
5 South Florida

▦ **Dataset grid**

● **National Oceanic and Atmospheric Administration Atlas 14 station**

**Figure 3.**—Continued

**G.** Jupiter WRF

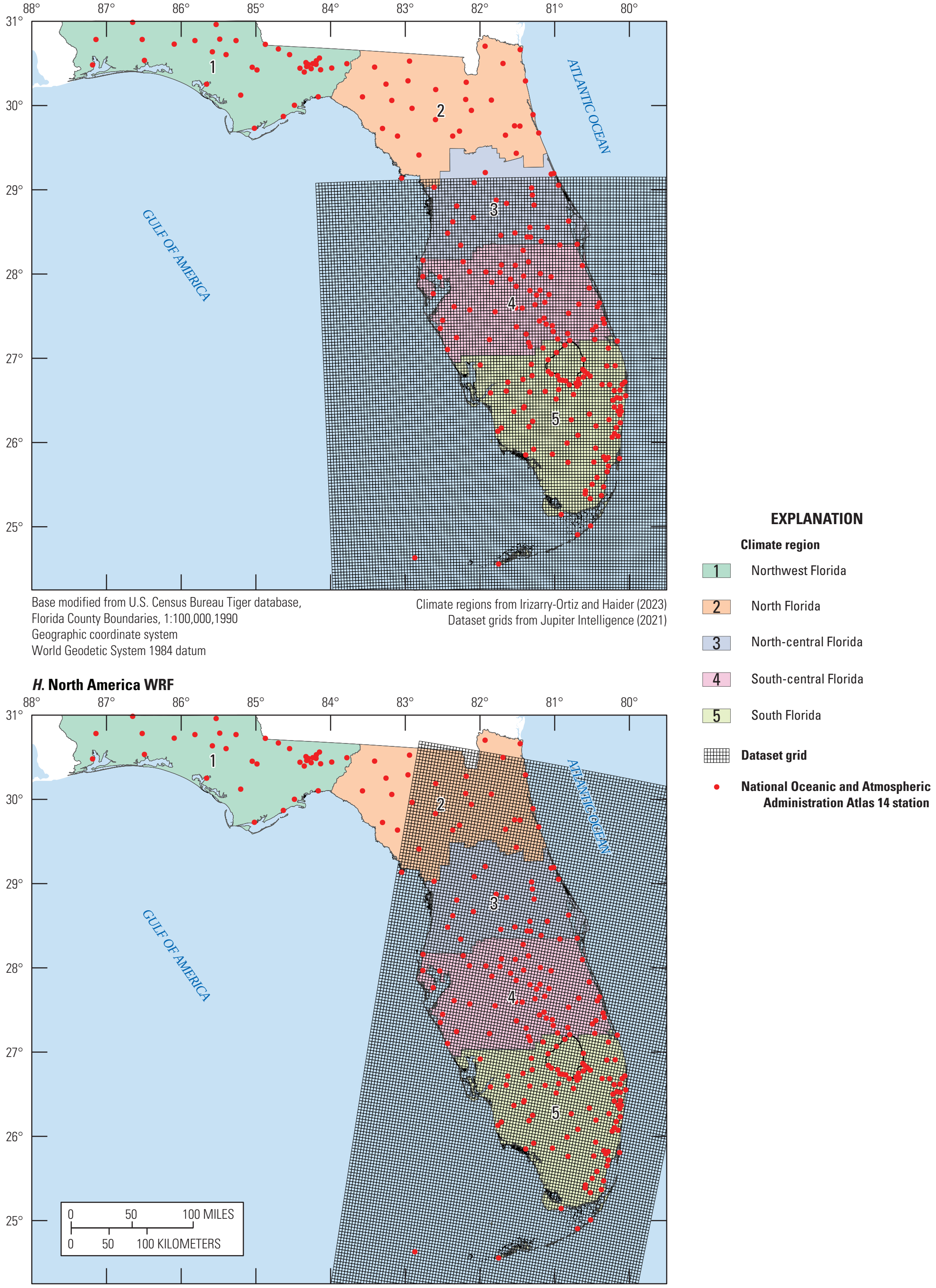

Base modified from U.S. Census Bureau Tiger database, Florida County Boundaries, 1:100,000,1990
Geographic coordinate system
World Geodetic System 1984 datum

Climate regions from Irizarry-Ortiz and Haider (2023)
Dataset grids from Jupiter Intelligence (2021)

**H.** North America WRF

Base modified from U.S. Census Bureau Tiger database, Florida County Boundaries, 1:100,000,1990
Geographic coordinate system
World Geodetic System 1984 datum

Climate regions from Irizarry-Ortiz and Haider (2023)
Dataset grids from Liu and others (2017)

**Figure 3.**—Continued

## CORDEX

The North American Coordinated Regional Downscaling Experiment (NA-CORDEX) is part of the global CORDEX program sponsored by the World Climate Research Program to provide global coordination of regional climate downscaling (Giorgi and others, 2009; Mearns and others, 2017). NA-CORDEX consists of output from RCMs over a domain covering the majority of North America and using boundary conditions from CMIP5 GCMs (tables 6 and 7 of Irizarry-Ortiz and others, 2022). According to Bukovsky and others (2021), the existing NA-CORDEX simulations for both the historical and future climates keep the land surface conditions constant at present-day conditions. The historical period for most models is 1950–2005, whereas the future projection period is from 2006 to 2100. Future projections are available for RCP4.5 and RCP8.5 scenarios. The RCMs have a spatial resolution of 0.22° (approximately 25 km) or 0.44° (approximately 50 km) and produce data for critical climate variables, including daily precipitation. Because the grids from the various RCMs are not all coincident, the data are also made available on two common grids of 0.25° or 0.50° resolution (called NAM-22i and NAM-44i, respectively) based on interpolation of the native RCM grid (fig. 3*D*–*E*). Bias-corrected, simulated meteorological data are also provided by NA-CORDEX. The bias correction of the RCM output is performed using the multivariate quantile-mapping method MBCn (Cannon, 2018) using the gridMET (1979–2016; 4.4-km native resolution; Abatzoglou, 2013) or Daymet (1980–2017; 1-km native resolution; Thornton and others, 2016) gridded observational datasets. Bias correction is done for the central calendar month of a 3-month sliding window at each grid point (Cannon, 2018).

The NA-CORDEX experiment downscaled GCMs have a wide range of equilibrium climate sensitivity from 2.4 to 4.6 °C (Irizarry-Ortiz and others, 2022) to encompass a large range of possible changes in climate. For this study, bias-corrected daily precipitation data on the common NAM-22i and NAM-44i grids were obtained from the National Center for Atmospheric Research (NCAR, 2021, 2022) for the State of Florida. For a list of GCMs and RCMs used in NA-CORDEX and downloaded for Florida, see Irizarry-Ortiz and others (2022) and the data release associated with this report (Irizarry-Ortiz and Haider, 2023). An error was previously found in the bias-corrected CORDEX data downloaded before November 19, 2021, as described by Mearns and others (2017); however, the NA-CORDEX bias-corrected data were corrected and republished by the NCAR as of November 19, 2021, and this updated dataset was used for this study (NCAR, 2021, 2022). It is evident, especially for the CORDEX NAM-44i grid, that many NOAA Atlas 14 stations are located within a single grid cell (fig. 3*D*–*E*). This clustering is most pronounced in areas of high station density such as the southeast coast of Florida (fig. 3*D*–*E*).

## JupiterWRF

Jupiter Intelligence (https://www.jupiterintel.com) has developed a Weather Research and Forecasting (WRF; Skamarock and others, 2019) model for central and south Florida at 4-km resolution that can be used to downscale historical observations of extreme precipitation events in the region (fig. 3*G*). They provided the USGS with simulated precipitation fields at 15-minute temporal resolution and 4-km spatial resolution for 1,044 historical precipitation events between 1979 and 2017 (Jupiter Intelligence, 2021). The output from this model is used by Jupiter Intelligence, together with an analog resampling and statistical scaling method they developed, to produce downscaled future climate projections of extreme precipitation events. Because this method uses high-resolution output from climate models as well as statistical techniques, it is considered a hybrid downscaling approach.

An analog resampling technique is used by Jupiter Intelligence to project future changes in event frequency caused by changes in large-scale meteorological fields that are conducive to extreme precipitation over central and south Florida. For analog resampling, Jupiter Intelligence uses future projections from various CMIP5 and CMIP6 GCMs, which are listed in Irizarry-Ortiz and others (2022) and in the data release associated with this report (Irizarry-Ortiz and Haider, 2023). To provide a wider range of potential future extreme events, many ensemble members are used for each GCM when available. The GCMs and projections used for analog resampling were chosen by Jupiter Intelligence primarily on the basis of a subjective evaluation of their relative quality compared to other GCMs and on the availability of the daily meteorological data needed to define analogs. To project future changes in event magnitude, Jupiter Intelligence uses a statistical scaling technique that intends to capture increases in extreme precipitation resulting from increases in the atmosphere’s water holding capacity under global warming. The statistical scaling technique uses output from a WRF model of North America by Liu and others (2017), which is also described by Rasmussen and others (2020). The portion of the North America WRF model grid in central and south Florida is shown in figure 3*H*. The statistical scaling data were provided to the USGS by Jupiter Intelligence. Data are not currently available from Jupiter Intelligence. Contact Jupiter Intelligence for further information.

Additional details about how to implement this method are included in appendix 2 of Irizarry-Ortiz and others (2022) and were provided by Jupiter Intelligence. The method was programmed as an R script (R Core Team, 2020) to provide estimates of future DDF curves for daily duration only.

## LOCA2

The University of California at San Diego has recently developed a second version of the LOCA dataset (LOCA2; Pierce and others, 2023) using the LOCA statistical-downscaling technique to downscale as many as 10 ensemble members from 27 GCMs from the CMIP6 archive on the same grid as the original LOCA dataset (fig. 3*A*). The training dataset used by LOCA2 is the “Livneh unsplit” daily gridded precipitation dataset over the period 1950–2014 (6.6-km native resolution; Pierce and others, 2021), which better preserves daily precipitation extremes than the Livneh and others (2015) dataset used in the original LOCA.

The historical period for LOCA2 matches that of the CMIP6 GCMs (1950–2014), and three future projected scenarios are available: SSP2-4.5, SSP3-7.0, SSP5-8.5 over the period 2015–2100. Multiple ensemble members are downscaled, which allows for potential alternative trajectories for the historical and future climates that may result from changes in natural variability to be considered. The Fifth National Climate Assessment (Basile and others, 2023; Marvel and others, 2023) relied on the LOCA2 dataset as a source of downscaled climate information. For this study, daily precipitation data were downloaded via the Globus command line interface connected to the LOCA2 collection at Lawrence Berkeley Lab (2023). Data were clipped to the State of Florida using Climate Data Operators (CDO) utilities (Max Planck Institute for Meteorology, 2022a). The CMIP6 models downscaled in LOCA2 and used in this study are listed in the data release associated with this report (Irizarry-Ortiz and Haider, 2023).

Most of the methods used in the first version of LOCA are used in LOCA2; however, a multi-ensemble member bias-correction scheme described in Pierce and others (2023) was used for models with multiple ensemble members. This approach allows for each ensemble member to have a different maximum daily extreme at each grid cell from the one present in the training dataset. This method performs better at preserving rare extreme precipitation events than if each ensemble member were bias-corrected independently.

## NEX-GDDP

The NEX-GDDP CMIP6 dataset (Thrasher and others, 2021, 2022) provides global daily downscaled precipitation data at 0.25° (approximately 25 km) resolution for 35 CMIP6 GCMs for as many as four future SSP scenarios: SSP1-2.6, SSP2-4.5, SSP3-7.0, SSP5-8.5; the NEX-GDDP grid in Florida is shown in figure 3*F*. The historical period for this dataset is 1950–2014, and the future projection period is 2015–2100. The CMIP6 models downscaled in this dataset and used in this study are listed in the data release associated with this report (Irizarry-Ortiz and Haider, 2023). The dataset was developed using the Bias-Correction Spatial Disaggregation (BCSD) statistical-downscaling method (Wood and others, 2002, 2004; Maurer and Hidalgo, 2008; Thrasher and others, 2012) and uses the 0.25°-resolution (~26.2-km) Global Meteorological Forcing Dataset (GMFD) for Land Surface Modeling from the Terrestrial Hydrology Research Group at Princeton University (Sheffield and others, 2006) over the period 1960–2014. GMFD combines National Centers for Environmental Prediction NCAR reanalysis precipitation with global observational data, which are then disaggregated to 0.25°-resolution by statistical downscaling. Daily precipitation data for the State of Florida were downloaded from the NASA Center for Climate Simulation THREDDS data server (NASA, 2022).

Prior to the BCSD procedure, the monthly large-scale climate trends are extracted from the GCM precipitation data as a 9-year running average for each individual month of the year. For bias correction, the BCSD technique uses quantile mapping (Panofsky and Brier, 1968) of GCM precipitation onto gridded precipitation observations that have been spatially aggregated to the scale of the GCM. For a given day, the algorithm generates cumulative distribution functions (CDFs) for the GMFD data and for the historical GCM simulations by pooling data for the day of the year ±15 days over the reference period 1960–2014. The same mapping is applied to future GCM projections. The result is that the mean and the variability of the downscaled precipitation evolves according to the GCM simulation, whereas all of the statistical moments between the GCM and observations are matched in the reference period. After the bias-correction step, the climate trends are added back onto the adjusted GCM climate fields.

The spatial-disaggregation step spatially interpolates the adjusted GCM precipitation fields to the finer resolution grid of GMFD. This process is done in several steps: (1) a smoothed daily climatology is calculated from the gridded GMFD observations over the reference period using a Fast Fourier Transform that retains three harmonics at both the native and GCM-scale resolutions; (2) in each timestep, the bias-corrected GCM precipitation is compared to the corresponding GMFD climatology to calculate quotient “scaling factors”; (3) the coarse-resolution scaling factors are bilinearly interpolated to the GMFD grid; and (4) the interpolated scaling factors are multiplied by the fine-resolution GMFD climatologies to obtain the final downscaled climate fields.

The algorithm essentially merges the observed historical spatial climatology with the relative changes or scaling factors at each timestep as simulated by the GCMs and assumes that the relative spatial patterns in the 1960–2014 observations will remain constant under future climate change. The algorithm does not add information beyond that contained in the original CMIP6 simulations, other than by increasing spatial resolution and by bias correction. Therefore, it preserves the frequency of periods of anomalously high and low values contained within each individual simulation. The method does not affect the slope of the trends in the GCM projections, but if the model is biased in the historical period, it affects the offset of the climate trends by shifting the retrospective period to match the GMFD data. Although this dataset extends to the Florida Keys, the technical note associated with the dataset (Thrasher and others, 2021) warns that because of lack of validation of GMFD over oceans, downscaled values over small island areas might not be realistic. The technical note (Thrasher and others, 2021, p. 7) also states that “This dataset is intended for use in scientific research only, and the use of this dataset for other purposes, such as commercial applications, and engineering or design studies is not recommended without consultation with a qualified expert.”

# Methods

The methodology used to derive change factors based on CORDEX, LOCA, MACA, LOCA2, and NEX-GDDP downscaled climate datasets is the same used by Irizarry-Ortiz and others (2022) and is illustrated in the flow chart on figure 4. Change factors were computed for these five downscaled climate datasets for durations of 1, 3, and 7 days, and return periods of 5, 10, 25, 50, 100, 200, and 500 years. The historical period was chosen as the 40-year period 1966–2005, which is centered around 1985. The beginning of this period matches the approximate beginning of the global warming trend from the 1970s onward (Rahmstorf and others, 2017), and the end was selected to match the end of the CMIP5 historical simulations (2005). Two 40-year future (projected) periods of interest include a period centered around 2040 that spans 2020–59, and a period centered around 2070 that spans 2050–89. These two 40-year periods were used to develop change factors for application of the Multiplicative Quantile Delta Mapping (MQDM) bias-correction method described in the “Multiplicative Quantile Delta Mapping” section herein.

Stationarity was assumed within the 40-year historical and future projection periods of interest, which means that a quasi-stationary approach was used. The assumption of quasi-stationarity implies that stationarity can be assumed under defined conditions, such as over a given period of time. Other studies, such as those by Ren and others (2019) and NOAA (2022a), have used the quasi-stationary approach for DDF fitting during specific time windows identified using trend tests. A quasi-stationary approach was used in this study because of the high degree of subjectivity in defining how the parameters of the extreme value distribution may vary in time, which increases uncertainty in return levels. First-order stationarity was tested using the Mann-Kendall nonparametric trend test (Mann, 1945; Kendall, 1970). For an in-depth discussion of these and other issues related to the assumption of nonstationarity in extreme value analysis, see Coles (2001) and Serinaldi and Kilsby (2015).

Most of the analysis done as part of this study was performed using R programming software (R Core Team, 2020) and various common statistical and extreme value analyses packages on USGS desktop/laptop computers and the USGS Denali supercomputer (Falgout and others, 2023). The next sections describe the theory behind the methods used to compute change factors based on the CORDEX, LOCA, MACA, LOCA2, and NEX-GDDP datasets, followed by details on the implementation of the methodology. The methods used for deriving change factors from JupiterWRF output for daily duration are described in appendix 2 of Irizarry-Ortiz and others (2022).

## Extreme Value Theory

Extreme value theory (EVT) is a branch of statistics that deals with the stochastic behavior of extreme and rare events found in the tails of probability distributions and includes events that are unusually large or small. The extreme events modeled in EVT are beyond the central tendency and most frequent range of variation of the variable at hand and include the estimation of events that are more extreme than any that have already been observed (Coles, 2001). The probability of occurrence of a climate or weather variable can be described by a probability distribution function. The upper tail of the probability distribution, representing the larger values of extreme precipitation, might change under future conditions. EVT provides a class of models that make it possible to extrapolate from observed or modeled extremes to unobserved or unmodeled extremes (Coles, 2001).

EVT has developed under two main approaches. In the classical block maxima (or minima) approach (Fisher and Tippett, 1928; Jenkinson, 1955; Coles, 2001), the probability distribution of maxima (minima) over a given block of time, typically a year, is modeled. This is herein referred to as the “annual maxima approach.” The second approach, called peaks-over-threshold (POT), consists of extracting from a continuous record the peak values that exceed (or fall below) a particular threshold and modeling their distribution (Davison and Smith, 1990; Irizarry-Ortiz and others, 2022). The timeseries of threshold exceedances derived from the POT approach is a PDS. Both extreme value approaches can be implemented under stationary and nonstationary frameworks. Stationarity implies that, given any subset of variables, their joint distribution stays the same through time, which is the approach taken here. In this study, first-order stationarity was validated using the Mann-Kendall nonparametric trend test with a significance level (alpha) of 0.05. In contrast, nonstationary processes have characteristics that change systematically through time, for example, as seasonal effects or in the form of trends (Coles, 2001). These changes are reflected as changes in their probability distribution through time. Irizarry-Ortiz and others (2022) provide a detailed discussion of the annual maxima and POT approaches. The POT approach was used in this study and will be discussed hereafter in the context of the stationary framework.

## ARFs

ARFs are used in stormwater infrastructure design to convert point precipitation for a given duration and return period into areal precipitation over a given area for the same duration and return period (Pavlovic and others, 2016). Typically, the area of interest is a watershed. ARFs are also

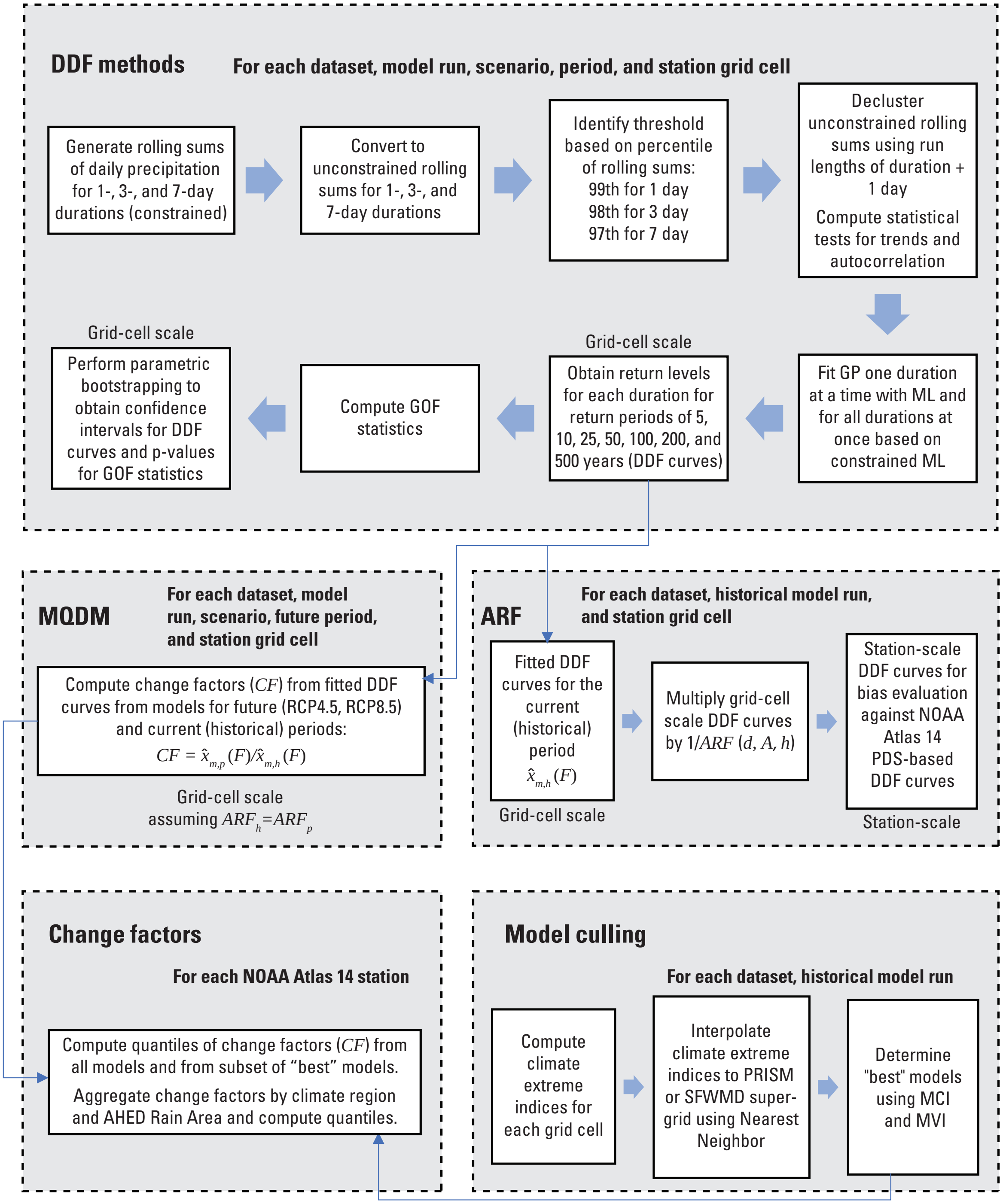

EXPLANATION

| | |
|---|---|
| AHED | ArcHydro Enhanced Database |
| ARF | areal reduction factor |
| DDF | depth-duration-frequency |
| GOF | goodness of fit |
| GP | generalized Pareto distribution |
| MCI | Model Climatology Index |
| ML | maximum likelihood |
| MQDM | multiplicative quantile delta mapping |
| MVI | Model Variability Index |
| NOAA | National Oceanic and Atmospheric Administration |
| PDS | partial-duration series |
| PRISM | Parameter-elevation Regressions on Independent Slopes Model |
| RCP | representative concentration pathway |
| SFMWD | South Florida Water Management District |
| $CF$ | change factor |
| $\hat{x}$ | quantile for the model projections for the future projection period |
| $m$ | model of interest |
| $p$ | future projection period of interest |
| $h$ | historical baseline period of interest |
| $F$ | annual nonexceedance probability function |
| $d$ | duration of interest (in days) |
| $A$ | spatial aggregation level (area, in kilometers) |

**Figure 4.** Methodology for deriving change factors for all downscaled datasets except JupiterWRF. (Modified from Irizarry-Ortiz and others, 2022).

useful when comparing simulated precipitation between datasets with different resolutions. As demonstrated by Chen and Knutson (2008), precipitation output from climate models should be interpreted as areal means rather than as point values, and their use and analysis should remain consistent with that interpretation. Otherwise, large differences in precipitation fields among datasets with different resolutions may be misinterpreted as bias. If the comparison is performed at consistent spatial scales, the true bias may be smaller or even of a different sign. In the computation of DDF change factors, described in the “Multiplicative Quantile Delta Mapping” section, current and future ARFs are assumed to be constant so that they would cancel out; however, ARFs are still useful when assessing model performance by comparing modeled extremes against observed extremes.

To evaluate the performance of modeled precipitation extremes from datasets of various resolutions by comparison against observational datasets for a chosen historical period in this study, grid-cell (areal) scale DDF curves were divided by ARFs to approximate station-scale (point-scale) DDF curves. The model-derived station-scale DDF curves for the historical period can then be compared to station-scale DDF curves from NOAA Atlas 14 volume 9 (Perica and others, 2013) or other sources. Because the station data used in developing the NOAA Atlas 14 DDF curves may include data for the period 1840–2008, depending on the station, all the precipitation data available from the historical period (1950–2005) of the downscaled climate datasets were used for this comparison. The two sets of historical DDF curves may not be completely comparable because of the differences inherent in the data and methods used to develop them, which include (1) different periods of record, and (2) different methods for DDF curve-fitting (regional frequency analysis on annual maximum series for NOAA Atlas 14 versus constrained maximum likelihood [CML] for the downscaled climate model datasets as discussed in Irizarry-Ortiz and others, 2022). Therefore, some differences between the two are to be expected.

Irizarry-Ortiz and others (2022) discuss known sources of ARF data and methods. In their study, geographically fixed-area ARF curves for climate regions across the State of Florida (fig. 5) were used to account for differences in spatial scale when comparing the model-derived station-scale DDF curves for the historical period to station-scale DDF curves from NOAA Atlas 14 volume 9 (Perica and others, 2013). Figure 6 shows the mean ARFs developed by Irizarry-Ortiz and others (2022) for 1-, 3-, and 7-day durations by ARF region (fig. 5). Also shown are error bars representing the mean ARF for each ARF region plus and minus one standard deviation of the grid-cell values within each ARF region. As expected, the mean ARF increases with increasing duration and its variability decreases. Overall, ARF values decrease from north to south Florida, and ARF values tend to be lower on the west coast of south Florida than on the east coast. As shown in figure 6, the ARF correction is close to 1 for most datasets, except for the CORDEX models and in particular for the coarser NAM-44i models.

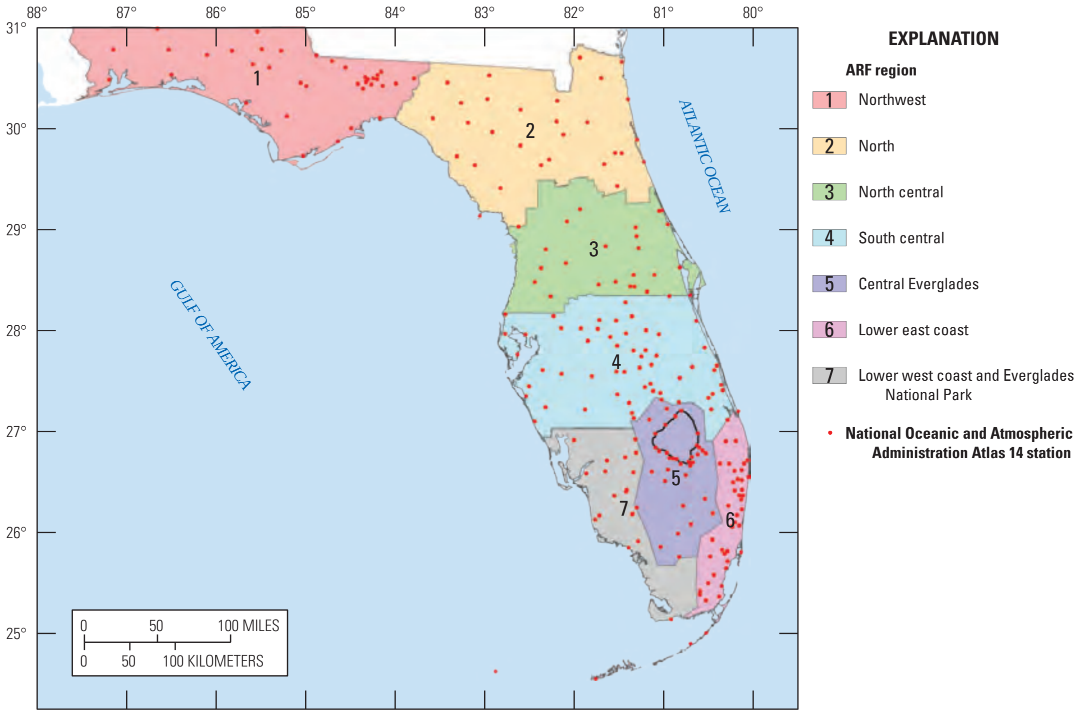

Base modified from U.S. Census Bureau Tiger database,
Florida County Boundaries, 1:100,000,1990
Geographic coordinate system
World Geodetic System 1984 datum

ARF regions from Irizarry-Ortiz and Haider (2023)

**Figure 5.** Areal reduction factor (ARF) regions for the State of Florida.

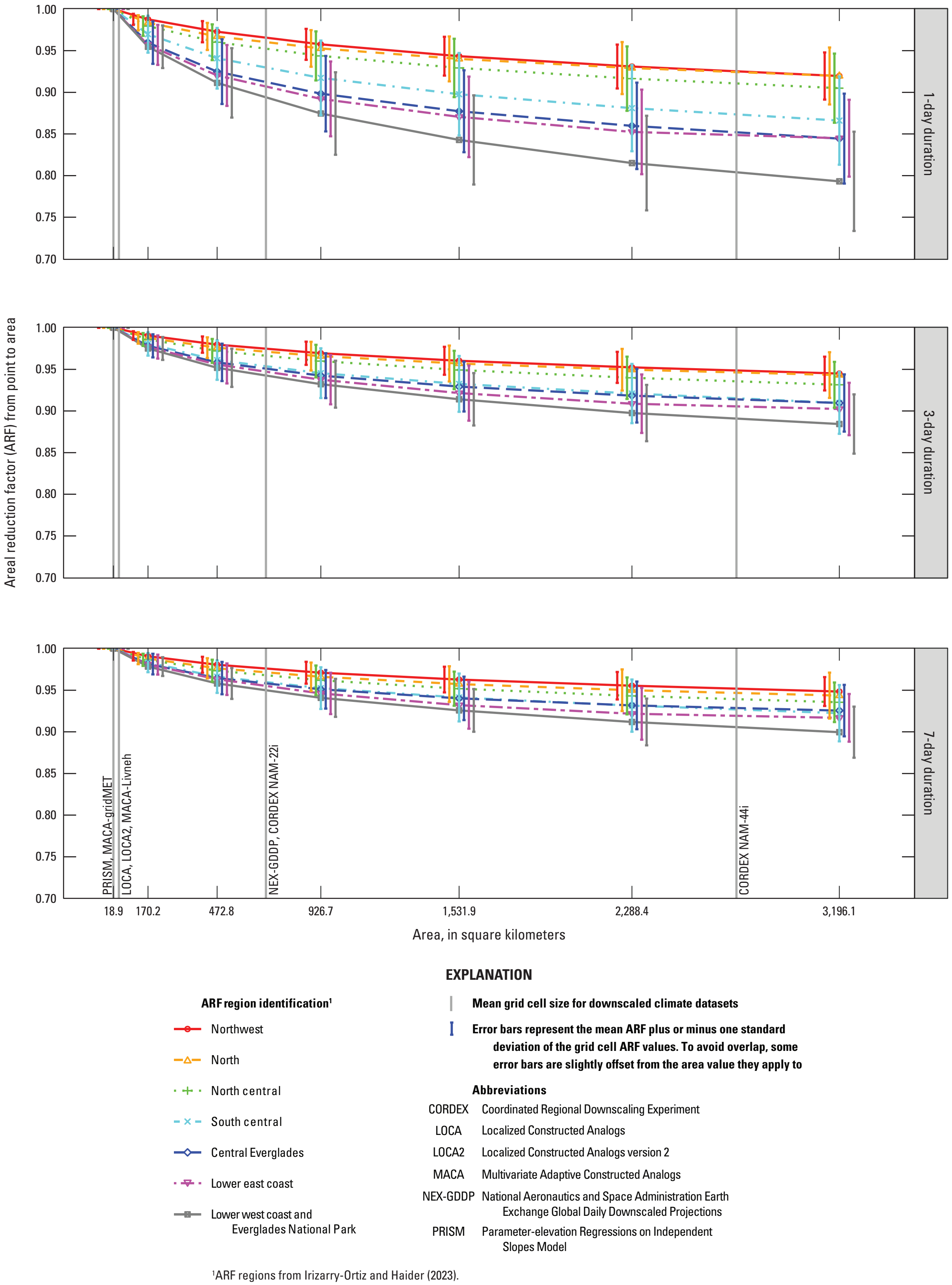

**Figure 6.** Mean areal reduction factors (ARFs), and associated standard deviation bars, by precipitation duration and ARF region for 1-, 3-, and 7-day durations. Modified from Irizarry-Ortiz and others (2022)

## Multiplicative Quantile Delta Mapping

Quantile mapping or CDF-matching methods (Panofsky and Brier, 1968) are often applied to bias-correct precipitation time series from climate model simulations, but the methods can similarly be used to bias-correct annual maximum series of precipitation or DDF curves. They can also be used as a form of statistical downscaling that attempts to bridge the scale mismatch between the model grid-cell estimates and the point observations. In this study, a MQDM approach (Wang and others, 2013; Cannon and others, 2015) is used to bias-correct projected future DDF curves. MQDM, as opposed to its additive version, is better suited to correcting variables such as precipitation where preserving relative changes is important to respect the Clausius-Clapeyron relation (Wallace and Hobbs, 2006), which relates the amount of atmospheric moisture to temperature changes. Lanzante and others (2021) confirmed the superiority of MQDM over its additive version by means of a “perfect model” experiment. The MQDM method is described in more detail by Irizarry-Ortiz and others (2022), and only the most relevant version of the equation is included in this manuscript:

$$\hat{x}_{m,p\ adj.} = F^{-1}_{m,p\ adj.}(F) = F^{-1}_{o,h}(F)\cdot\left[F^{-1}_{m,p}(F)/F^{-1}_{m,h}(F)\right], \qquad (1)$$

where

$\hat{x}_{m,p\ adj.}$ is the adjusted quantile for the model projections for the future projection period;

$m$ is the model of interest;

$p$ is the future projection period of interest;

$F^{-1}_{m,p\ adj.}$ is the inverse CDF (that is, the quantile function) of the adjusted model projections for the future projection period;

$F$ is equal to $F_{m,p}\left(\hat{x}_{m,p}\right)$, the annual nonexceedance probability for the model projections in the future projection period;

$\hat{x}_{m,p}$ is the quantile for the model projections in the future projection period;

$F^{-1}_{o,h}$ is the inverse of the CDF (that is, the quantile function) of the observations in the historical baseline period;

$o$ is the observation of interest;

$h$ is the historical baseline period of interest;

$F^{-1}_{m,p}$ is the inverse of the CDF of the model projections for the future projection period; and

$F^{-1}_{m,h}$ is the inverse of the CDF of the model in the historical baseline period.

The annual nonexceedance probability for the model projections in the future projection period ($F = F_{m,p}\left(\hat{x}_{m,p}\right)$) is related to the return period by the following relation:

$$F = 1 - P = 1 - 1/T, \qquad (2)$$

where

$T$ is the annual return period, in years; and

$P$ is the annual exceedance probability (AEP), which is equal to 1/$T$.

The term $F^{-1}_{m,p}\left(F\right)/F^{-1}_{m,h}\left(F\right)$ in equation 1 is the change factor for the particular nonexceedance probability (or return period), and duration. The assumption is that the relative change between historical and future projected conditions can be indicative of future changes in DDF curves even if the models are biased. The ultimate goal of this study is to obtain change factors from the historical period (1966–2005) to the future projection periods (2020–59 and 2050–89) across the locations of NOAA Atlas 14 stations in Florida. These change factors could then be applied to the PDS-based DDF curves from NOAA Atlas 14 to obtain future projected DDF curves.

NOAA Atlas 14 stations in the Florida Keys (08-2418, 08-4570, 08-5035, and 08-8841, defined in Irizarry-Ortiz and Haider, 2023) are inactive in most downscaled model grids (fig. 3). In such cases, data from the closest mainland grid cells to these four stations were used for developing DDF curves at these four locations. Although the NEX-GDDP dataset extends to the Florida Keys, the technical note for the dataset (Thrasher and others, 2021) warns that because of a lack of validation of its training dataset (GMFD) over oceans, downscaled values over small island areas might not be realistic. Therefore, change factors developed for these four locations in the Florida Keys are highly uncertain and should be used with caution.

## Derivation of Change Factors

The following is a description of the analytical steps used to derive change factors based on CORDEX, LOCA, MACA, LOCA2, and NEX-GDDP downscaled climate datasets (fig. 4). For each dataset, the closest grid cells to each of the 242 NOAA Atlas 14 stations in Florida were identified for each model. For each of these grid cells, rolling sums of daily precipitation were computed using R package RcppRoll (Ushey, 2018) to obtain the cumulative 3- and 7-day precipitation totals. This process was repeated for each climate model run for historical and future projection periods for each RCP or SSP scenario in each dataset. It is expected that all extreme values might be downward-biased because of their being constrained to a clock-based interval (that is, a consistent daily timestep). Therefore, rolling sums for the durations of interest were multiplied by correction factors (table 1; Perica and others, 2013) to convert constrained precipitation totals to unconstrained precipitation totals for each duration, that is, to the maximum precipitation for any time period of the given duration. Checks were made to ensure that the selected exceedances for each duration were larger than for shorter durations overall by comparing their CDFs.

The POT approach was used to fit the generalized Pareto (GP) probability distribution (Pickands, 1975; Leadbetter and others, 1983; Davison and Smith, 1990; Coles, 2001; Katz and others, 2002) to exceedances above a high threshold (fig. 4), as described by Irizarry-Ortiz and others (2022). In this study, thresholds were defined for every location (grid cell) on the basis of a percentile of the precipitation totals for each duration that would result in 2–3 exceedances per year ($\lambda$) for each duration after declustering; the chosen percentiles were 99th, 98th, and 97th for 1-, 3-, and 7-day durations, respectively. The runs declustering method in the extRemes package from R (Gilleland and Katz, 2016) was used with run lengths equal to the duration in days, plus 1 day (fig. 4). That is, run lengths of 2, 4, and 8 days were chosen for 1-, 3-, and 7-day durations, respectively. Our choice of run length for the 1-day event is similar to that of NOAA (2022a), which found that dependent events in the time series of exceedances do not affect the precipitation frequency estimates substantially and that declustering the daily exceedances using a 1-day separation period between exceedance events would be adequate. The run length is the number of threshold deficits to be considered as starting a new cluster. These run lengths were chosen to exclude neighboring (clustering) rolling-sum precipitation values that include the same high-precipitation days.

The extRemes package from R (Gilleland and Katz, 2016) was used to compute the interval-based extremal index of the exceedances declustered by the runs declustering method with prespecified run lengths. The objective of this exercise was to confirm that the exceedances declustered on the basis of prespecified run lengths were reasonably independent. A cutoff value of 0.7 for the interval-based extremal index, $\theta$, was assumed to be indicative of adequate tail independence. Additional statistical tests, such as the lag-1 Kendall autocorrelation coefficient (KACF; Durbin, 1960) and the Mann-Kendall trend test (MK; Mann, 1945; Kendall, 1970), were employed to determine whether precipitation excesses above a chosen threshold met the basic assumptions for POT, namely that the declustered excesses were independent and identically distributed. The GP was then fit to cluster maxima, hence the POT approach.

The GP was fitted one duration at a time using the traditional maximum likelihood (ML) approach and for all durations at once using the CML approach (Irizarry-Ortiz and others, 2022) at each model grid cell where a NOAA Atlas 14 station is located (fig. 4). In the CML approach, the GP shape and scale parameters are simulated as linear functions of duration and constraints are added to ensure that return levels for a given duration are larger than those for a shorter duration. The CML approach requires fitting two fewer parameters than the traditional ML approach (Irizarry-Ortiz and others, 2022). The resulting GP fits based on the CML approach are used to derive DDF curves by using the quantile function of the GP for each duration and converting the return periods of interest into nonexceedance probabilities. The tradeoff between model fit and parameter parsimony in the CML approach compared to the traditional ML approach is quantified by means of the Akaike Information Criterion (AIC; Akaike, 1973). In addition, a bootstrapping approach was used to determine goodness of fit (GOF) for the GP distribution (fig. 4) using the tests defined in Irizarry-Ortiz and others (2022): Kolmogorov-Smirnov, Anderson-Darling, Cramér-von Mises, the Pearson product moment correlation coefficient on probability-probability plots, and the Pearson product moment correlation coefficient on quantile-quantile plots. In addition to the GOF statistics described above, two other methods were used to determine whether the GP distribution is a reasonable distribution to model exceedances above a high threshold, as in Irizarry-Ortiz and others (2022). First, the gamlss R package (Rigby and Stasinopoulos, 2005) was used to fit all the available probability distributions in the package that can model real positive values. Second, an L-moment ratio diagram (Hosking, 1990; Vogel and Fennessey, 1993) was used to determine whether the excesses above the selected threshold at each location follow a GP distribution.

The resulting DDF curves apply at the grid-cell scale and are divided by appropriate ARFs to obtain station-scale values for both historical and future projection periods. Assuming the historical ARF applies to the future projection period, the ARF would cancel out in the computation of change factors; however, the ARF allows for comparison of the station-scale DDF curves fitted to simulated historical precipitation data as part of this study against the NOAA Atlas 14 PDS-based DDF curves that were fitted to historical observations of precipitation. Finally, the MQDM method (eq. 1) was used to compute change factors as the ratio of the future projected DDF precipitation depth to the historical DDF precipitation depth for each station grid cell in each downscaled climate dataset.

## Model Culling

Model culling refers to the process by which some models are eliminated from further analysis, and the remaining subset of climate models (referred to as “best” models, hereafter) are selected to inform future changes in impact-relevant climate variables (such as used by Infanti and others, 2020). The “best” models are determined by a series of performance measures of relevance to the region and variables of interest. The performance measures are typically based on how well the models reproduce historical observations at weather stations or in comparison to observational gridded products in the region of interest. For this study, precipitation extremes and their return periods in Florida are of the utmost importance to meet the study objective. The use of the word “best” within quotes is to emphasize that these models are the ones that best reproduce historical observations for the limited set of performance measures evaluated, but we do not imply that these models would necessarily perform best in simulating all aspects of the historical or future climate or result in the most accurate change factors.

The Expert Team on Climate Change Detection and Indices (ETCCDI; further information available at http://etccdi.pacificclimate.org/list_27_indices.shtml) has defined climate extremes indices on the basis of daily precipitation data. The original ETCCDI indices and variations thereof (Zhang and others, 2011) have been used by many researchers worldwide to assess the performance of GCMs and downscaled climate products (see, for example, Donat and others, 2013; Sillmann and others, 2013a, b; Srivastava and others, 2020). Several ETCCDI precipitation extreme indices were selected to quantify model performance, as documented in table 3. The ETCCDI precipitation extreme indices were supplemented with additional indices of relevance to this study, as listed in table 3. Preliminary evaluation of precipitation extreme indices for the various downscaled climate datasets used in this study showed correlation between some of the indices, and only a small number of models remained when model culling was based on all the indices listed in table 3. To include as many models as possible to inform the potential range of change factors, a decision was made to only use four precipitation extremes indices in selecting the "best" models (fig. 4). These selected indices consist of annual maxima of consecutive precipitation for durations of 1, 3, 5, and 7 days, and are the most relevant to the estimation of precipitation extremes.

Two reference observational datasets were used to evaluate historical precipitation extremes indices in this study: the SFWMD "Super-grid" and PRISM. Various studies have found that the model performance in capturing climate extremes indices varies depending on the reference dataset chosen (Gleckler and others, 2008; Sillmann and others, 2013a, b; Donat and others, 2014; Wang and others, 2020). The SFWMD "Super-grid" and PRISM observational datasets were chosen for validation of precipitation extreme indices instead of the gridded observational precipitation datasets used in bias correction of the downscaled datasets (Livneh, Daymet, gridMET, Livneh unsplit, and GMFD). As discussed by Irizarry-Ortiz and others (2022), PRISM was chosen on the basis of Behnke and others (2016), who identified it as one of the best performing datasets at capturing daily precipitation statistics and most climate extremes indices at meteorological stations in Florida, whereas the SFWMD "Super-grid"

**Table 3.** Extreme precipitation indices evaluated in this study.

[All indices are recommended by the Expert Team on Climate Change Detection and Indices (2009) except those indicated as supplemental indices. ID, identifier; mm, millimeter; ≥, greater than or equal to; <, less than]

| Index ID | Index name | Index definition | Unit of measure |
|---|---|---|---|
| PRCPTOT | Annual total wet day precipitation | Annual total precipitation from days with precipitation ≥ 1 mm | Inches |
| R1mm[1] | Number of wet days | Annual count of days with precipitation ≥ 1 mm | Days |
| R10mm | Number of heavy precipitation days | Annual count of days with precipitation ≥ 10 mm | Days |
| R20mm | Number of very heavy precipitation days | Annual count of days with precipitation ≥ 20 mm | Days |
| SDII | Simple daily intensity index | Ratio of annual total precipitation to the number of wet days (≥ 1 mm) (PRCPTOT/R1mm) | Inches per day |
| CDD | Consecutive dry days | Maximum number of consecutive days when precipitation < 1 mm in a year | Days |
| CWD | Consecutive wet days | Maximum number of consecutive days when precipitation ≥ 1mm in a year | Days |
| RX1day[2,3] | Max 1-day precipitation amount[3] | Annual maximum 1-day precipitation | Inches |
| RX3day[1,2,3] | Max 3-day precipitation amount[3] | Annual maximum consecutive 3-day precipitation | Inches |
| RX5day[2,3] | Max 5-day precipitation amount[3] | Annual maximum consecutive 5-day precipitation | Inches |
| RX7day[1,2,3] | Max 7-day precipitation amount[3] | Annual maximum consecutive 7-day precipitation | Inches |
| R95p | Very wet days | Annual total precipitation from days ≥ 95th percentile in the base period | Inches |
| R95pTOT[1] | Contribution from very wet days | 100 * R95p / PRCPTOT | Percent |
| R99p | Extremely wet days | Annual total precipitation from days ≥ 99th percentile in the base period | Inches |
| R99pTOT[1] | Contribution from extremely wet days | 100 * R99p / PRCPTOT | Percent |

[1] Supplemental index of relevance to this study that are not part of the original list from the Expert Team on Climate Change Detection and Indices (ETCCDI; Zhang and others, 2011).

[2] Used to cull models for this study.

[3] Used in selecting "best" models in this study for reproducing historical observations based on index of performance.

dataset was developed by the SFWMD to cover nearly the entire SFWMD and with a long enough record to allow for analysis of trends (SFWMD, 2005). In this study, the common 25-year historical period between PRISM and the downscaled datasets (1981–2005) was chosen as the base period for computation of percentiles in the percentile-based indices and for calculation and performance evaluation of the precipitation extremes indices.

The precipitation extremes indices were calculated using Python code developed by Gibson (2021). The Python code relies on Python bindings (Max Planck Institute for Meteorology, 2022b) to CDO. The CDO utility remapnn (Max Planck Institute for Meteorology, 2022c) was used to remap the climate indices computed for the downscaled climate datasets to the grids of the PRISM and SFWMD ”Super-grid” datasets using nearest-neighbor interpolation. This interpolation method was used so as not to add information to the downscaled climate datasets that was not already there. In essence, the assumption was made that the grid-cell values from the downscaled climate datasets represent mean values over the grid cell (see Chen and Knutson, 2008), and the node value was assigned to all PRISM and SFWMD “Super-grid” locations having their centroid within a model grid cell. Although the resolution of the indices may be the same for the reference and downscaled datasets after remapping, differences in climate indices are to be expected because of differences in the native scale of each dataset and the order of steps followed in remapping (that is, climate index computation first, followed by remapping, or vice versa). Climate indices for the reference datasets represent the approximately 4- or 3.2-km spatial mean of daily station precipitation that was used for each PRISM or SFWMD “Super-grid” cell, respectively. In contrast, climate indices for CORDEX, for example, were calculated from the 25- to 50-km daily precipitation simulated for each CORDEX grid cell and then assigned to all PRISM or SFWMD “Super-grid” cells located within the area of the CORDEX grid cell.

To summarize the spatial pattern match of each climate index in the downscaled datasets to the reference dataset, various performance measures from Gleckler and others (2008), Sillmann and others (2013a), and Srivastava and others (2020) were used. These performance measures were evaluated separately for five distinct climate regions in Florida (fig. 2). The climate regions were defined as the NOAA (2011) U.S. Climate Divisions for the State of Florida, with Florida climate divisions 5, 6, and 7 merged into a single region named “south Florida” hereafter. Guttman and Quayle (1996) explain the history behind U.S. climate divisions.

The root-mean-square error (RMSE) statistic is used to summarize the performance of each model in capturing the climatology (long-term mean for 1981–2005) of each index calculated from the reference dataset at the model resolution:

$$RMSE_{m,I} = \sqrt{\frac{1}{C}\sum_{c=1}^{C}\left(\overline{I_{m,c}} - \overline{I_{o,c}}\right)^2}\ , \qquad (3)$$

where

| | |
|---|---|
| $RMSE_{m,I}$ | is the RMSE statistic for climate index $I$ in model $m$, |
| $c$ | is the index for a grid cell in model $m$, |
| $C$ | is the number of grid cells in model $m$, |
| $\overline{I_{m,c}}$ | is the climatological mean of index $I$ at grid cell $c$ for model $m$ after remapping to the scale of the observational dataset, and |
| $\overline{I_{o,c}}$ | is the climatological mean of index $I$ at grid cell $c$ for the reference observational dataset $o$. |

The best models will have a small $RMSE_{m,I}$. The relative performance of a model in simulating the climatological mean of the reference observational dataset can be computed by normalizing the $RMSE_{m,I}$ as follows:

$$NRMSE_{m,I} = \frac{RMSE_{m,I} - RMSE_{med,I}}{RMSE_{med,I}}, \qquad (4)$$

where

| | |
|---|---|
| $NRMSE_{m,I}$ | is the normalized RMSE statistic for climate index $I$ in model $m$, and |
| $RMSE_{med,I}$ | is the median of the RMSE statistic across all models in a particular downscaled climate dataset for climate index $I$. |

The median is used for normalization to avoid undue influence by outlier models having unusually large errors. The best models will have a large negative $NRMSE_{m,I}$, indicating that the model performs better than most models. A large positive $NRMSE_{m,I}$ indicates that the model performs worse than most models. To quantify the overall performance of a model in simulating the climatological mean of all indices, the Model Climatology Index (MCI) from Srivastava and others (2020) was used, but it was modified to use the mean of the $NRMSE_{m,I}$ values over all indices for a particular model as opposed to the median.

In addition to the spatial pattern in the climatological mean, it is important to quantify how different models capture the spatial pattern of the interannual variability of each climate index from gridded observations. For this purpose, the interannual variability skill score (IVSS; Chen and others, 2011; Jiang and others, 2015) was used, which is defined as

$$IVSS_{m,I} = \frac{1}{C}\sum_{c=1}^{C}\left(\frac{\sigma_{I,m,c}}{\sigma_{I,o,c}} - \frac{\sigma_{I,o,c}}{\sigma_{I,m,c}}\right)^2, \qquad (5)$$

where

| | |
|---|---|
| $IVSS_{m,I}$ | is the interannual variability skill score statistic for climate index $I$ in model $m$, |
| $\sigma_{I,m,c}$ | is the interquartile range (difference between 75th and 25th percentile) of index $I$ at grid cell $c$ for model $m$ after remapping to the scale of the observational dataset, and |

$\sigma_{I,o,c}$ is the interquantile range (difference between 75th and 25th percentile) of index $I$ at grid cell $c$ for the reference observational dataset $o$.

The best models will have a small $IVSS_{m,I}$. The relative performance of a model in simulating the interquartile range of the reference observational dataset can be computed by normalizing the $IVSS_{m,I}$ as follows:

$$NIVSS_{m,I} = \frac{IVSS_{m,I} - IVSS_{med,I}}{IVSS_{med,I}}, \tag{6}$$

where

$NIVSS_{m,I}$ is the normalized interannual variability skill score for climate index $I$ in model $m$, and

$IVSS_{med,I}$ is the median, *med*, of the interannual variability skill score across all models in a particular downscaled climate dataset for climate index $I$.

The best models will have a large negative $NIVSS_{m,I}$, indicating that the model performs better than most models. A large positive $NIVSS_{m,I}$ indicates that the model performs worse than most models. To quantify the overall performance of a model in simulating the interannual variability of all indices, the Model Variability Index (MVI) from Srivastava and others (2020) was used but was modified to use the mean of the $NIVSS_{m,I}$ values over all indices for a particular model as opposed to the median. Lastly, the MCI and MVI for each model were plotted as a scatterplot, with the best performing models having the largest negative MCI and MVIs.

In this report, only results considering all models are presented; however, the list of best models and results, such as change factor quantiles considering only best models, are included in the data release associated with this report (Irizarry-Ortiz and Haider, 2023).

# Results

Change factors were derived for extreme precipitation events from the output of six downscaled models at grid cells closest to the 242 weather stations used in the NOAA Atlas 14 analyses for Florida. Future changes in the timing of extreme events may or may not correlate directly with changes in the annual cycle of precipitation. Figures 7–11 show the annual cycle of mean monthly precipitation for the historical period (1966–2005) and the two future periods (2020–59 and 2050–89), as simulated in each of the six downscaled climate datasets for the five climate regions in the State of Florida (fig. 2). Data from the KACE-1-0-G_r1i1p1f1 GCM are excluded from the NEX-GDDP dataset in figure 10 because they show much lower precipitation in January and February than do the remaining models and observational datasets during the historical period. Increasing precipitation seasonality is evident from northwest to south Florida in figures 7–11. The range of the annual cycle of mean monthly precipitation in historical simulations from different climate models in each downscaled climate dataset tends to match the annual cycle of precipitation from PRISM, the SFWMD “Super-grid,” and the datasets used in bias correction reasonably well. Each downscaled climate dataset was bias-corrected to different gridded observational datasets; therefore, as expected, they tend to match the dataset that they were bias-corrected to better than they match PRISM and the SFWMD “Super-grid” in the historical period. The variability shown in the historical simulations might be due, at least in part, to the different period used in bias-correcting each downscaled climate dataset than the 40-year historical period chosen here for DDF calculation.

Srivastava and others (2022) show that raw precipitation data from the CORDEX models prior to bias correction do not to capture the annual cycle of mean monthly precipitation in Florida, with some models completely out of phase or not able to capture the cycle’s amplitude. Most CORDEX RCMs evaluated by Srivastava and others (2022) underestimate precipitation from June through August and overestimate it during the rest of the year. The bias-correction algorithm used by CORDEX generally corrects the seasonality problem, as shown in figure 7.

As discussed in Irizarry-Ortiz and others (2022), the use of a 3-month sliding window for bias-correcting each central month in CORDEX (Cannon, 2018) results in more variability in the historical simulations than for other datasets (figs. 7–11). The use of a 3-month sliding window also results in a general overestimation of precipitation during the wet-dry season transition months of May and October and an underestimation in June in CORDEX, especially for the two southernmost Florida climate regions. Future projections for different climate models in each downscaled climate dataset (figs. 7–11) vary widely in wet-season precipitation for all climate regions and periods. However, the future projected range of wet-season precipitation is more compact in CORDEX (fig. 7), which is possibly a result of fewer GCMs downscaled by CORDEX (eight) than in other downscaled climate datasets.

The median projected change in the annual cycle of mean monthly precipitation from the historical period (1966–2005) to the future periods (2020–59 and 2050–89) (fig. 12) indicates a shift in seasonality of increasing amplitude from north to south Florida. Projected reductions in June–August precipitation and increases in precipitation during the transitional months of May and October are especially evident in central and south Florida. The projected increase in May precipitation is more marked in the CMIP6 datasets (LOCA2 and NEX-GDDP) than in the CMIP5 datasets. The projected seasonality changes are more marked in the period 2050–89 than in the earlier period, 2020–59, especially in central and south Florida. The projected decline in summer precipitation in south Florida is consistent with GCM projections of summertime drying of the Caribbean region extending into

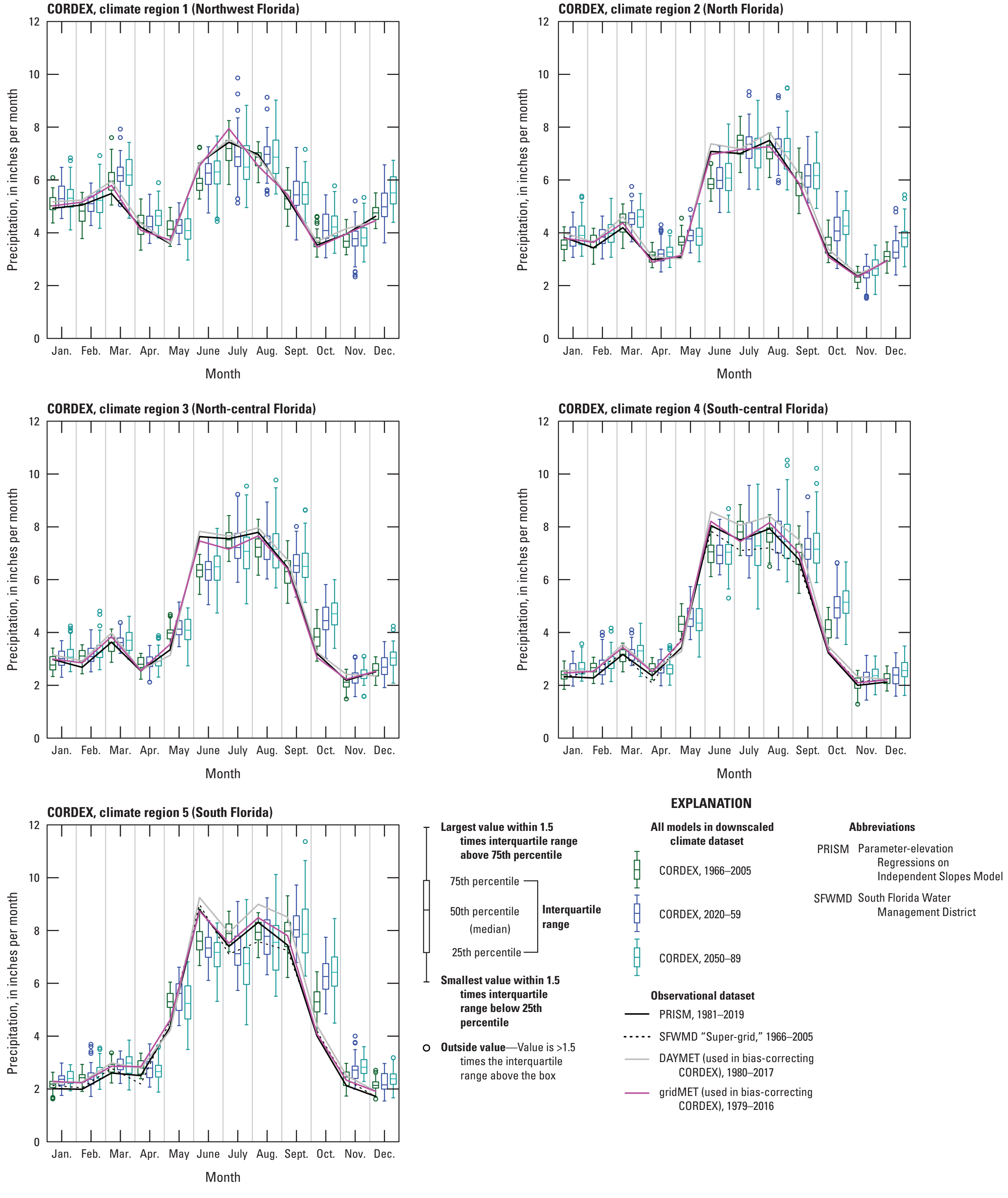

**Figure 7.** Annual cycle of mean monthly precipitation for the historical period (1966–2005) and the two future periods (2020–59 and 2050–89), as simulated for all models in the Coordinated Regional Downscaling Experiment (CORDEX) dataset for the Florida climate regions in figure 2. Annual cycle of mean monthly precipitation for observational datasets shown for comparison. The green, blue, and cyan boxplots are the annual cycle of mean monthly precipitation for the historical (1966–2005) and the two future projection periods (2020–59, 2050–89), respectively, for all models. On the graph, the historical observations are aligned with the corresponding historical boxplots on the horizontal axis.

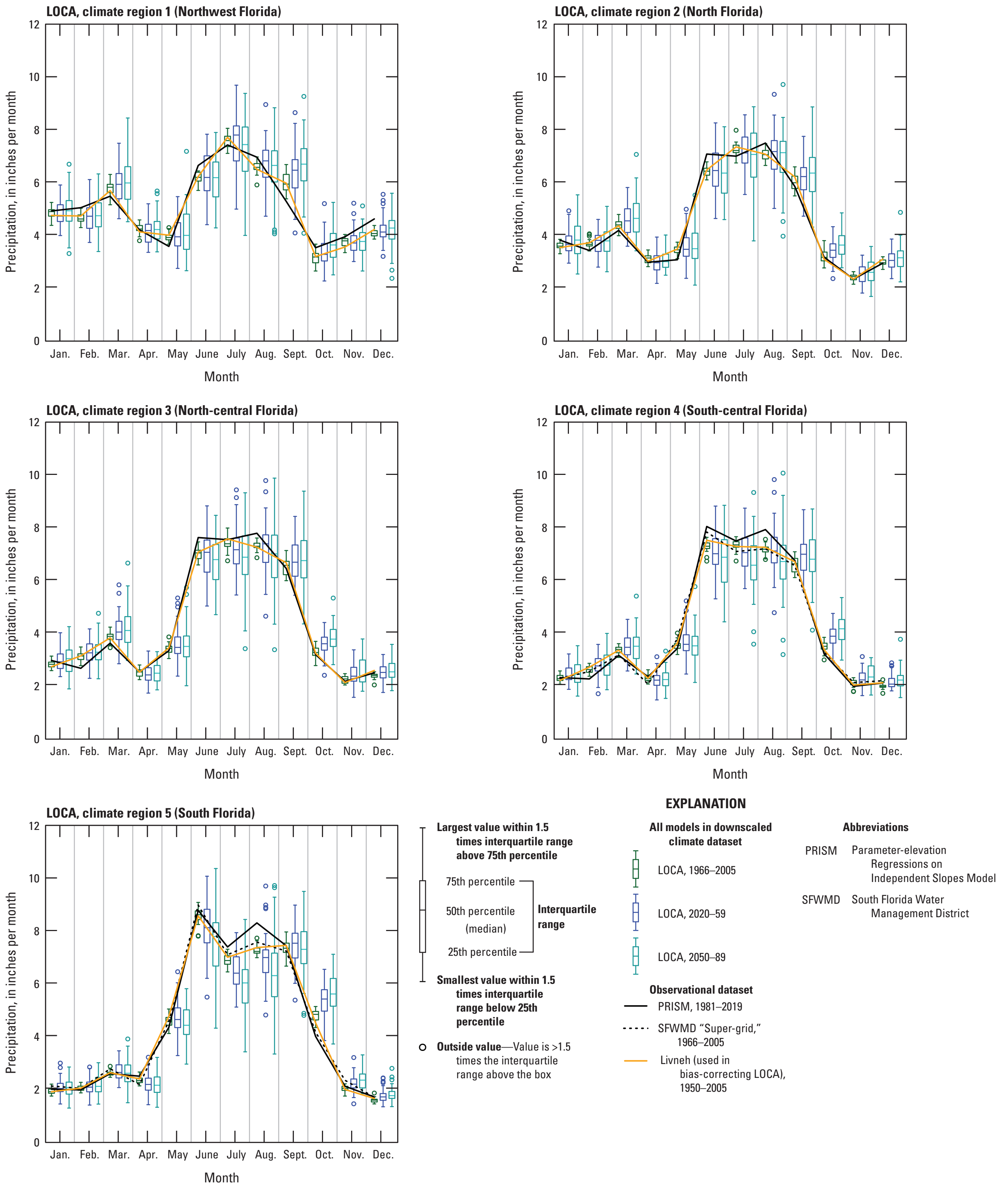

**Figure 8.** Annual cycle of mean monthly precipitation for the historical period (1966–2005) and the two future periods (2020–59 and 2050–89) as simulated in the Localized Constructed Analogs (LOCA) dataset for the Florida climate regions in figure 2. Annual cycle of mean monthly precipitation for observational datasets shown for comparison. The green, blue, and cyan boxplots are the annual cycle of mean monthly precipitation for the historical (1966–2005) and the two future projection periods (2020–59, 2050–89), respectively, for all models. On the graph, the historical observations are aligned with the corresponding historical boxplots on the horizontal axis.

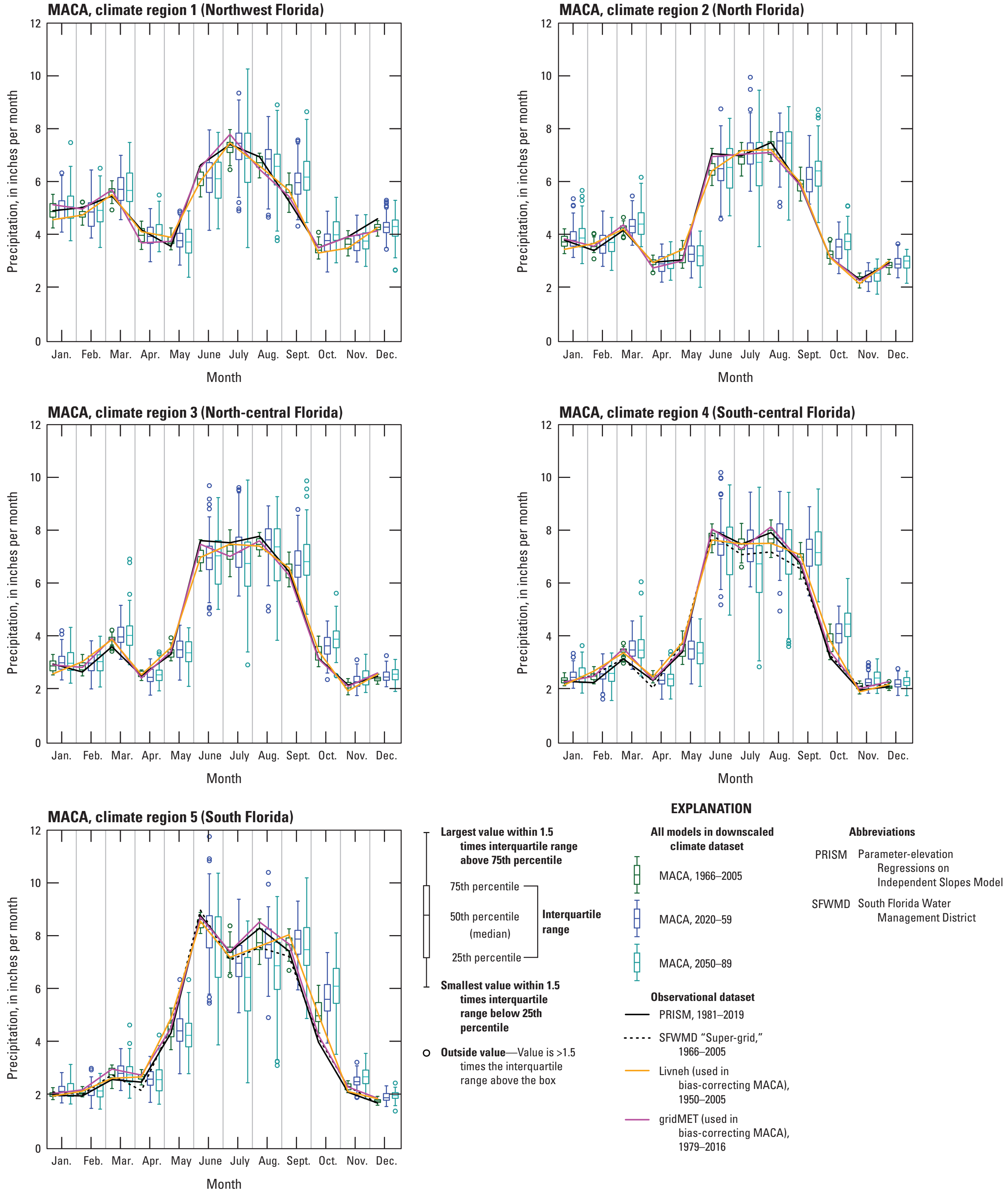

**Figure 9.** Annual cycle of mean monthly precipitation for the historical period (1966–2005) and the two future periods (2020–59 and 2050–89) as simulated in the Multivariate Adaptive Constructed Analogs (MACA) dataset for the Florida climate regions in figure 2. Annual cycle of mean monthly precipitation for observational datasets shown for comparison. The green, blue, and cyan boxplots are the annual cycle of mean monthly precipitation for the historical (1966–2005) and the two future projection periods (2020–59, 2050–89), respectively, for all models. On the graph, the historical observations are aligned with the corresponding historical boxplots on the horizontal axis.

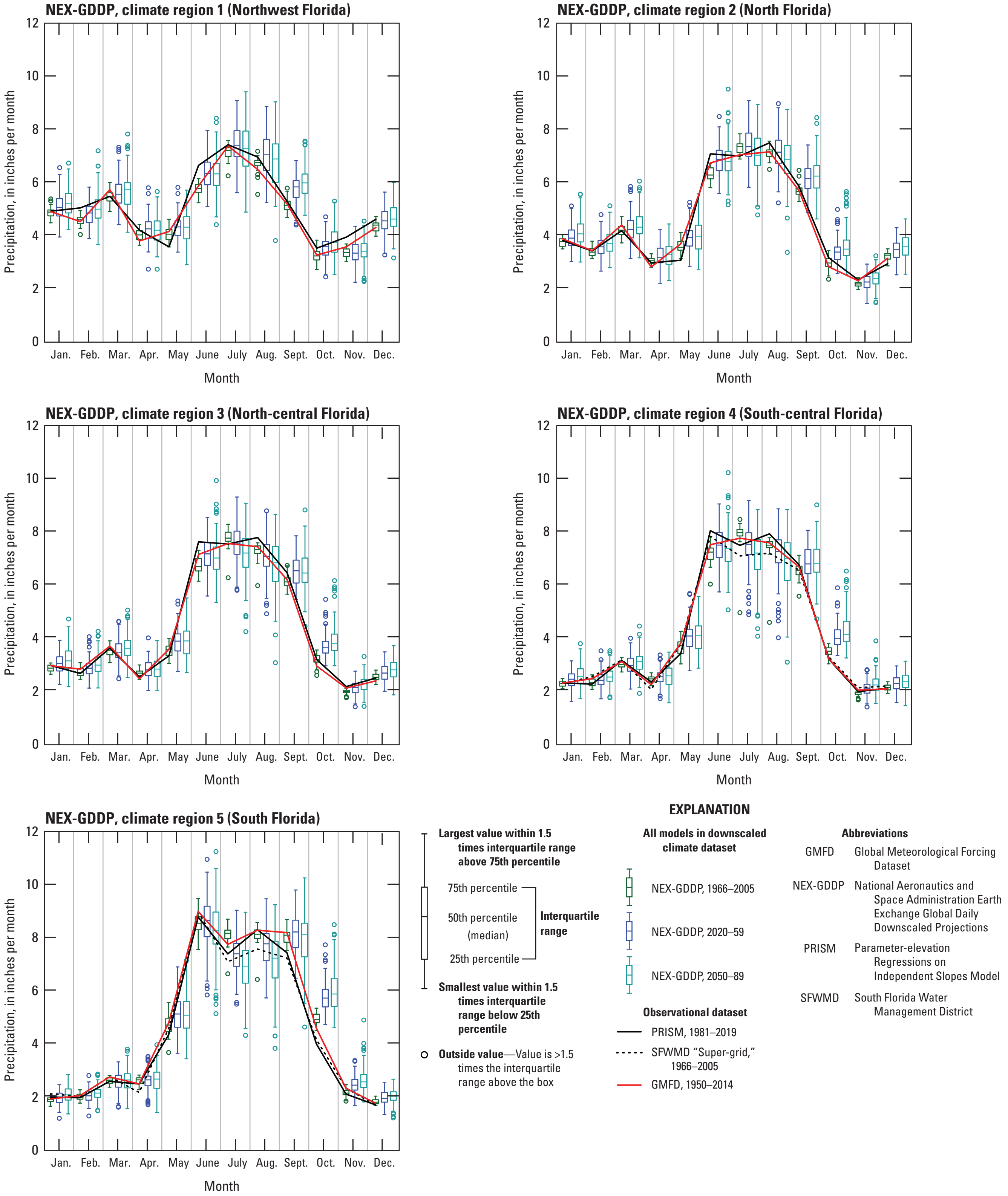

**Figure 10.** Annual cycle of mean monthly precipitation for the historical period (1966–2005) and the two future periods (2020–59 and 2050–89) as simulated in the National Aeronautics and Space Administration Earth Exchange Global Daily Downscaled Projections (NEX-GDDP) dataset for the Florida climate regions in figure 2. Annual cycle of mean monthly precipitation for observational datasets shown for comparison. The green, blue, and cyan boxplots are the annual cycle of mean monthly precipitation for the historical (1966–2005) and the two future projection periods (2020–59, 2050–89), respectively, for all models. On the graph, the historical observations are aligned with the corresponding historical boxplots on the horizontal axis.

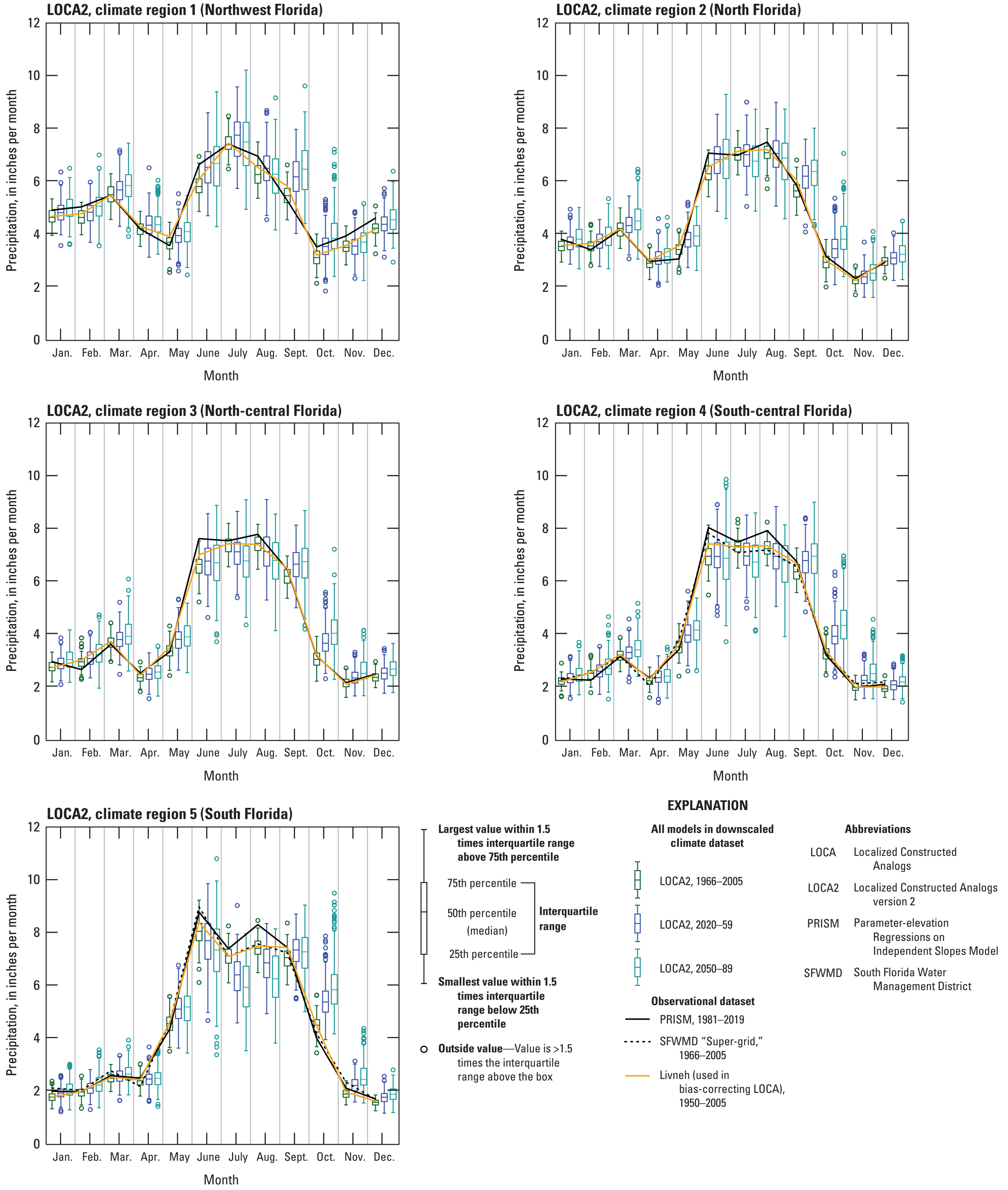

**Figure 11.** Annual cycle of mean monthly precipitation for the historical period (1966–2005) and the two future periods (2020–59 and 2050–89) as simulated in the Localized Constructed Analogs version 2 (LOCA2) dataset for the Florida climate regions in figure 2. Annual cycle of mean monthly precipitation for observational datasets shown for comparison. The green, blue, and cyan boxplots are the annual cycle of mean monthly precipitation for the historical (1966–2005) and the two future projection periods (2020–59, 2050–89), respectively, for all models. On the graph, the historical observations are aligned with the corresponding historical boxplots on the horizontal axis.

southern portions of peninsular Florida (Misra and others 2011; Collins and others, 2013; Byrne and others, 2018; Taylor and others, 2018; Campbell and others, 2021).

The CMIP6 datasets (LOCA2 and NEX-GDDP) project increases in precipitation in northwest Florida during all months in both future periods, but only for the future period 2020–59 in north Florida (fig. 12); however, both datasets project an overall increase in annual total precipitation in both climate regions. A larger or longer-lasting decline in summertime precipitation for north and north-central Florida is projected by the CMIP6 datasets than the CMIP5 datasets, especially for the period 2050–89. In particular, the CMIP6 datasets project declines in July and August precipitation in these two climate regions, whereas the CMIP5 datasets only project declines in July precipitation. Median projected changes in annual precipitation (fig. 12) are relatively small; however, larger increases in annual precipitation are projected for northwest Florida, with smaller increases toward the south. In general, LOCA2 projects the largest increases in annual precipitation, whereas LOCA and MACA project the smallest increases, and even decreases, for south-central and south Florida in the period 2050–89.

## Declustering and Partial-Duration Series

Extreme precipitation events were identified as those exceeding the 99th, 98th, and 97th percentiles of precipitation for 1-, 3-, and 7-day durations, respectively. After declustering the precipitation exceedances using run lengths equal to the duration plus 1 day, it was determined that more than 95 percent of the grid cells had an extremal index (as calculated from the intervals method of Ferro, 2003; and Ferro and Segers, 2003) of 0.7 or greater in all periods, durations, and models in all downscaled climate datasets. The inverse of the extremal index provides an estimate of the mean cluster size (Moloney and others, 2019); therefore, an extremal index of 0.7 would correspond to mean cluster size of 1.4. This increases confidence that the declustering was adequate for the great majority of cells. This approach was applied to the CORDEX, LOCA, MACA, LOCA2, and NEX-GDDP downscaled climate datasets. After declustering, the CML approach was used to fit the GP distribution to declustered precipitation excesses for durations of 1, 3, and 7 days, for the periods 2050–89 and 1966–2005 at every grid cell closest to each of the 242 NOAA Atlas 14 stations in Florida.

As discussed by Winsberg (2020) and Irizarry-Ortiz and others (2022), the historical monthly frequency distribution of extreme precipitation is bimodal over most of the State, peaking in June and September. Winsberg (2020) explained the June peak as resulting from the Intertropical Convergence Zone moving north and having more influence on the local weather and the September peak as resulting from the greater frequency of tropical storms reaching the State during that month, which corresponds to the peak of the Atlantic hurricane season. Figures 13–15 show the median change in the annual cycle of the mean monthly number of declustered threshold exceedance events from the historical period (1966–2005) to the future periods (2020–59 and 2050–89) for durations of 1, 3, and 7 days, as simulated in each downscaled climate dataset for the climate regions shown in figure 2. The percentile-based historical threshold is used to define the number of exceedance events for both the historical and future periods. For example, the 99th percentile value chosen as the threshold to define extreme 1-day events in the historical period (fig. 13) corresponds to about 3.6 extreme precipitation events per year on average. Those 3.6 extreme events in an average year have an associated annual cycle (Winsberg, 2020) with less than one extreme event happening per month on average (see Irizarry-Ortiz and others, 2022). Therefore, figure 13 shows the median changes across models in the mean monthly number of exceedances of the threshold value defined by the 99th percentile of the historical data. Figures 14–15 can be interpreted in a similar manner to the above explanation for figure 13; however, they correspond to 3- and 7-day extreme events defined as those exceeding the 98th and 97th percentiles, respectively. Note that in fitting the GP distribution, different percentile-based thresholds are used for the historical and future periods. When the percentile-based historical threshold is used to define exceedance events for the historical and future periods, as in figures 13–15, the median change in the annual number of threshold exceedance events from the historical to the future periods is generally positive for most datasets, climate regions, durations, and periods. This means that an increase in the number of extreme events is projected, especially for the northernmost climate regions and for the latter period 2050–89.

Overall, the median change in the number of future exceedance events for all durations (figs. 13–15) follows a similar seasonal pattern as the projected median changes to the mean annual cycle of precipitation (fig. 12). The similarity in seasonal changes between overall precipitation and the number of future exceedance events is more evident for the 7-day duration (fig. 15), whereas changes for 1- and 3-day durations are more erratic, although a seasonal pattern can still be discerned. The number of future exceedance events is generally projected to increase during the dry season, particularly during the transitional months for the longer durations, and decrease during the wet season, especially in the south. The annual number of future exceedance events is projected to increase the most according to the CORDEX and NEX-GDDP datasets and the least according to the LOCA and MACA datasets. The annual number of future exceedance events is projected to increase the most in the northern climate regions and less so further south because of decreases in the number of events during the wet season in the south, particularly in the period 2050–89.

## Goodness of Fit

The AIC is used to quantify goodness of fit. For each grid-cell location corresponding to NOAA Atlas 14 stations in every downscaled model, the change in AIC ($\Delta AIC$) was

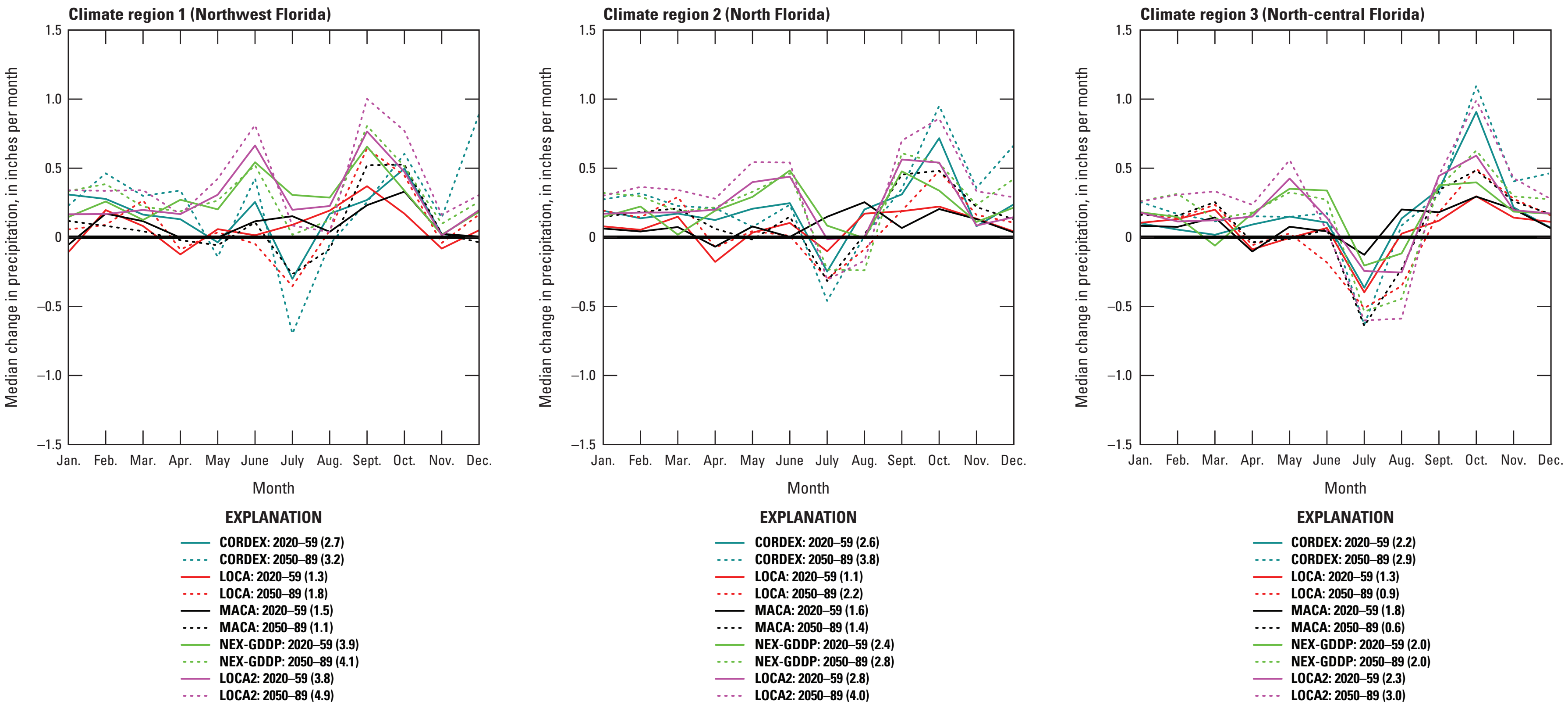

**Figure 12.** Median change in the annual cycle of mean monthly precipitation from the historical period (1966–2005) to the two future periods (2020–59 and 2050–89) as simulated in each downscaled climate dataset for the Florida climate regions shown in figure 2. Values in parentheses next to each dataset represent the median change in annual precipitation, in inches per year, from the historical period to the future period. CORDEX, Coordinated Regional Downscaling Experiment; LOCA, Localized Constructed Analogs; LOCA2, Localized Constructed Analogs version 2; MACA, Multivariate Adaptive Constructed Analogs); NEX-GDDP, National Aeronautics and Space Administration Earth Exchange Global Daily Downscaled Projections.

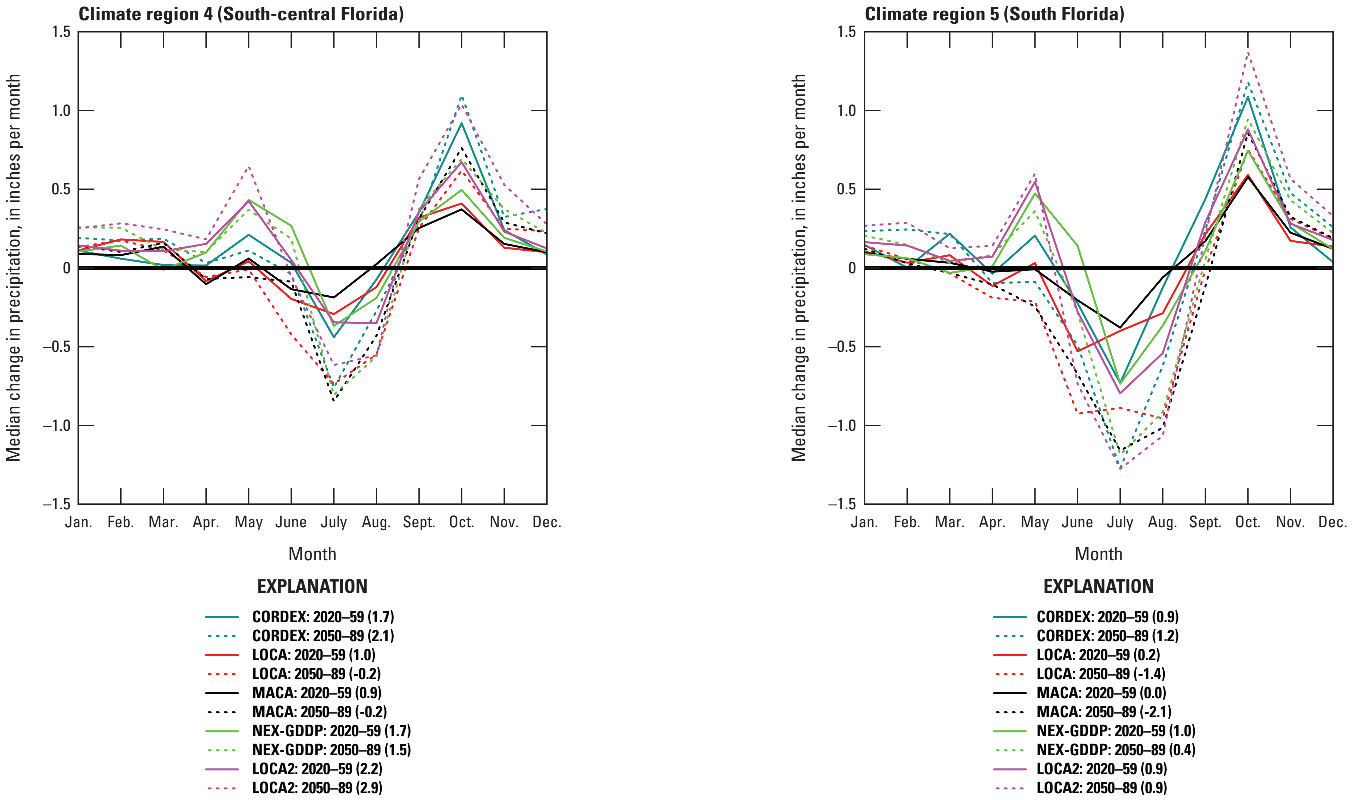

**Figure 12.**—Continued

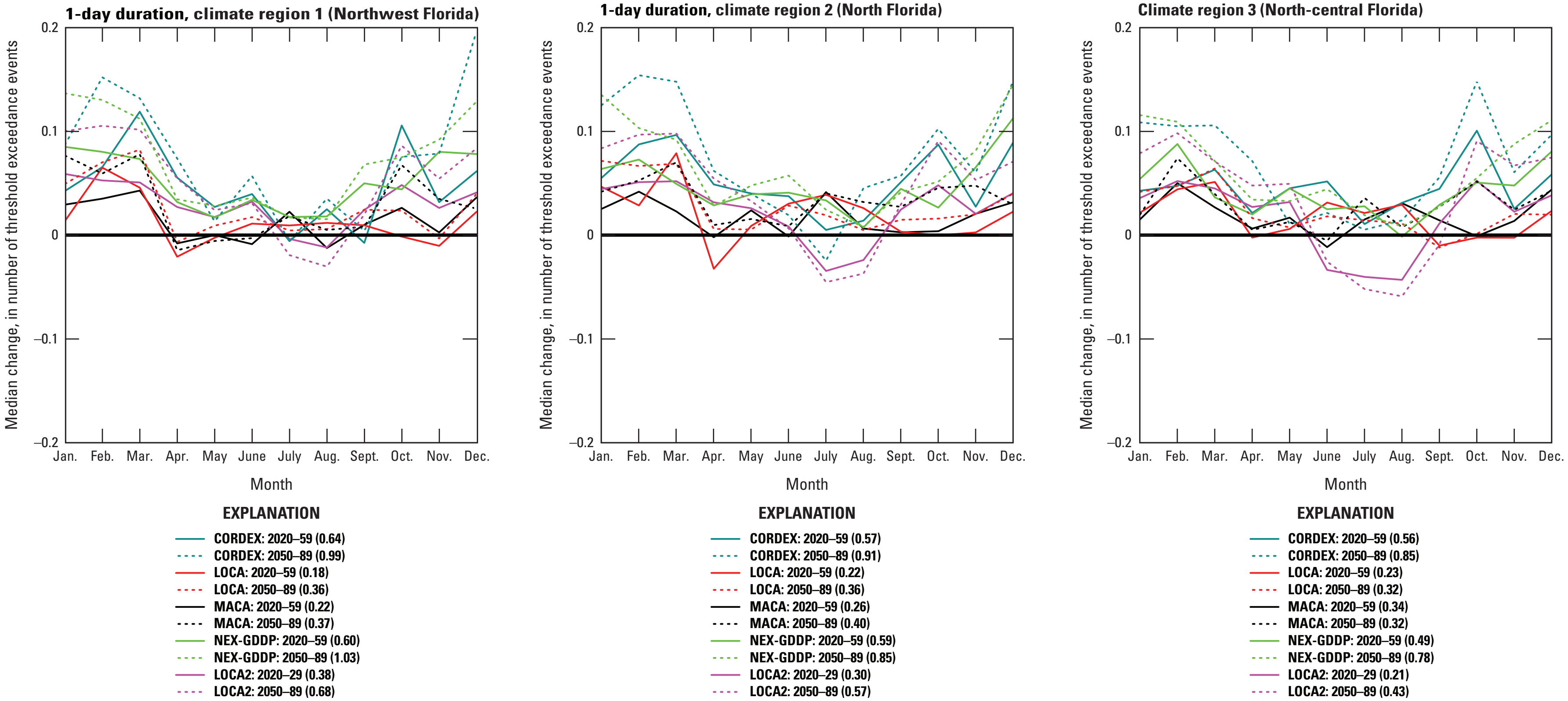

**Figure 13.** Median change in the mean annual cycle of the monthly number of declustered threshold exceedance events from the historical period (1966–2005) to the two future periods (2020–59 and 2050–89) for 1-day duration, as simulated in each downscaled climate dataset for the Florida climate regions in figure 2. Values in parentheses next to each dataset represent the median change in the annual number of declustered threshold exceedance events from the historical period to the future period. CORDEX, Coordinated Regional Downscaling Experiment; LOCA, Localized Constructed Analogs; LOCA2, Localized Constructed Analogs version 2; MACA, Multivariate Adaptive Constructed Analogs); NEX-GDDP, National Aeronautics and Space Administration Earth Exchange Global Daily Downscaled Projections.

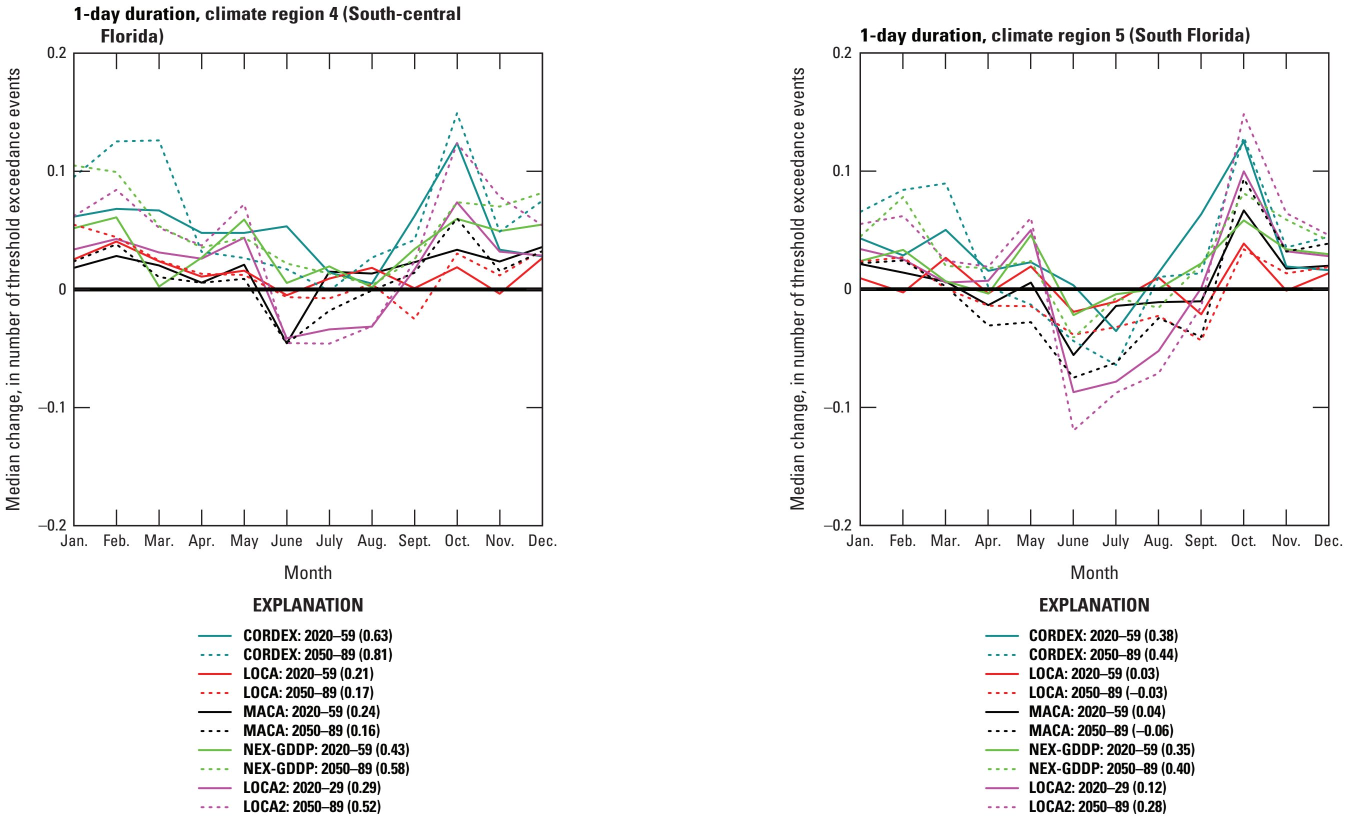

**Figure 13.**—Continued

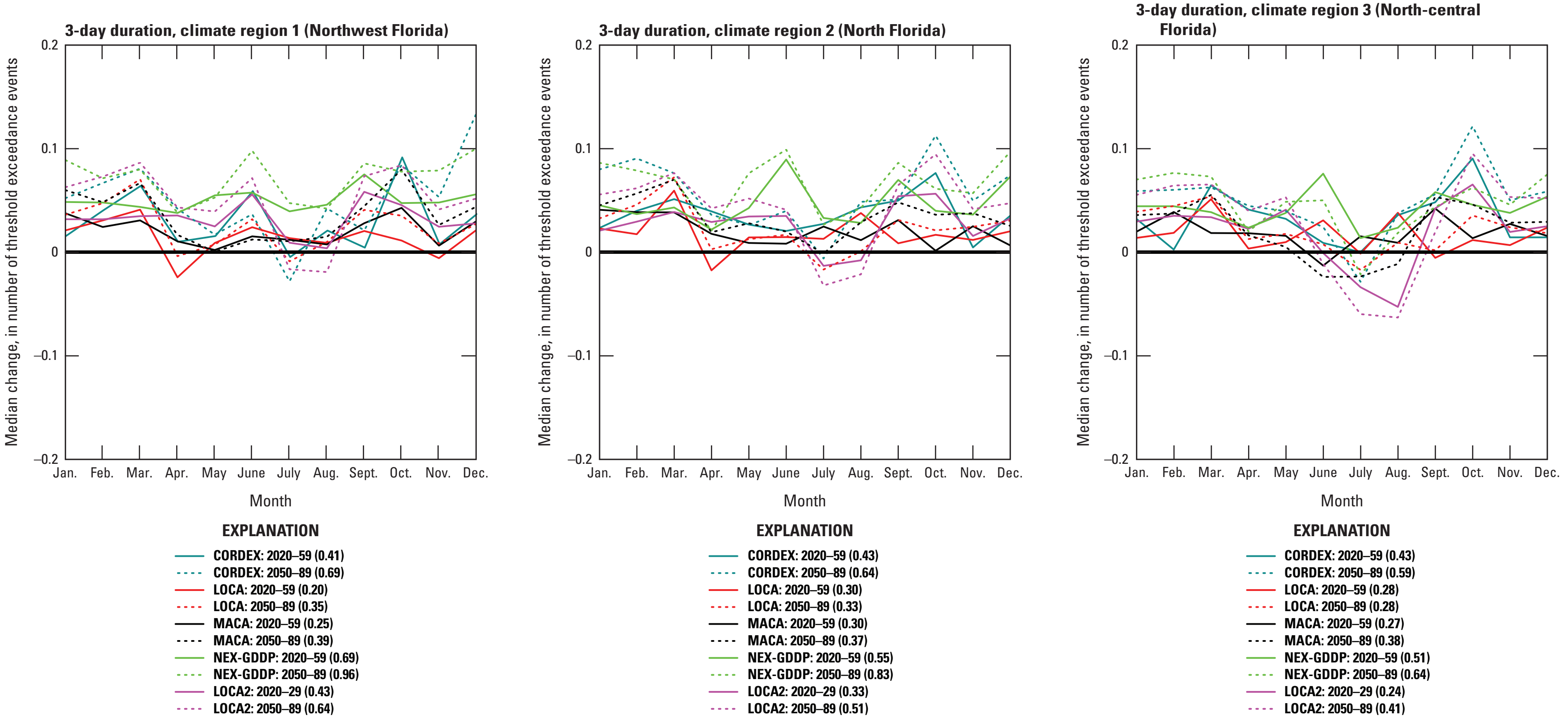

**Figure 14.** Median change in the mean annual cycle of the monthly number of declustered threshold exceedance events from the historical period (1966–2005) to the two future periods (2020–59 and 2050–89) for 3-day duration, as simulated in each downscaled climate dataset for the Florida climate regions in figure 2. Values in parentheses next to each dataset represent the median change in the annual number of declustered threshold exceedance events from the historical period to the future period. CORDEX, Coordinated Regional Downscaling Experiment; LOCA, Localized Constructed Analogs; LOCA2, Localized Constructed Analogs version 2; MACA, Multivariate Adaptive Constructed Analogs); NEX-GDDP, National Aeronautics and Space Administration Earth Exchange Global Daily Downscaled Projections.

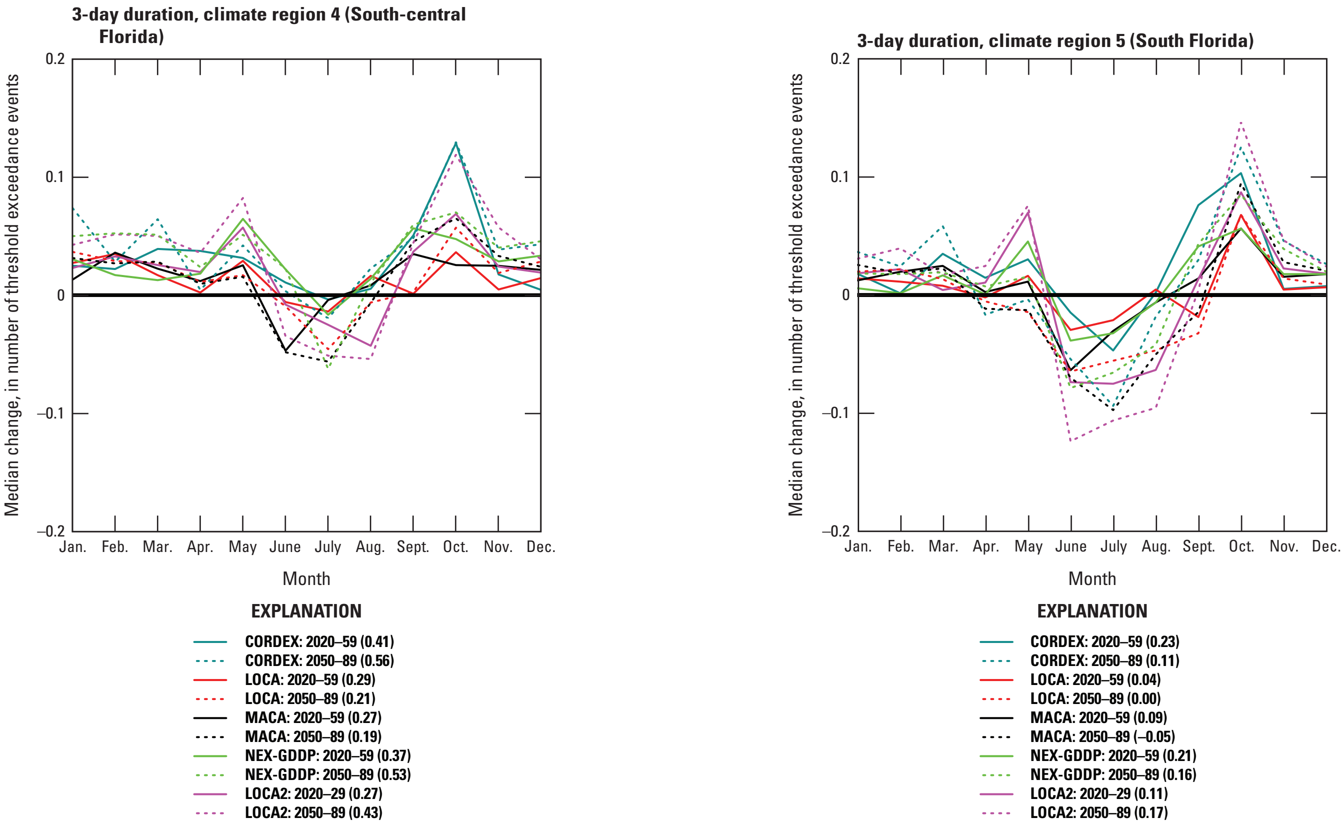

**Figure 14.**—Continued

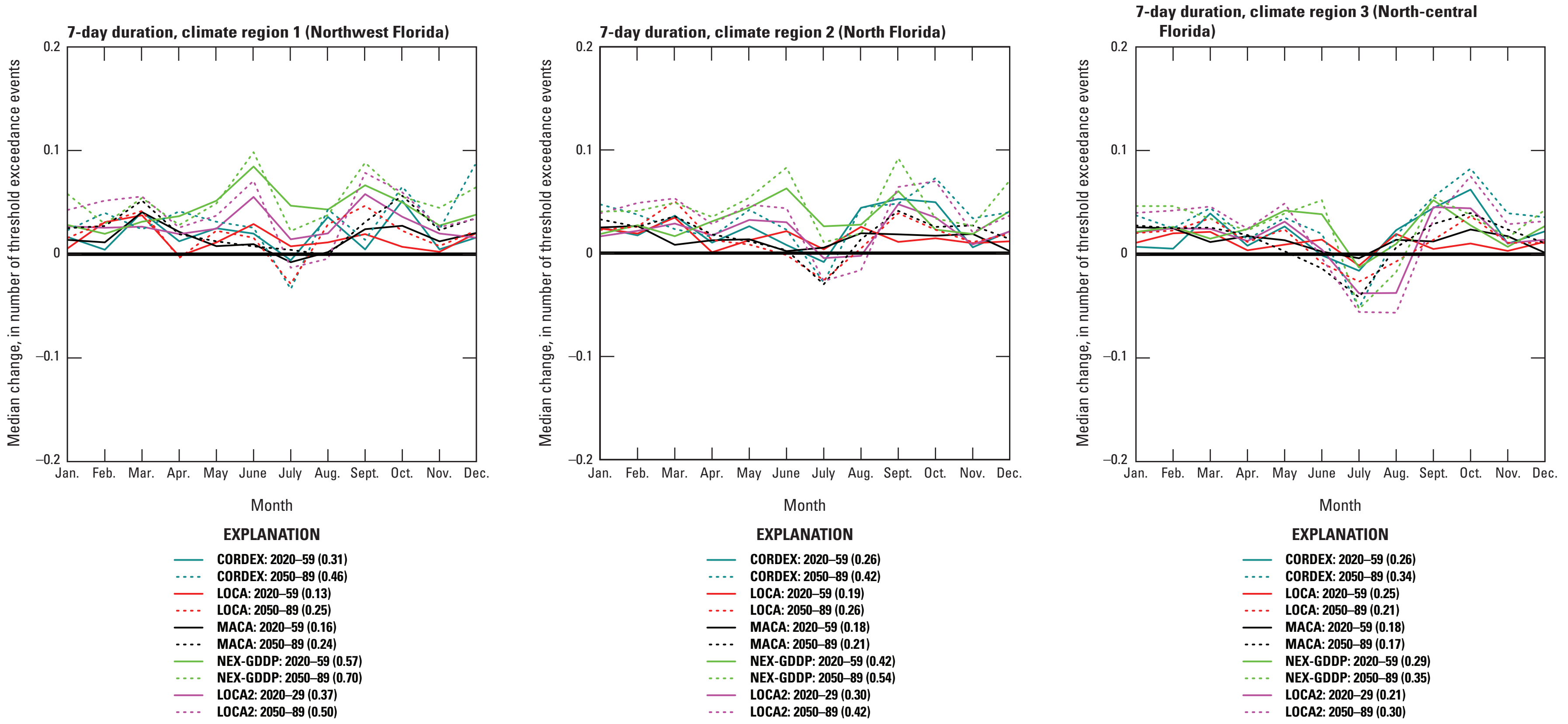

**Figure 15.** Median change in the mean annual cycle of the monthly number of declustered threshold exceedance events from the historical period (1966–2005) to the two future periods (2020–59 and 2050–89) for 7-day duration, as simulated in each downscaled climate dataset for the Florida climate regions in figure 2. Values in parentheses next to each dataset represent the median change in the annual number of declustered threshold exceedance events from the historical period to the future period. CORDEX, Coordinated Regional Downscaling Experiment; LOCA, Localized Constructed Analogs; LOCA2, Localized Constructed Analogs version 2; MACA, Multivariate Adaptive Constructed Analogs); NEX-GDDP, National Aeronautics and Space Administration Earth Exchange Global Daily Downscaled Projections.

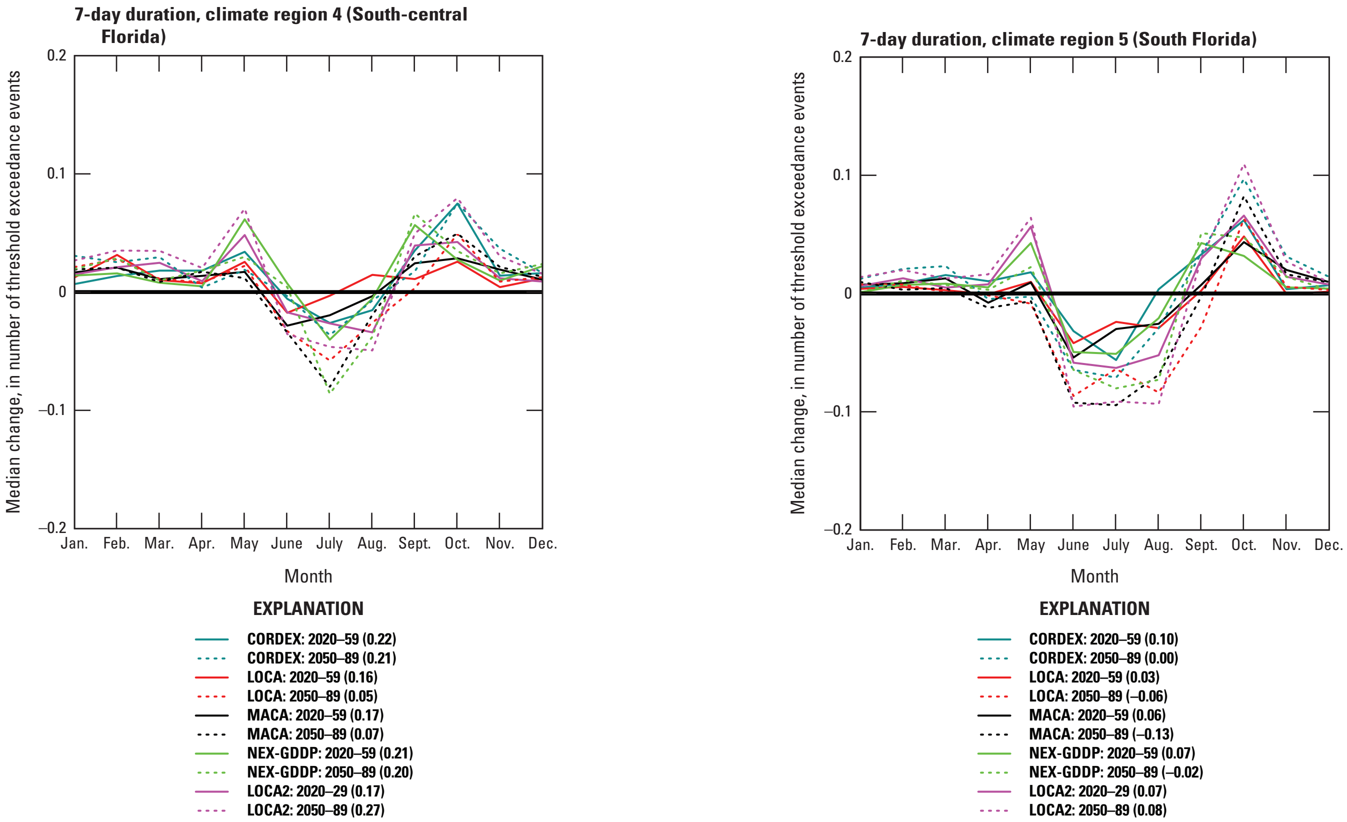

**Figure 15.**—Continued

calculated with respect to the traditional maximum likelihood (ML) model. It was found that more than 95 percent of grid cells have $\Delta AIC$ values below 2 and 7, which according to Burnham and Anderson (2002) and Burnham and others (2011), respectively, indicates that there is substantial evidence and support for the (simpler) CML model compared to the traditional ML model. A relatively small percentage of cells (< 0.2 percent) exceeds the $\Delta AIC$ threshold of 7 units.

The figure 16 bar graphs indicate the percentage of model grid cells with p-values less than 0.05 for the lag-1 KACF and the MK trend test on excess values in the historical (1966–2005) and future projection (2020–59 and 2050–89) periods. The null hypothesis that precipitation-excess data are not autocorrelated is measured by the KACF, whereas the null hypothesis that it does not exhibit monotonic trends is quantified by the MK test. The nominal rate line in figure 16 represents the expected percentage of rejections of the null hypothesis when it is true, which is the significance level or expected nominal value of 5 percent. Also shown in this figure is the 95-percent prediction interval for the significance level under multiple comparison testing and under the assumptions that the data are uncorrelated and that the number of false rejections of the null hypotheses follows a binomial distribution, as in Serinaldi and Kilsby (2014). The percentage of rejections of the null hypothesis of no autocorrelation and no trend are close to the nominal value for most periods and durations. The main exception is CORDEX for which the null hypothesis is rejected more often than the nominal rate for MK tests in the historical period and the future period 2050–89. Another exception is MACA for which the null hypothesis rejection rate is slightly larger than the nominal rate for the 3- and 7-day MK tests in the historical period, and for the 1- and 3-day MK tests in the future period 2050–89. The 1- and 7-day MK tests for LOCA in the future period 2050–89 also have rejection rates slightly larger than the nominal rate. The 7-day KACF test for MACA and the 1- and 7-day KACF tests for the NEX-GDDP in the historical period also indicate a rejection rate slightly larger than expected. The maximum rejection rate obtained for the MK tests is 7 percent, which is comparable to the 7- to 8-percent rejection rates corresponding to the 98th percentile-based threshold chosen by Serinaldi and Kilsby (2014) in fitting the GP to rainfall observations for the period 1970–2011. On the basis of these results, we conclude that it is acceptable to use a stationary approach in fitting the GP for these two 40-year periods.

Figure 17 shows bar graphs indicating the percentage of model grid cells for which the null hypothesis that the historical (1966–2005) and the future projected (2020–59 and 2050–89) precipitation-excess data follow a GP distribution is rejected at the 0.05 significance level for each duration in each downscaled climate dataset. The p-values are bootstrapped on the basis of the CML assumption, as discussed in appendix 3 of Irizarry-Ortiz and others (2022). Results are only shown for the model grid cells closest to the 242 NOAA Atlas 14 stations used in this study. The figure shows a nominal rate of 5 percent and a 95-percent prediction interval for the significance level. Overall, CORDEX tends to perform worse for the 1-day duration compared to the other datasets, especially in the future periods, with rejection rates much higher than the nominal rate of 5 percent expected by chance if all data follow a GP distribution. For the 1-day duration, only MACA and NEX-GDDP in the historical period consistently show rejection rates below or close to 5 percent across all GOF tests. LOCA tends to perform worse than the other datasets for 3- and 7-day durations, with higher rejection rates than the chosen nominal rate of 5 percent. Limited GOF testing based on the traditional ML approach with bootstrapping indicates a similar percentage of rejections, indicating that the performance deterioration when using CML does not have a large influence on the high test rejection rates for the GOF statistics and that, in fact, the raw excess data do not always seem to follow a GP distribution.

Figures 18 and 19 show L-moment ratio diagrams for precipitation excesses in the historical (1966–2005) and future projection (2020–59 and 2050–89) periods for CMIP5 and CMIP6 downscaled climate datasets, respectively. JupiterWRF is only included in the 1-day panel in figure 18 because 3- and 7-day durations were not evaluated for this dataset. The empirical L-moment ratios for all datasets shown in figure 18 tend to follow the GP line shown in the figure. As the duration increases, the cloud of points shifts slightly from the portion of the GP curve to the upper right of the exponential ("EXP") point, which corresponds to positive shape parameters, to the portion of the GP curve to the lower left of the exponential point, which corresponds to negative shape parameters. This shift reflects a general decline in shape parameters with increasing duration. In figure 18, some LOCA points show lower L-skew and L-kurtosis, especially for the 1-day duration, indicating a tendency for lower GP shape parameters and lower extremes in all periods. There is also a slight tendency for higher L-kurtosis in the future projection periods than in the historical period, indicating a tendency for higher GP shape parameters and higher extremes in the future. A portion of the cloud of points to the left of the exponential point tends to be located somewhat below the GP curve.

The cloud of points for NEX-GDDP (fig. 19) is much more compact around lower L-skew and L-kurtosis values than for the other datasets, which implies lower shape parameter values. This finding indicates that this dataset has smaller extreme precipitation values than the other datasets and, as will be shown, underestimates extreme precipitation. The lower extreme precipitation in NEX-GDDP might be the combined result of the use of GMFD for training and bias correction and the BCSD downscaling method, which is much simpler than analog-based methods used in LOCA and MACA. For example, Avila-Diaz and others (2020) found that GMFD substantially underestimates daily and multiday extremes in Brazil compared to other datasets of similar spatial resolution. The BCSD method combines the observed historical daily spatial climatology of precipitation with relative changes at each timestep simulated by a GCM. Therefore, interannual variability in extremes mainly reflects

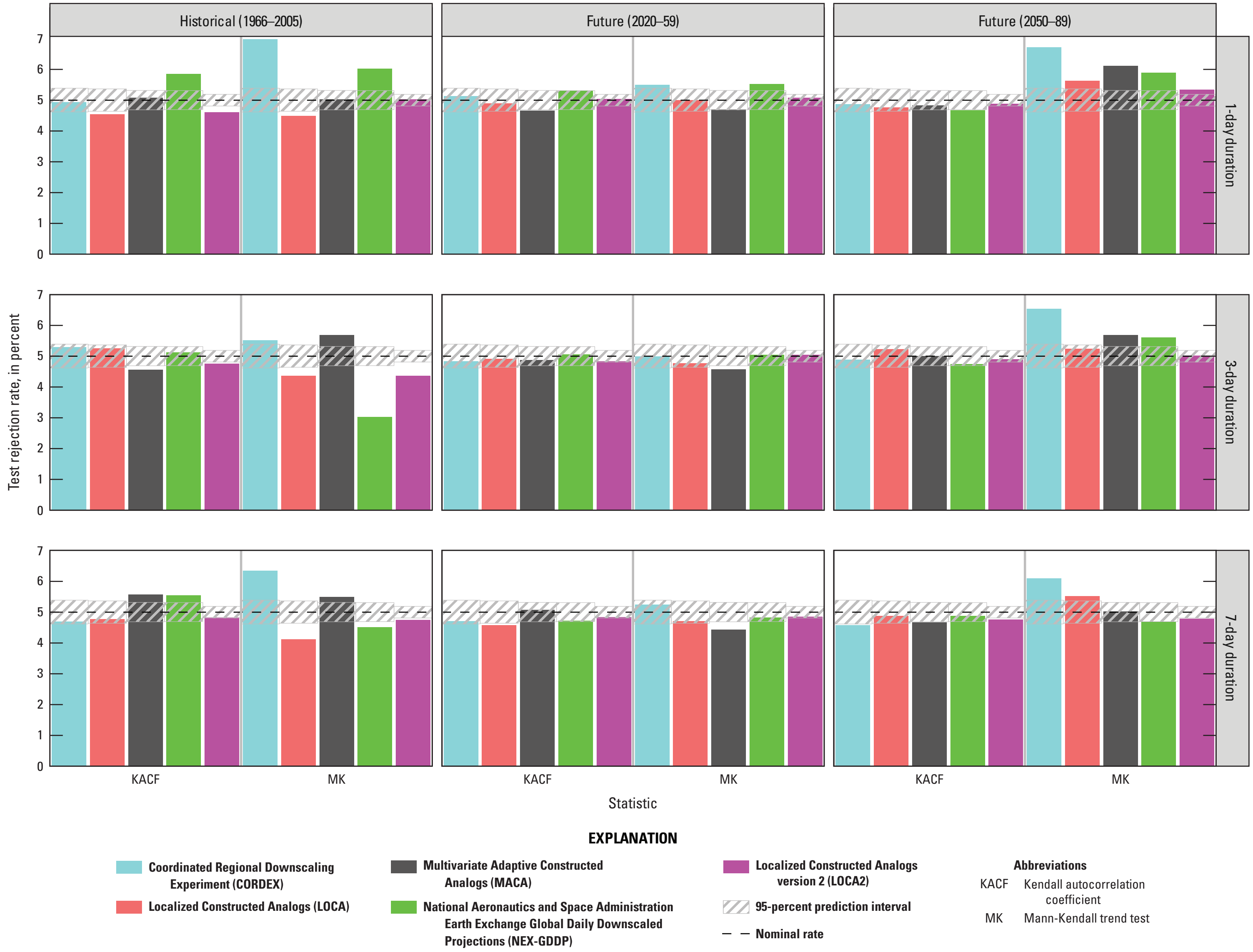

**Figure 16.** Percentage of model grid cells with a p-value less than 0.05 for peaks-over-threshold (POT) statistics in the historical period (1966–2005) and future projection periods (2020–59 and 2050–89) by downscaled climate dataset for durations of 1, 3, and 7 days.

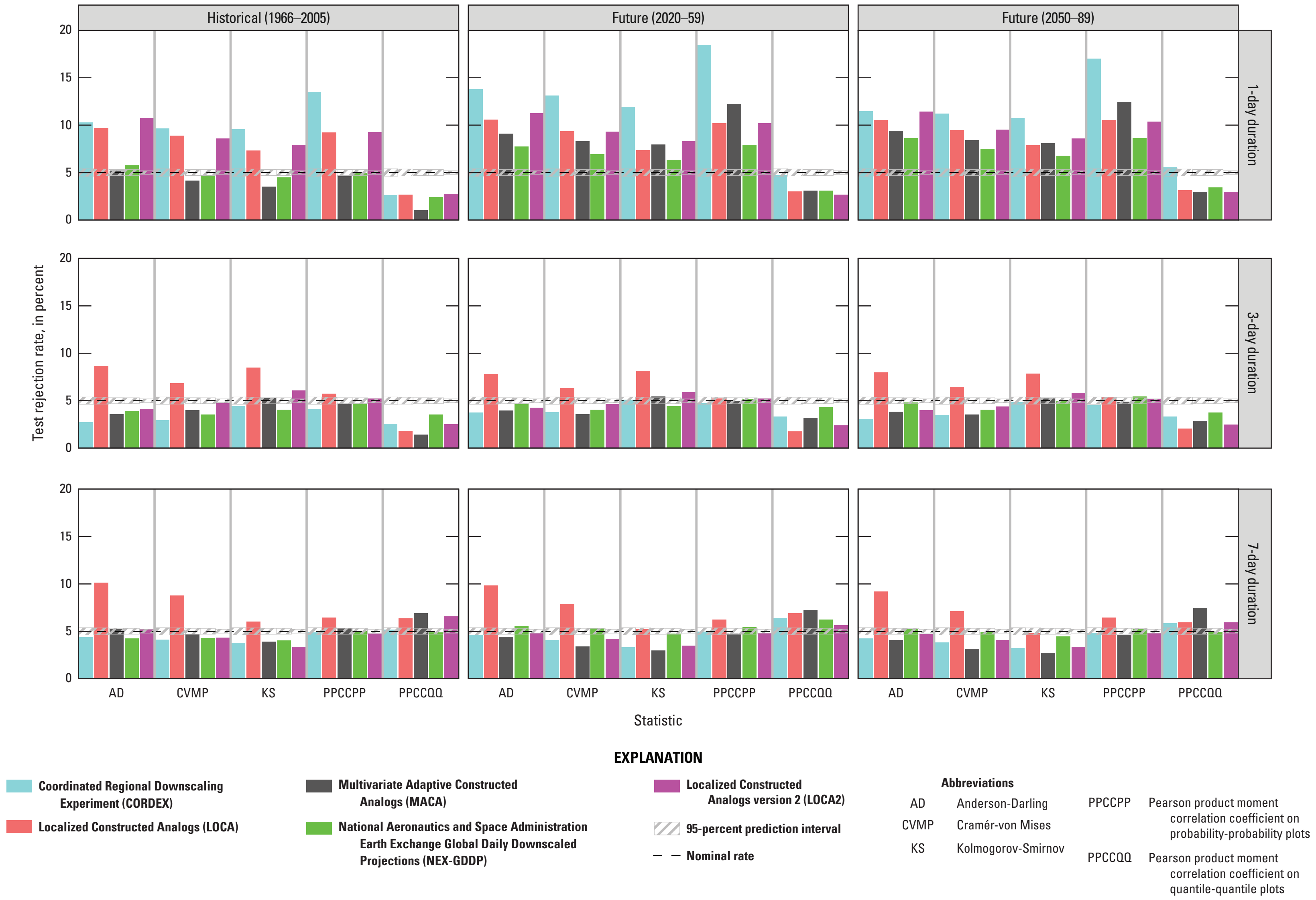

**Figure 17.** Percentage of model grid cells with p-value less than 0.05 for goodness-of-fit (GOF) statistics in the historical period (1966–2005) and future projection periods (2020–59 and 2050–89) by downscaled climate dataset for durations of 1, 3, and 7 days.

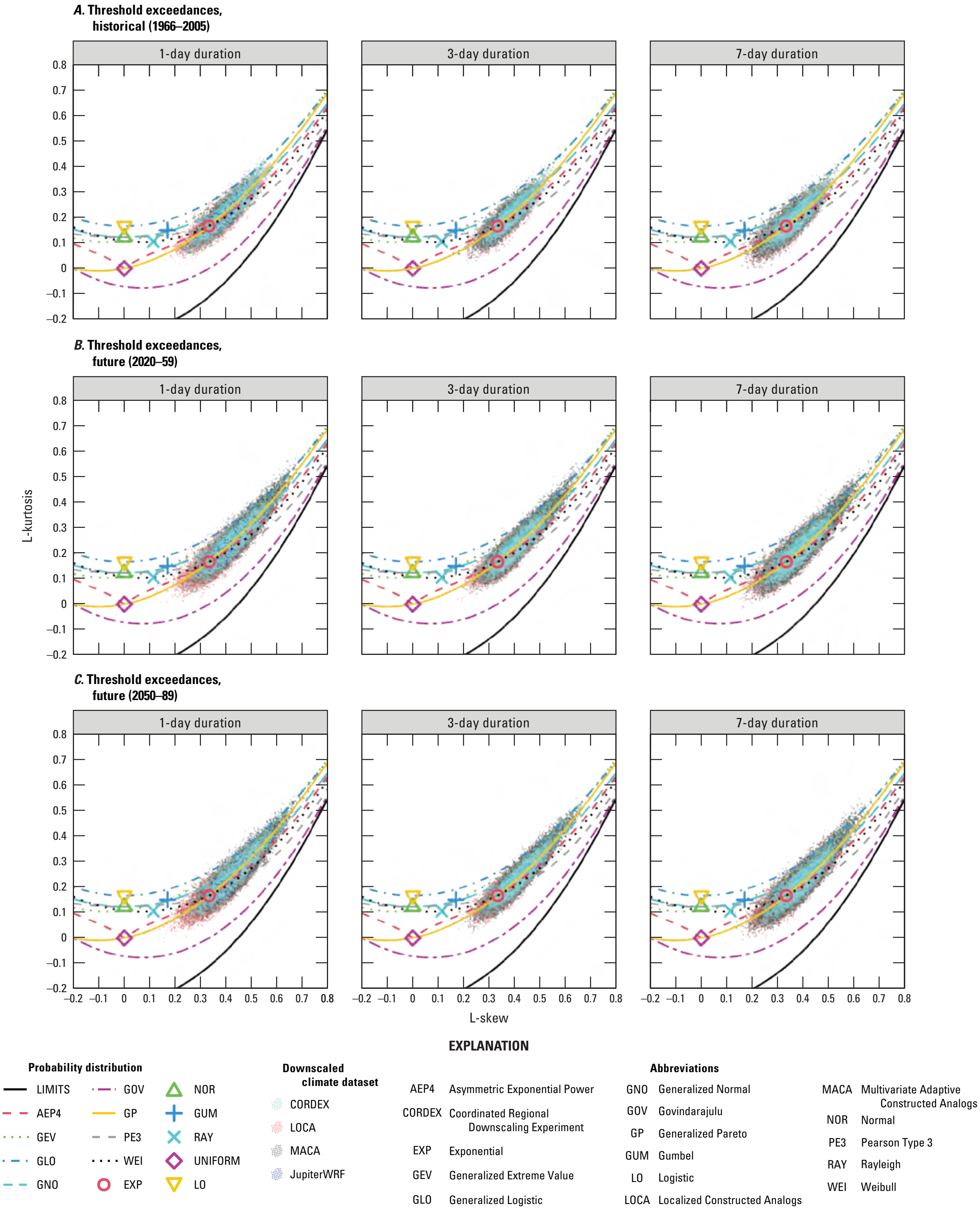

**Figure 18.** L-moment ratio diagrams for threshold exceedances in, *A*, the historical period (1966–2005), *B*, the future projection period 2020–59, and, *C*, the future projection period 2050–89 for Coupled Model Intercomparison Project Phase 5 (CMIP5) downscaled climate datasets. The large points correspond to probability distributions with no shape parameter and the curves correspond to probability distributions with a shape parameter.

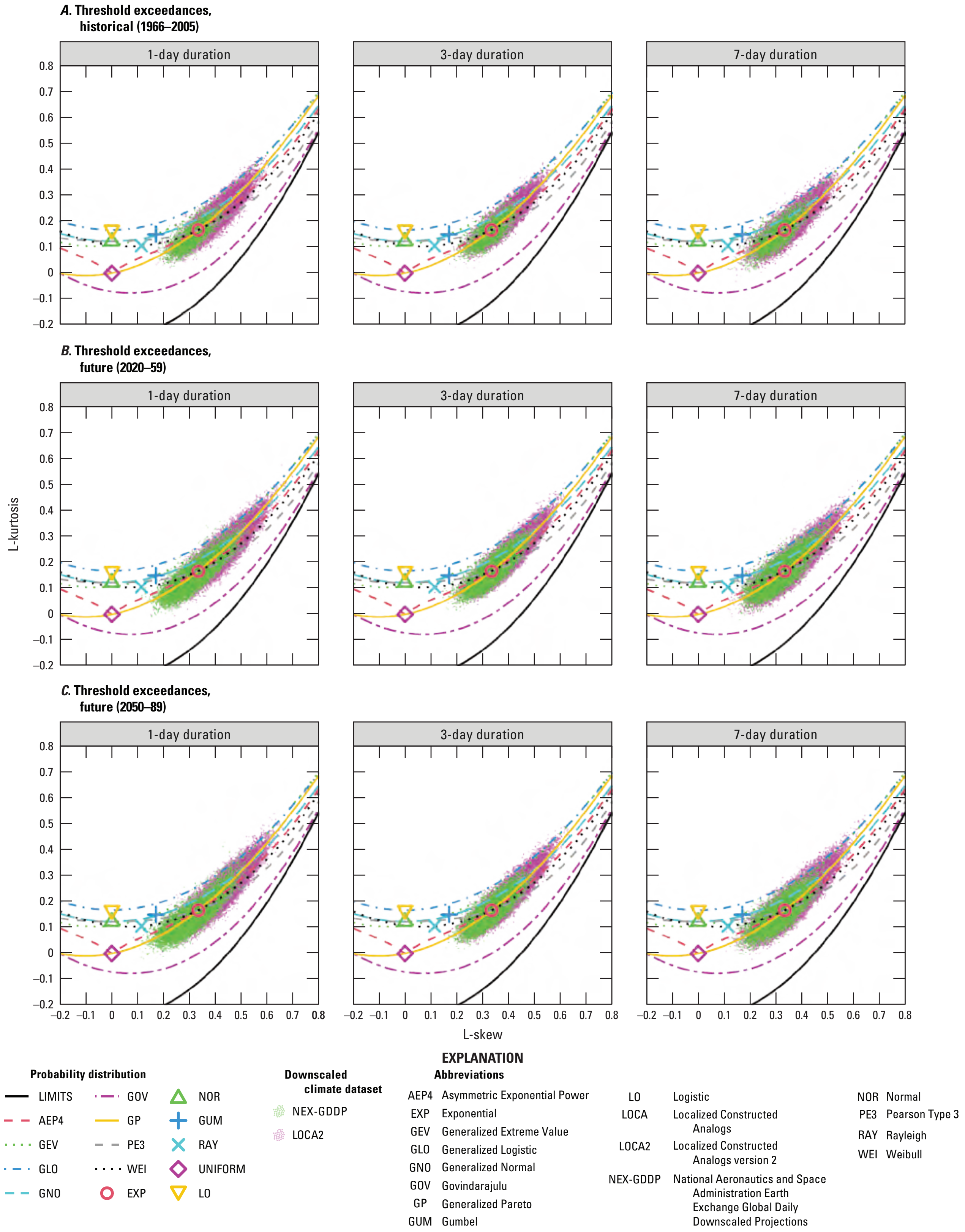

**Figure 19.** L-moment ratio diagrams for threshold exceedances in, *A*, the historical period (1966–2005), *B*, the future projection period 2020–59, and, *C*, the future projection period 2050–89 for Coupled Model Intercomparison Project Phase 6 (CMIP6) downscaled climate datasets. The large points correspond to probability distributions with no shape parameter and the curves correspond to probability distributions with a shape parameter.

that of the GCM as opposed to originating from analogue historical days as in other methods, which may also limit the variability in extremes.

Figures 18 and 19 also show more points farther to the upper right of the GP curve in the future projection periods compared to the historical period, reflecting an overall tendency for larger shape parameters and larger extremes in the future.

The bar charts in figure 20 show the percentage of model grid cells for which a given probability distribution is one of the five best fitting probability distributions among the tested distributions according to the AIC, which include all the available functions for positive real numbers in the gamlss R package. The selection of the best fitting probability distributions was performed using the fitDist function in gamlss, which uses the AIC to balance GOF with distribution parsimony. In this figure, the first four bars (EXP, PARETO2, PARETO2o, and GP) correspond to different parameterizations of the GP and the exponential distribution, which is the special case of the GP having a shape parameter of zero. The bars for the remaining distributions are ordered from higher to lower percentage. The GP is an adequate distribution for most locations, durations, periods, and datasets; however, various parameterizations of the Weibull distribution are also among the best fitting distributions. The GP with an exponent different from zero (that is, PARETO2, PARETO2o, and GP in fig. 20) appears to be less adequate for NEX-GDDP, whereas the GP with an exponent of zero (EXP in fig. 20) and the various parameterizations of the Weibull distribution appear to be more adequate. This reflects the lower L-skew and L-kurtosis values for NEX-GDDP shown in figure 19.

Using global precipitation data, Serinaldi and Kilsby (2014) show that nonzero precipitation (that is, equivalent to a POT approach with a threshold of zero) tends to follow a Weibull distribution, and they reference studies showing a progressive shift from GP to Weibull as the threshold is decreased. This finding indicates it is possible that the selected constant percentile-based threshold for each duration may be too low at some locations (that is, the asymptotic conditions for the GP are not being met), resulting in more rejections of the null hypothesis of a GP distribution than the expected nominal value of 5 percent (significance level). Figures 18 and 19 show, however, that the empirical L-moment ratios are generally in better alignment with the GP curve than with the Weibull curve. In fact, the deviation of the cloud of points from the GP curve in the region below the exponential point is away from the Weibull distribution rather than toward it. Therefore, the GP distribution has more support than the Weibull distribution. Although the generalized Gamma and generalized Beta Type 2 distributions have more parameters, they are not among the best fitting distributions according to the AIC (fig. 20). In other words, the improvement in fit is not sufficient to justify the higher number of parameters in these distributions.

## Historical Bias and Spatial Pattern

The overall percentage difference of the model-derived station-scale DDF depths for the entire historical period available in the downscaled climate datasets (1950–2005) were analyzed relative to the partial-duration series (PDS)-based DDF depths from NOAA Atlas 14 volume 9 (Perica and others, 2013). The percentage differences (fig. 21) are calculated from the mean DDF depths at all 242 NOAA Atlas 14 stations in Florida, except for JupiterWRF where the difference is only based on the 171 stations in central and south Florida included on its grid (fig. 3*G*). The DDF depths from NOAA Atlas 14 volume 9 are based on statistical fits to precipitation observations within the period 1840–2008, depending on the station. Although different methods and periods of record are used in DDF fitting for the downscaled climate datasets compared to NOAA Atlas 14 volume 9, it is still informative to evaluate their overall differences. From figure 21, it is evident that the JupiterWRF dataset has the lowest absolute difference from observed DDF depths for the 1-day duration, on the order of less than 10 percent, followed by CORDEX-Daymet with median differences of about −12 to −21 percent, and CORDEX-gridMET with median differences of about −21 to −25 percent. LOCA and MACA-gridMET perform poorer than most datasets for the 1-day duration, with median differences in the range of −33 to −36 percent. The poor daily performance for LOCA might be a result (at least in part) of deficiencies in its training dataset (Livneh and others, 2015) mentioned earlier in this report. LOCA2, which uses Livneh unsplit for training, has lower negative biases than LOCA, especially for the 1-day duration (about −20 percent). NEX-GDDP performs poorer than all the other datasets and underestimates extremes, with median 1-day differences ranging from −61 to −75 percent. This underestimation of extremes is evident in the L-moment diagrams (figs. 18–19), where NEX-GDDP has lower L-skew and L-kurtosis than the other datasets.

Although the MACA-Livneh dataset uses the Livneh and others (2013) dataset for training, it did not show differences as large as those for LOCA, with differences in the range of −26 to −28 percent for the 1-day duration (fig. 21), indicating that the differences in LOCA may also be due to the downscaling method used. Two different versions of the Livneh dataset (Livneh and others, 2013, 2015) and two different periods are used in bias correcting LOCA and MACA, which may also explain some of the differences. MACA-gridMET has median 1-day differences of about −33 to −35 percent, close to those of LOCA, but larger negative differences than in MACA-Livneh. MACA-gridMET models always show negative differences, whereas some MACA-Livneh models show positive differences for the 7-day duration.

Overall, the longer return periods show more negative differences (with the exception of CORDEX and JupiterWRF for the 1-day duration) and the differences are more variable across models than for the shorter return periods (fig. 21).

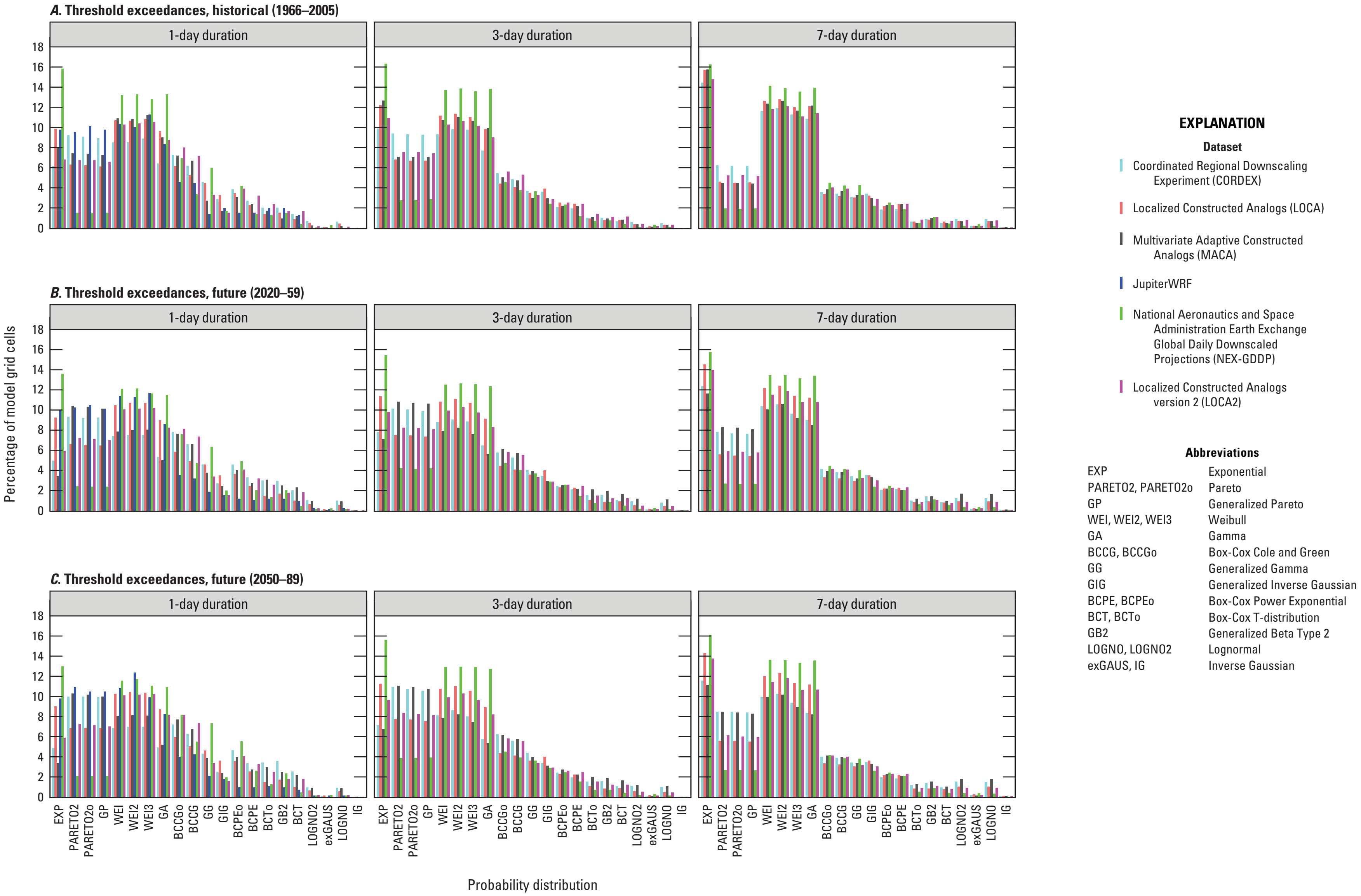

**Figure 20.** Best fitting distributions to threshold exceedances by duration and downscaled climate dataset from options available in the gamlss R package for, *A*, the historical period (1966–2005), *B*, the future projection period 2020–59 and, *C*, the future projection period 2050–89. Distribution names that end with a number are different parameterizations of the distribution. For more details, see the gamlss R package documentation (Rigby and Stasinopoulos, 2005).

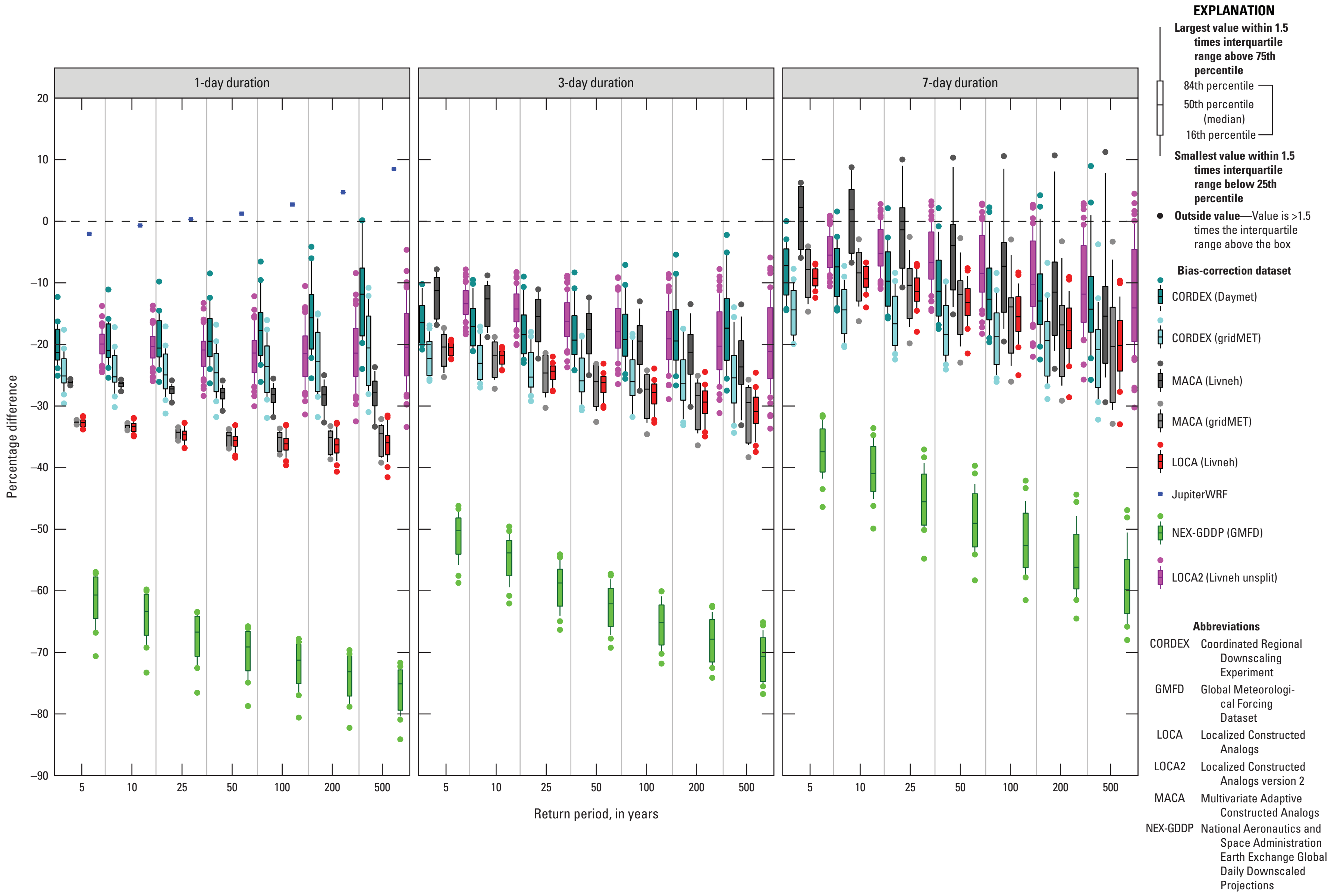

**Figure 21.** Boxplots showing the overall percentage difference in precipitation depths from depth-duration-frequency (DDF) curves fitted for the model historical period (1950–2005) compared to those fitted to observations at National Oceanic and Atmospheric Administration Atlas 14 stations (1840–2008) for all models in each downscaled climate dataset. Only one historical simulation is available for JupiterWRF, hence percent difference is displayed as a single point. Computed percent differences from Irizarry-Ortiz and Haider (2023).

The negative differences generally decrease with increasing duration for most datasets but remain quite large for NEX-GDDP. For the 7-day duration, some MACA-Livneh, LOCA2, and CORDEX-Daymet models even exhibit positive differences. Overall, the range of negative differences increases with increasing duration. Although CORDEX starts with the smallest 1-day negative difference with respect to observations, its percentage difference does not improve with increasing duration quite as much as those for the other datasets, indicating that the RCMs and (or) the bias-correction scheme may be inadequate in simulating multiday extreme events. Overall, the CORDEX-Daymet negative differences are smaller than in CORDEX-gridMET by 4–9 percent, depending on duration and return period.

The differences between extremes fitted to observations and those derived from the downscaled climate datasets might result from a combination of factors, some of which have been mentioned previously. These factors include the following, among others:

1. Biases in the observational datasets used in “training” (analog construction and bias correction of downscaled climate datasets).

2. The downscaling and bias-correction methods used. (For example, subtle differences in how tail adjustments are implemented in the different downscaled climate datasets influence the downscaled extremes.)

3. The observational datasets used in training and bias correction of downscaled climate datasets not capturing extremes at specific NOAA Atlas 14 stations (for example, because of the observational dataset not including the stations used in NOAA Atlas 14 or averaging or interpolating more than one station to obtain a grid-cell mean).

4. Differing methods and periods of record for DDF fitting used to derive the observational and downscaled climate models.

5. Biases arising from the parent GCMs. For example, the inability of CMIP5 GCMs to capture increases in extreme precipitation from the latter part of the 20th century to early 21st century has been observed by Wuebbles and others (2014) and Asadieh and Krakauer (2015) for the entire continental United States and North America, respectively. Another example is that because of the coarse spatial resolution, convection is parameterized in GCMs instead of solving physical equations of motion. Irizarry-Ortiz and others (2022) discuss CMIP model limitations in terms of their ability to capture the physical mechanisms resulting in extreme precipitation in the State of Florida.

6. Natural variability in the rarest extremes, which results in a lower signal-to-noise ratio, decreasing their predictability especially when estimated from short, and in this case different, periods of record.

7. Random differences in internal variability between the observations and the bias-corrected downscaled climate data that may be present even if data for the same multidecadal periods were being compared (that is, even after bias correction, observations and climate data may represent different portions of multidecadal cycles).

The percentage difference was computed between (1) station-scale precipitation depths obtained by fitting the GP distribution with CML to precipitation depths from the datasets used to bias-correct each downscaled climate dataset and (2) the PDS-based DDF depths from NOAA Atlas 14 for 1840–2008 (fig. 22). The periods of record and native resolutions for each bias-correction dataset vary by downscaled climate dataset, as described in each applicable subsection of the “Downscaled Climate Datasets” section. The precipitation data were obtained for the closest grid cell to each of the 242 NOAA Atlas 14 stations at the native resolution of each bias-correction dataset. The ARF values corresponding to these resolutions are very close to 1 with the exception of GMFD for which ARF values range from 0.89 to 0.98, depending on region and duration (fig. 6). Comparison of figure 22 with the median percentage difference in precipitation depths across models for each downscaled climate dataset in figure 21 indicates similar magnitudes and patterns of change with respect to changes in duration and often with respect to changes in return period. These similarities indicate that the overall percentage difference of the model-derived station-scale DDF depths for the historical period (1950–2005) compared to the PDS-based DDF depths from NOAA Atlas 14 volume 9 is largely a result of the bias-correction datasets not being able to capture the localized station-based DDF depths from NOAA Atlas 14. Daily biases were found to be the lowest for Livneh unsplit (used in LOCA2), followed by Daymet (used in CORDEX), which has the highest resolution of the bias-correction datasets (1 km). Despite daily biases being the lowest for Livneh unsplit, Ensor and Robeson (2008) found that Livneh unsplit slightly mutes extremes as a result of the gridding process. Ullrich (2023) also found that Livneh unsplit and LOCA2 exhibit larger values for most quantiles near the observing stations used in their development, especially in the southeastern United States. Therefore, extreme events at Livneh unsplit grid cells where NOAA Atlas 14 stations are located but that were not used in the interpolation to develop Livneh unsplit are expected to underestimate the NOAA Atlas 14 extremes to some degree.

The improvement of Livneh unsplit at capturing daily extremes compared to the original Livneh datasets is also evident in figure 22. The GMFD dataset used in developing the NEX-GDDP downscaled climate dataset is by far the most biased, especially for the 1-day duration. The large biases in

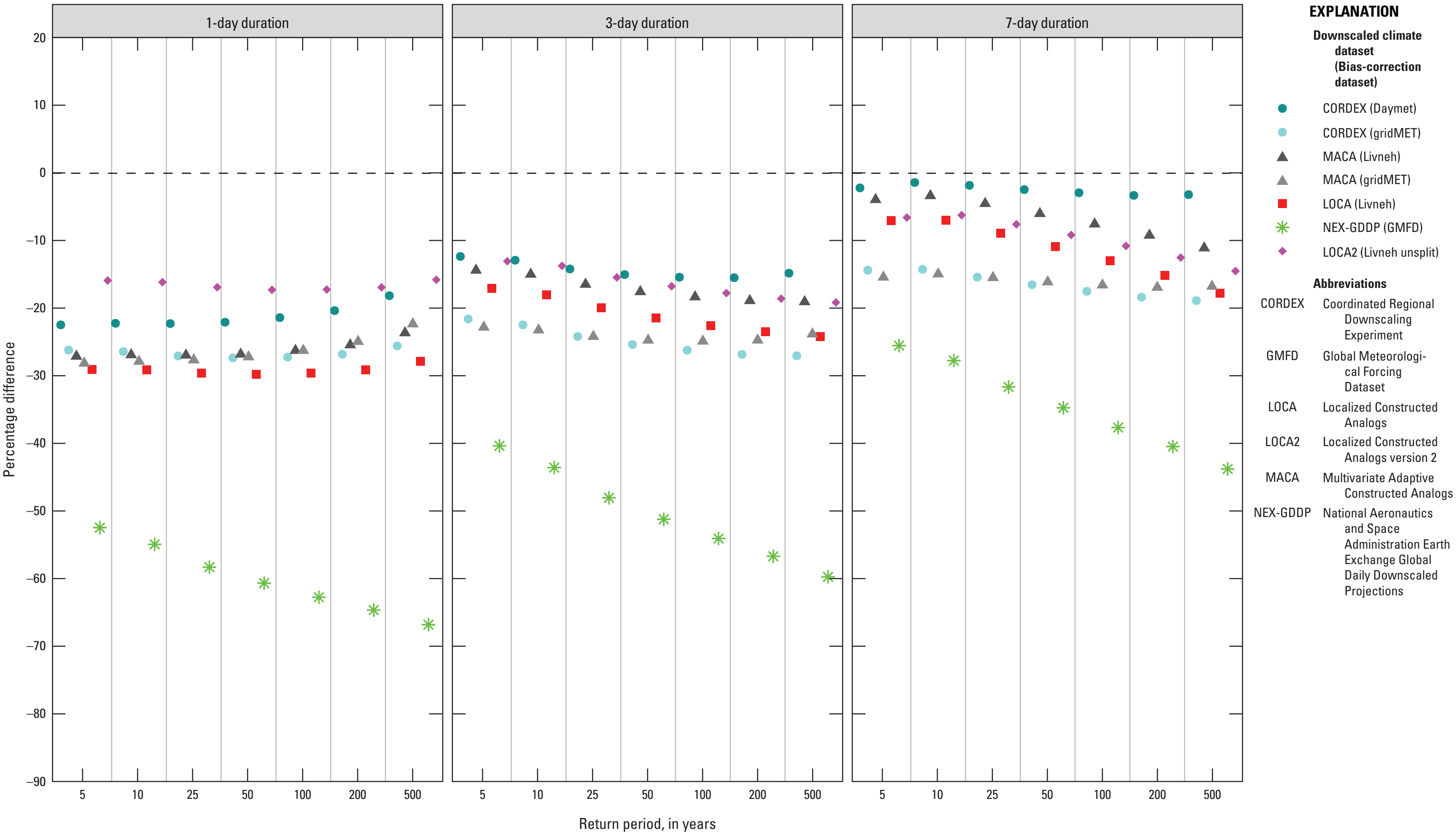

**Figure 22.** Overall percentage difference in precipitation depths from depth-duration-frequency (DDF) fitted for the bias-correction datasets used for each downscaled climate dataset compared to those fitted to observations at National Oceanic and Atmospheric Administration Atlas 14 stations (1840–2008). In the explanation, the downscaled climate dataset is listed first, followed by the bias-correction dataset in parentheses. Computed percent differences from Irizarry-Ortiz and Haider (2023).

GMFD are partially attributed to its much coarser resolution compared to the other datasets. However, Avila-Diaz and others (2020) found that GMFD substantially underestimates climate indices related to extreme precipitation, such as RX1day, RX5day, and R95p (table 3), in Brazil compared to other datasets of similar spatial resolution, such as the fifth European Centre for Medium Range Weather Forecasts Reanalysis—ERA5 (Hersbach and others, 2020). Irizarry-Ortiz and others (2022) show that differences in the periods of record and DDF-fitting methodologies only account for a small portion of the bias in the model-derived station-scale DDF depths compared to the PDS-based DDF depths from NOAA Atlas 14 volume 9.

## Model Culling

Initially, the best models were selected by evaluating the MCI and MVI criteria from Srivastava and others (2020) over the period 1981–2005 and considering all the precipitation extremes indices listed in table 3. This process resulted in a very small subset of best models. Given the desire to include as many models as possible to inform the potential range of change factors, a decision was made to only use four precipitation extremes indices in selecting best models, namely the annual maxima of precipitation for durations of 1, 3, 5, and 7 consecutive days. Irizarry-Ortiz and Haider (2023) include tables listing the best models for each climate region according to the MCI and MVI when each downscaled climate dataset (CORDEX, LOCA, MACA, LOCA2, and NEX-GDDP) is evaluated on its own for the four precipitation extremes indices chosen. Tables listing best models when all the CMIP5 datasets are evaluated together are also included in Irizarry-Ortiz and Haider (2023). In this case, the median RMSE and IVSS are defined on the basis of all the models in all the downscaled climate datasets. A model was considered to be among the best if it had a negative MCI and a negative MVI when compared to either the PRISM or SFWMD “Super-grid” observational datasets. Because of the small sample size, all models were considered the best models for the JupiterWRF dataset. As in Irizarry-Ortiz and others (2022), few LOCA models were considered best when all CMIP5 downscaled climate datasets were evaluated together. The CMIP6 datasets were not compared against each other because only models from LOCA2 would have been considered best on the basis of the poor performance of NEX-GDDP, as discussed below.

The median RMSE of the climatology of extreme precipitation indices across the different models in each downscaled climate dataset evaluated against PRISM (fig. 23) indicates that the CMIP6 NEX-GDDP performs poorer than the remaining datasets for the great majority of the indices (11–13 out of 15, depending on the climate region). Some exceptions are cumulative dry days (CDD), annual total wet day precipitation (PRCPTOT), simple daily intensity index (SDII), and annual count of days with precipitation greater than or equal to 1 mm (R1mm) for the northernmost climate regions for which NEX-GDDP performs similar to the other datasets. The poorer performance found for NEX-GDDP is consistent with findings by Avila-Diaz and others (2020) over Brazil where GMFD, the training and bias-correction dataset used in NEX-GDDP, was found to substantially underestimate extreme precipitation. The improvement from LOCA to LOCA2 caused by the switch from the Livneh and others (2015) to the Livneh unsplit (Pierce and others, 2021) dataset is also evident in figure 23. In general, the climatological performance of the datasets worsens toward the south for cumulative dry days (CDD), number of heavy precipitation days (R10mm), and PRCPTOT as quantified by the median RMSE. In contrast, the performance for the SDII improves toward the south. The performance for the maximum 1-day and multiday precipitation-depth indices (RX1day, RX3day, RX5day, and RX7day), as well as for the annual total precipitation from very wet and extremely wet days in inches and percentage (R95p, R95pTOT, R99p, and R99pTOT), is best for the north, north-central, and south-central Florida climate regions. Figure 24 shows the median IVSS across models in each downscaled climate dataset evaluated against the PRISM observational dataset. The poorer performance of NEX-GDDP in terms of IVSS is evident for the RX1day, RX3day, RX5day, and RX7day indices and in the southernmost climate regions, consistent with previous findings of low interannual variability in extremes for this dataset (fig. 19).

In this report, only results considering all models are presented; however, the list of best models and results, such as change factor quantiles at individual stations only considering best models, are included in the data release associated with this report (Irizarry-Ortiz and Haider, 2023).

## Change Factors

Change factors for DDF precipitation depths for the periods 2020–59 and 2050–89 with respect to the period 1966–2005 were computed for all model grid cells associated with NOAA Atlas 14 stations in the State of Florida from all CMIP5 and CMIP6 downscaled climate datasets evaluated as part of this study. The change factor data are available in the data release associated with this report (Irizarry-Ortiz and Haider, 2023). Figures 25–26 show median change factors for all climate regions shown in figure 2, considering all models and all RCP and SSP scenarios, for the periods centered on 2040 and 2070, respectively. In these figures, the term “all datasets” refers to the median considering all CMIP5 and CMIP6 datasets. Median change factors and their range generally increase with increasing return period and are similar across durations for all climate regions in the two future periods. The increase in change factors with return period is consistent with Lopez-Cantu and others (2020), who found that at the continental scale, high-end daily extremes generally increase more than low-end extremes, as determined by evaluating various downscaled climate datasets for the period 2044–99 with respect to 1951–2005. That is, the

**Figure 23.** Median root-mean-square error (RMSE) of the climatology of extreme precipitation indices across models in each downscaled climate dataset compared against those from the Parameter-elevation Regressions on Independent Slopes Model (PRISM) for the period 1981–2005. Units for individual extreme precipitation indices are given in table 3.

**Figure 24.** Median interannual variability skill score (IVSS) for extreme precipitation indices across models in each downscaled climate dataset compared against those from the Parameter-elevation Regressions on Independent Slopes Model (PRISM) for the period 1981–2005. Units for individual extreme precipitation indices are given in table 3.

largest historical precipitation events get larger under future conditions. The exception is JupiterWRF for which 1-day change factors do not vary much with return period. The IPCC (2021b, p. 15) also states that “There will be an increasing occurrence of some extreme events unprecedented in the observational record with additional global warming, even at 1.5 °C of global warming. Projected percentage changes in frequency are higher for rarer events (high confidence).”

Median change factors across all CMIP5 and CMIP6 datasets range between 1.04 and 1.18 for the period 2020–59 and between 1.05 and 1.23 for the period 2050–89, depending on duration and return period. When considering all RCPs and SSPs (figs. 25–26), median change factors from the LOCA, LOCA2, and JupiterWRF datasets (1-day duration only) are usually the lowest, followed by those from the NEX-GDDP, CORDEX, and MACA datasets. One exception is the median change factors from CORDEX being slightly larger than those from MACA for the 5- and 10-year, 7-day event in south Florida for the period 2050–89 (fig. 26). Overall, the median change factors are found to increase from 2020–59 to 2050–89 with the exception of MACA in the south Florida climate region where they decrease slightly in the latter period, especially for the 7-day duration. It is possible that this result is tied to the reduction in precipitation projected during summer for most MACA models in this region in the latter period (fig. 9). The median change factors also do not increase much for LOCA from 2020–59 to 2050–89, especially in the south Florida climate region. As a result of the lower median change factors projected by LOCA for the two periods in the south Florida climate region, this region has the largest range of change factors, especially for the 1-day duration.

With the exception of the longer return periods for the northwest Florida climate region, NEX-GDDP results in somewhat higher median change factors than LOCA2, especially in the north and south Florida climate regions for both periods (figs. 25–26). LOCA2 generally results in very similar though slightly higher change factors than LOCA in the north-central, south-central, and south Florida climate regions, and lower median change factors in the northwest and north Florida climate regions compared to LOCA for the period 2050–89 (fig. 26). The differences between LOCA and LOCA2 median change factors are even smaller for the earlier period 2020–59, with the exception of the north-central Florida climate region where the differences are slightly larger than in the latter period (fig. 25).

Median change factors were computed for all datasets, climate regions, and models, but only considering RCP4.5 and RCP8.5 and SSP2-4.5 and SSP5-8.5, which correspond to medium-low and high emission levels and are more directly comparable (figs. 27–28). As mentioned previously, although each RCP and its corresponding SSP attain about the same radiative forcing in the year 2100, the emissions pathways may differ. Comparison of figures 25 and 26 with 27 and 28 indicates slightly higher median change factors when only the medium-low and high emissions scenarios are considered. Median change factors considering all CMIP5 and CMIP6 datasets but only the medium-low and high emissions scenarios range between 1.05 and 1.21 for the period 2020–59 and between 1.06 and 1.27 for the period 2050–89.

Figures 29 and 30 show the median change factors by RCP/SSP for all datasets, climate regions, and models. Notably, the number of ensemble members downscaled by each dataset varies by RCP/SSP (table 2), which confounds the comparison of change factors across RCP/SSP in some datasets. A steep increase in median change factors with increasing return period is evident for the MACA and CORDEX datasets in the two periods. In the period 2020–59, the median change factors are generally lower in RCP8.5 than in RCP4.5 for MACA and CORDEX (with the exception of CORDEX in the south Florida climate region), whereas the opposite is generally the case for the latter period, 2050–89 (fig. 30). For MACA, this is the case even for return periods shorter than the 40-year period used in DDF fitting (5–25 years), which indicates that the higher change factors in RCP4.5 are not simply an artifact of extrapolation caused by distribution fitting for longer return periods, but that they are a feature of the bulk of the exceedance data used in DDF fitting. For the period 2050–89, the median MACA change factors in RCP8.5 are much higher than those of RCP4.5 in the northwest Florida climate region. Median change factors for RCP4.5 and RCP8.5 from CORDEX also deviate substantially for the northwest and north-central Florida climate regions in the latter period (fig. 30). CORDEX downscales 14 models under RCP4.5 and 54 under RCP8.5 (table 2); therefore, comparisons across RCPs are imbalanced for CORDEX. When the same 14 models are compared across RCPs, CORDEX generally has higher change factors under RCP8.5 than RCP4.5. LOCA has higher median change factors for RCP8.5 than RCP4.5 in the latter period (fig. 30); however, the differences between RCPs are smaller and RCP4.5 change factors are often higher than RCP8.5 change factors in the earlier period.

Median change factors from NEX-GDDP tend to stay flat or even decline with return period for most durations and SSPs in the northwest Florida climate region, especially in the earlier period, and in the northwest, north, and south-central Florida climate regions for the 1-day duration in the latter period (fig. 30). This may be related to the GMFD training and bias-correction dataset and the BCSD method used in NEX-GDDP resulting in too little interannual variability in extremes, with high historical extremes not well captured (figs. 19 and 21), an issue that may be amplified in the future projections. In the latter period, median change factors from NEX-GDDP tend to be highest under SSP2-4.5 and lowest under SSP3-7.0 in the north-central, south-central, and south Florida climate regions, especially for the 7-day duration. In the northwest and north Florida climate regions, median change factors from NEX-GDDP for the latter period (fig. 30) mostly increase or change little with increasing emissions (SSP level); however, SSP3-7.0 has the highest change

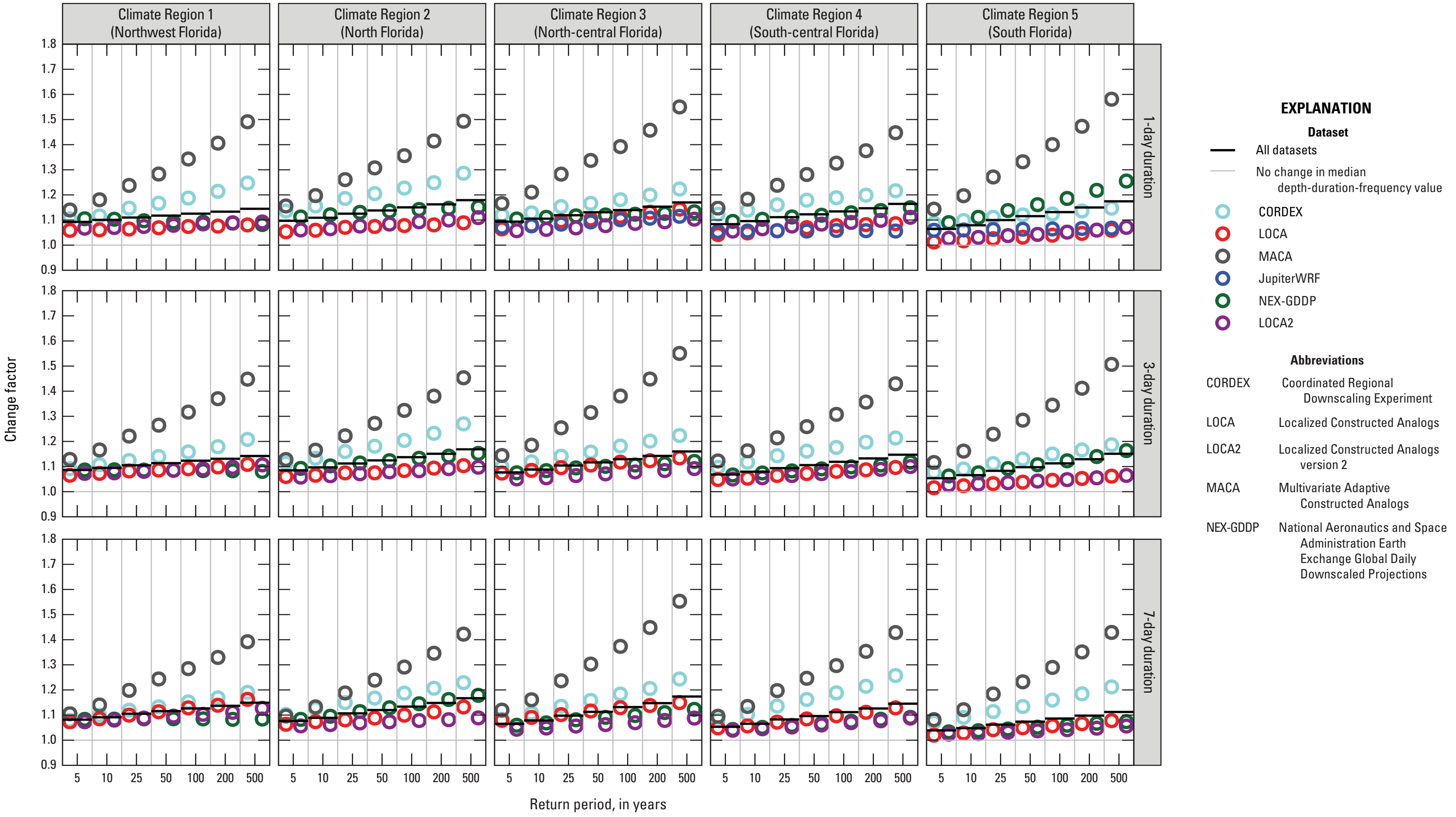

**Figure 25.** Median change factors across downscaled climate datasets for stations within each Florida climate region (fig. 2) considering all models and all representative concentration pathways and shared socioeconomic pathways for the period 2020–59. Coupled Model Intercomparison Project Phase 5 (CMIP5) datasets and Coupled Model Intercomparison Project Phase 5 (CMIP6) datasets shown in separate columns. JupiterWRF output only available for 1-day duration and for central and south Florida.

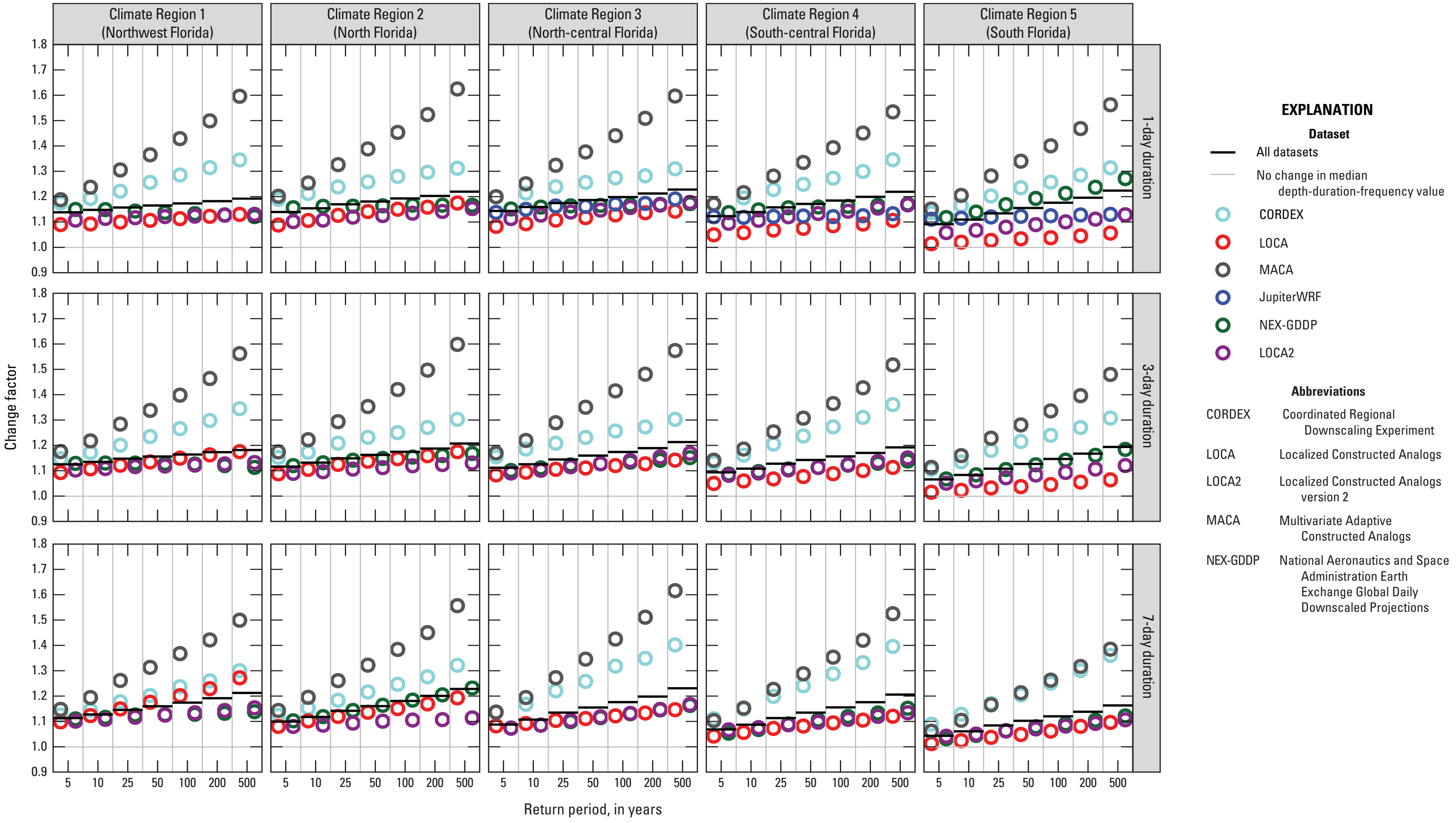

**Figure 26.** Median change factors across downscaled climate datasets for stations within each Florida climate region (fig. 2) considering all models and all representative concentration pathways and shared socioeconomic pathways for the period 2050–89. Coupled Model Intercomparison Project Phase 5 (CMIP5) datasets and Coupled Model Intercomparison Project Phase 5 (CMIP6) datasets shown in separate columns. JupiterWRF output only available for 1-day duration and for central and south Florida.

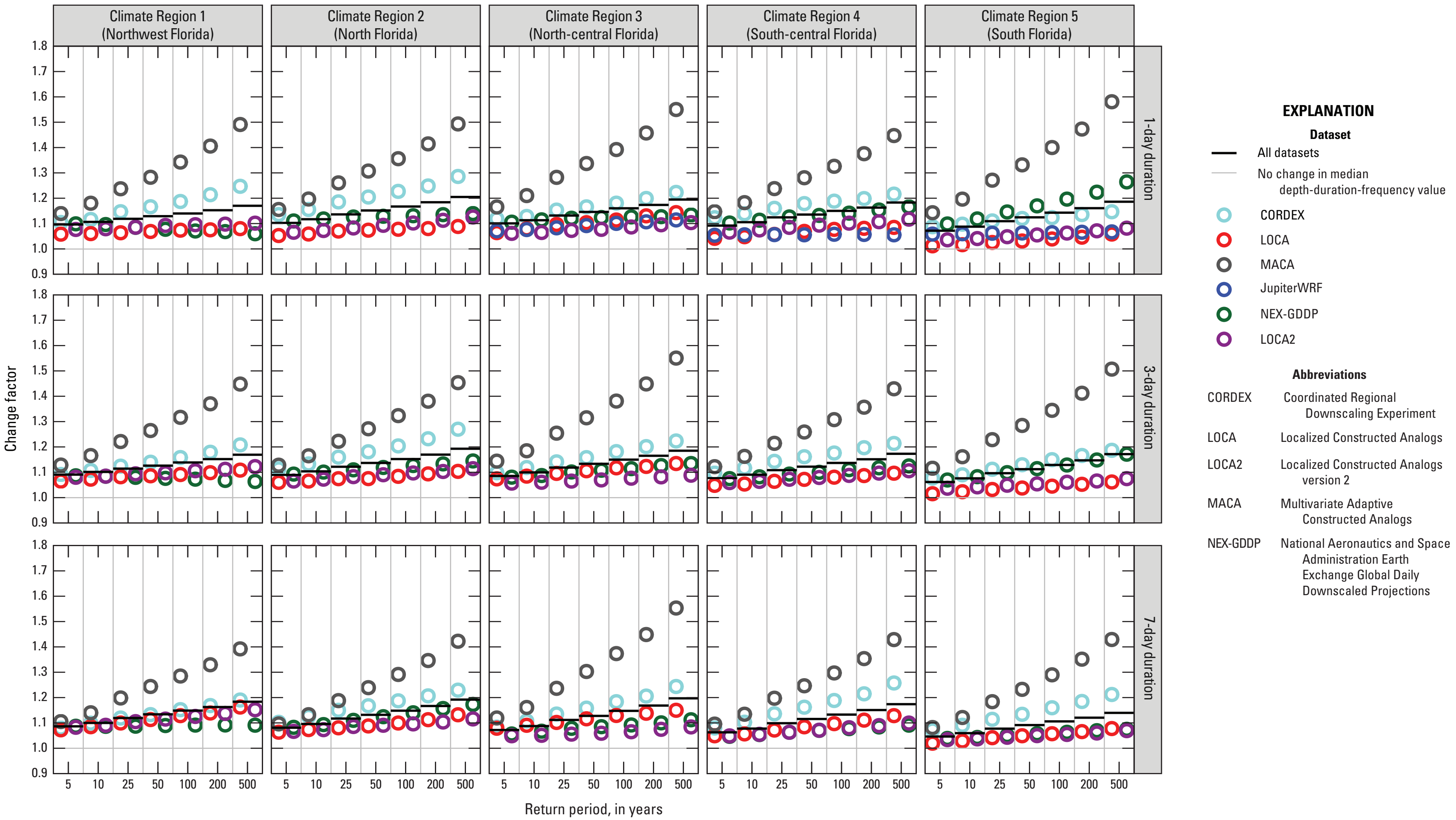

**Figure 27.** Median change factors across downscaled climate datasets for stations within each Florida climate region (fig. 2) considering all models and only representative concentration pathways RCP4.5 and RCP8.5, and shared socioeconomic pathways SSP2-4.5 and SSP5-8.5 for the period 2020–59. Coupled Model Intercomparison Project Phase 5 (CMIP5) datasets and Coupled Model Intercomparison Project Phase 6 (CMIP6) datasets shown in separate columns. JupiterWRF output only available for 1-day duration and for central and south Florida.

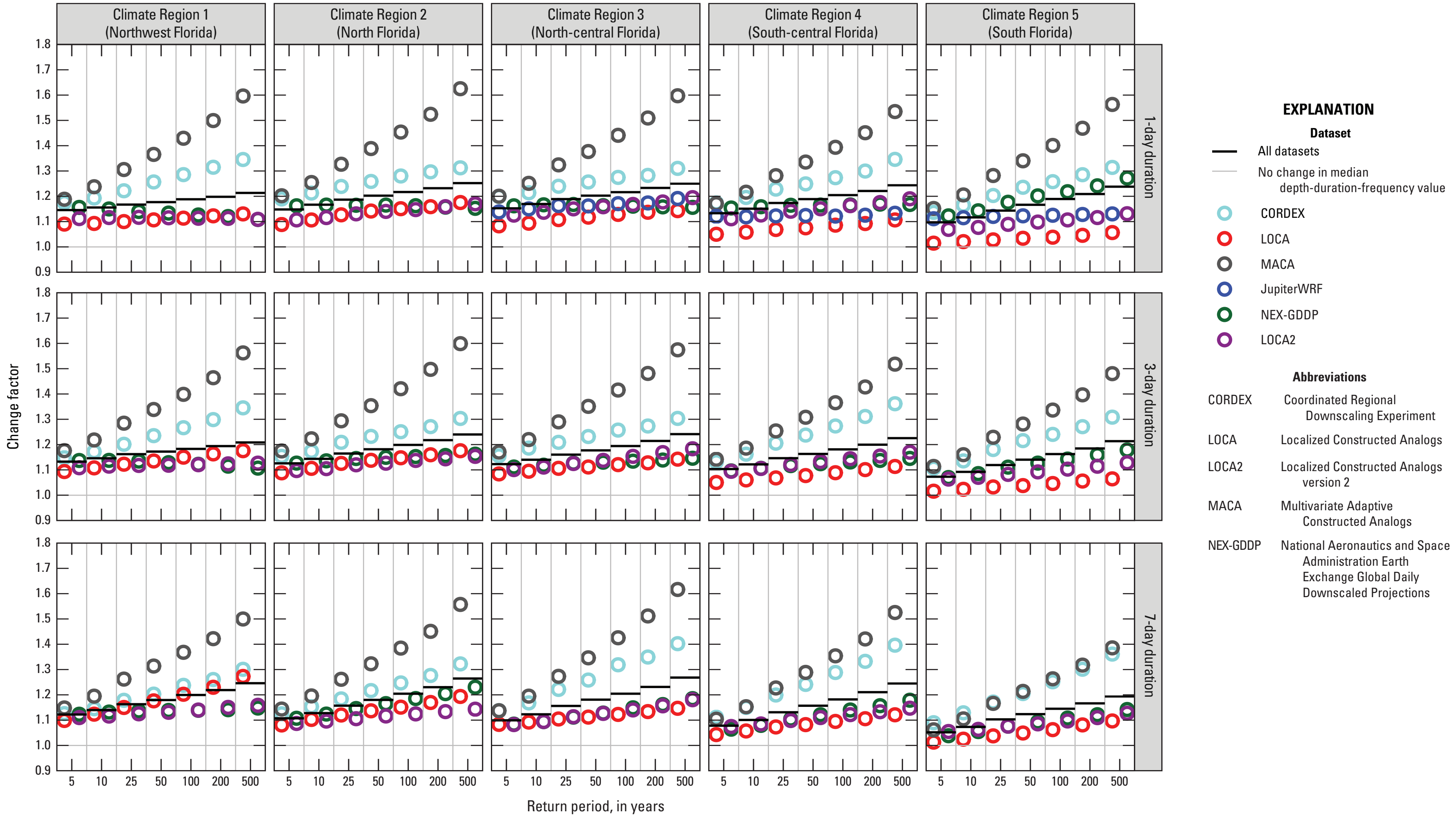

**Figure 28.** Median change factors across downscaled climate datasets for stations within each Florida climate region (fig. 2) considering all models and only representative concentration pathways RCP4.5 and RCP8.5, and shared socioeconomic pathways SSP2-4.5 and SSP5-8.5 for the period 2050–89. Coupled Model Intercomparison Project Phase 5 (CMIP5) datasets and Coupled Model Intercomparison Project Phase 6 (CMIP6) datasets shown in separate columns. JupiterWRF output only available for 1-day duration and for central and south Florida.

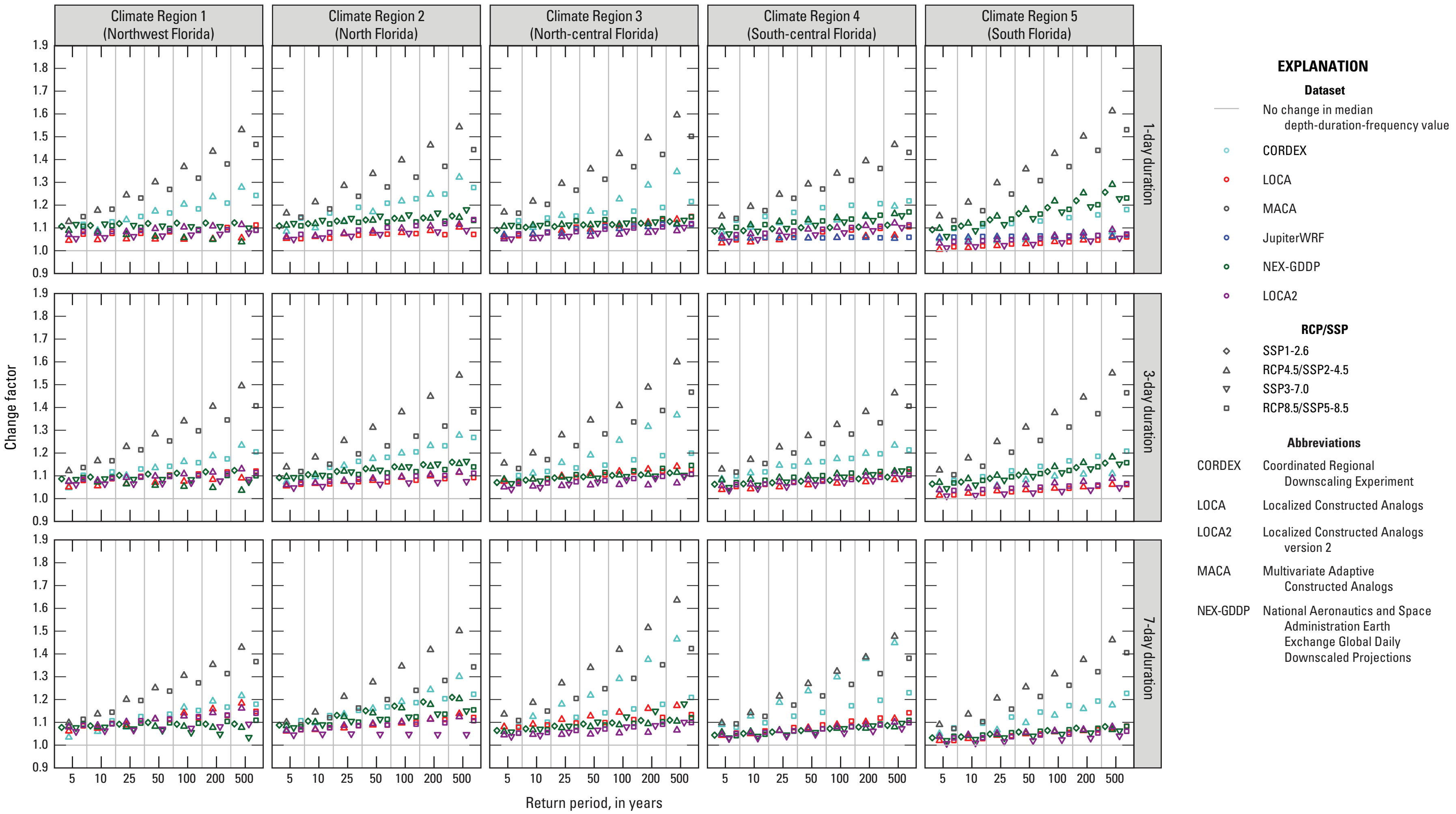

**Figure 29.** Median change factors across downscaled climate datasets for stations within each Florida climate region (fig. 2) considering all models and split by representative concentration pathway (RCP) and shared socioeconomic pathway (SSP) for the period 2020–59. Different RCP/SSP scenarios shown in separate columns.

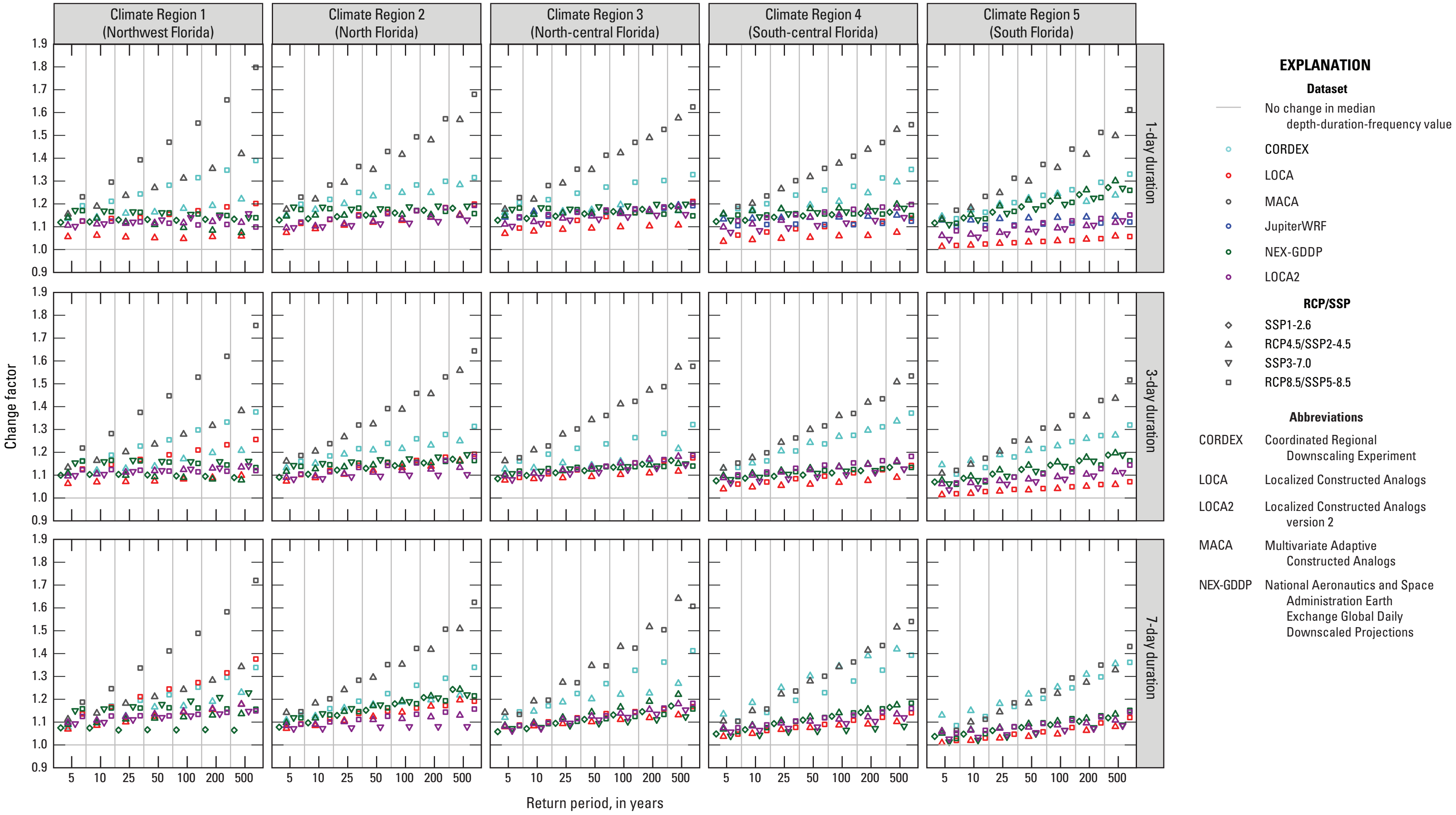

**Figure 30.** Median change factors across downscaled climate datasets for stations within each Florida climate region (fig. 2) considering all models and split by representative concentration pathway (RCP) and shared socioeconomic pathway (SSP) for the period 2050–89. Different RCP/SSP scenarios shown in separate columns.

factors for the 7-day duration in the northwest Florida climate region. NEX-GDDP downscales a smaller number of models and ensemble members under SSP3-7.0 (table 2); therefore, comparisons across SSPs are imbalanced for NEX-GDDP; however, the previously discussed variation in change factors with SSP remains very similar when only the GCM and ensemble member combinations with data available for all four SSPs downscaled by NEX-GDDP are considered.

Median change factors from LOCA2 generally increase with return period (figs. 29–30). In both periods, SSP3-7.0 generally has the lowest median change factors in LOCA2, with the exception of the north-central Florida climate region in the earlier period and the northwest Florida climate region in the latter period. The differences between SSPs are somewhat reduced when only the GCM and ensemble member combinations available for all three SSPs downscaled by the LOCA2 dataset are considered.

Figures 31–34 show maps of median change factors for the 1-day, 100-year event from each CMIP5 and CMIP6 downscaled climate dataset in the two periods of interest. In addition, maps of median change factors considering all datasets available for each CMIP version are provided. For CMIP6, maps are also provided that include only the SSP2-4.5 and SSP5-8.5 scenarios. The spatial patterns of median change factors are quite different across the different datasets. MACA clearly projects the highest change factors in both periods (figs. 31 and 33). CORDEX projects areas of higher change factors in southeast Florida, western south-central Florida, north Florida, and portions of northwest Florida in the earlier period. In the latter period, the highest median change factors projected by CORDEX are in western central Florida. Isolated stations in south Florida have median change factors less than 1 in LOCA in both periods. In the latter period, LOCA projects higher median change factors at some stations in north-central and north Florida. JupiterWRF also projects change factors smaller than 1 at isolated stations in south and central Florida. When all CMIP5 datasets are considered together, the lowest median change factors are generally concentrated in south-central and south Florida.

NEX-GDDP projects the highest median change factors in the urbanized areas of southeast Florida and near Lake Okeechobee (figs. 32 and 34). As in LOCA, isolated south Florida stations have median change factors less than 1 in LOCA2, especially in the earlier period. In the latter period, the highest median projected change factors are in central Florida. When all CMIP6 datasets are considered, there is little spatial variation in median change factors throughout the State in the earlier period and some isolated stations with higher values in central and south Florida in the latter period. These patterns do not change substantially when only SSP2-4.5 and SSP5-8.5 are considered.

For the entire continental United States, Lopez-Cantu and others (2020) found that, despite being the least biased overall compared to observed extremes, the MACA-gridMET multimember mean change factors (for the period 2044–99 with respect to 1951–2005) are also considerably larger than for the other datasets evaluated, which include Bias-Corrected Constructed Analog (BCCA) version 2, LOCA, and CORDEX without bias correction (called CORDEXnoBC hereafter). They found that BCCA version 2 results in the lowest change factors for the continental United States, followed by LOCA, low-resolution CORDEXnoBC models, high-resolution CORDEXnoBC models, and MACA-gridMET models. Furthermore, Lopez-Cantu and others (2020) found that the downscaled climate datasets somewhat preserve the pattern of the change signal in the native GCM change factors; however, the magnitude of the signal is reduced in BCCA version 2 and increased in MACA-gridMET. For the southeastern United States, using the CanESM2 GCM as an example, they found for RCP4.5 that LOCA and low-resolution CORDEXnoBC models tend to preserve the GCM change signal the best, whereas MACA-gridMET amplifies the change signal, especially for longer return periods, consistent with our findings. High-resolution CORDEXnoBC models were found to amplify the change signal more evenly across return periods. Their findings were similar for RCP8.5, but they found that LOCA tends to mute the change signal, whereas its amplification in MACA-gridMET and the high-resolution CORDEXnoBC models is slightly lower than in RCP4.5.

As in Irizarry-Ortiz and others (2022), isolated outlier change factors as high as 8–10 are estimated for individual stations, especially by MACA. When these very high change factors are multiplied by NOAA Atlas 14 DDF curves, the resulting future projected DDF values can be as high as 100 in. or more over 3- to 7-day durations and return periods beyond 100 years. These values exceed the record high precipitation accumulations recorded around the globe in the last decade, as discussed in Irizarry-Ortiz and others (2022). Some recent examples of extreme precipitation events in or near Florida include Hurricane Irma in 2017 with rainfall totals of 10–15 in. across the peninsula and a maximum of 21.7 in. within St. Lucie County (NOAA, 2017). Hurricane Dorian in 2019 produced storm-total rainfall of 22.8 in. at a location in the Bahamas (NOAA, 2020a). Hurricane Eta brought more than 14 in. of rainfall to south Florida, with a localized total of 20.7 in. for November 2020 (NOAA, 2020b). Hurricane Ian produced rainfall totals of 10–20 in. over central and eastern Florida in September 2022, causing major flooding that in some areas took months to recede. The highest rainfall associated with Hurricane Ian was about 27 in. within Grove City, Florida (NOAA, 2022b). A rapid-attribution modeling study by Reed and Wehner (2023) found that 3-day accumulated rainfall from Hurricane Ian was 18 percent higher because of climate change, which is much higher than would be expected because of the Clausius-Clapeyron relation. Close to 26 in. of rainfall was recorded over 24 hours at the Fort Lauderdale-Hollywood International Airport on April 13, 2023, with the majority of the rainfall occurring over a 6- to 12-hour period (Florida Climate Center, 2023) and causing significant flooding. The April 2023 event was associated with a warm front moving north into south Florida and was classified as a 12-hour, 1,000-year event

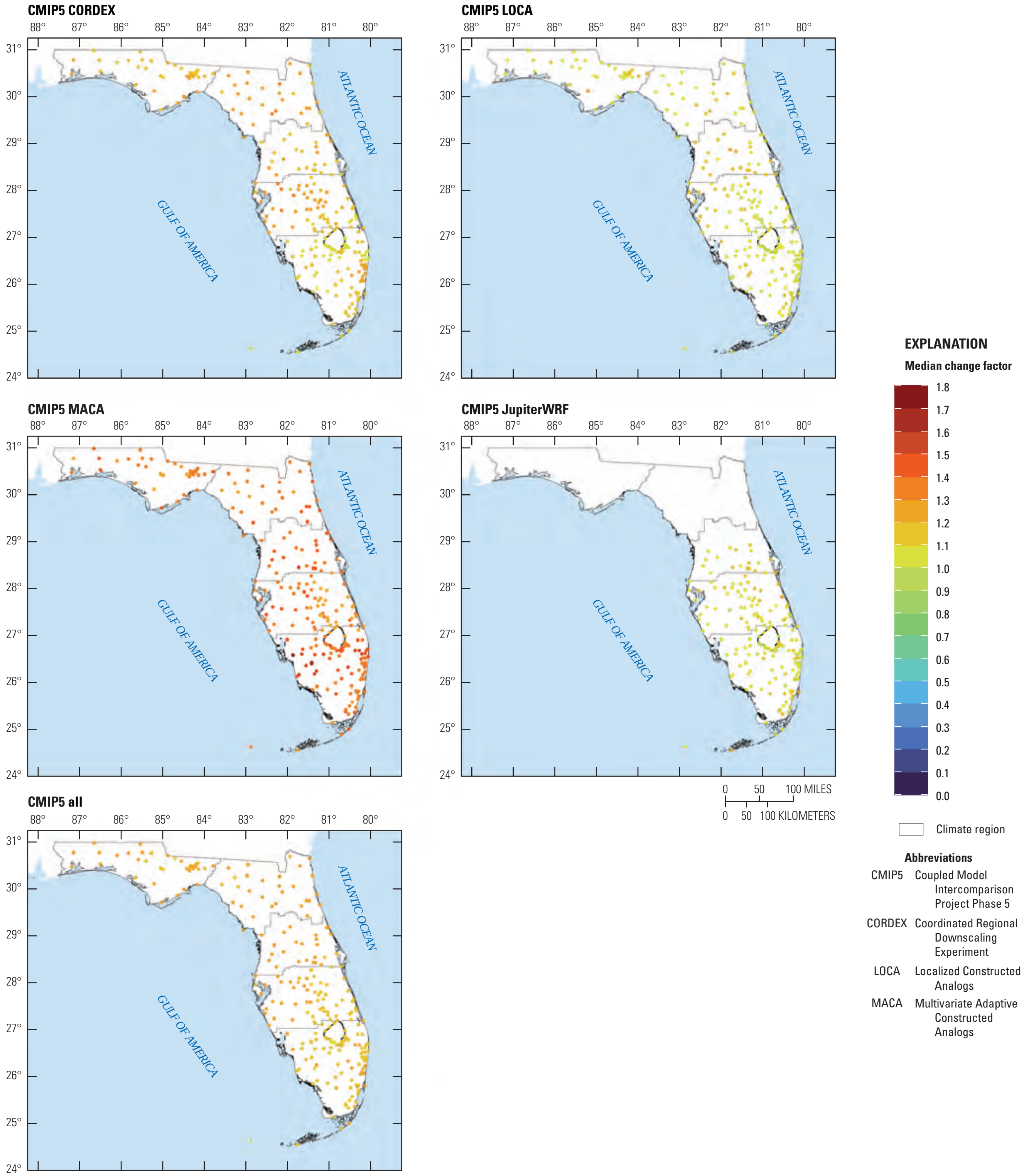

Base modified from U.S. Census Bureau Tiger database,
Florida County Boundaries, 1:100,000,1990
Geographic coordinate system
World Geodetic System 1984 datum

Climate regions from
Irizarry-Ortiz and Haider
(2023)

**Figure 31.** Median 1-day, 100-year change factors at National Oceanic and Atmospheric Administration Atlas 14 station locations across Coupled Model Intercomparison Project Phase 5 (CMIP5) downscaled climate datasets considering all models and available representative concentration pathways (RCPs) for the period 2020–59. The panel labeled “CMIP5 all” considers all models from all CMIP5 downscaled climate datasets and RCPs. The boundaries of the five climate regions shown in figure 2 are included for reference. Calculated median change factors from Irizarry-Ortiz and Haider (2023).

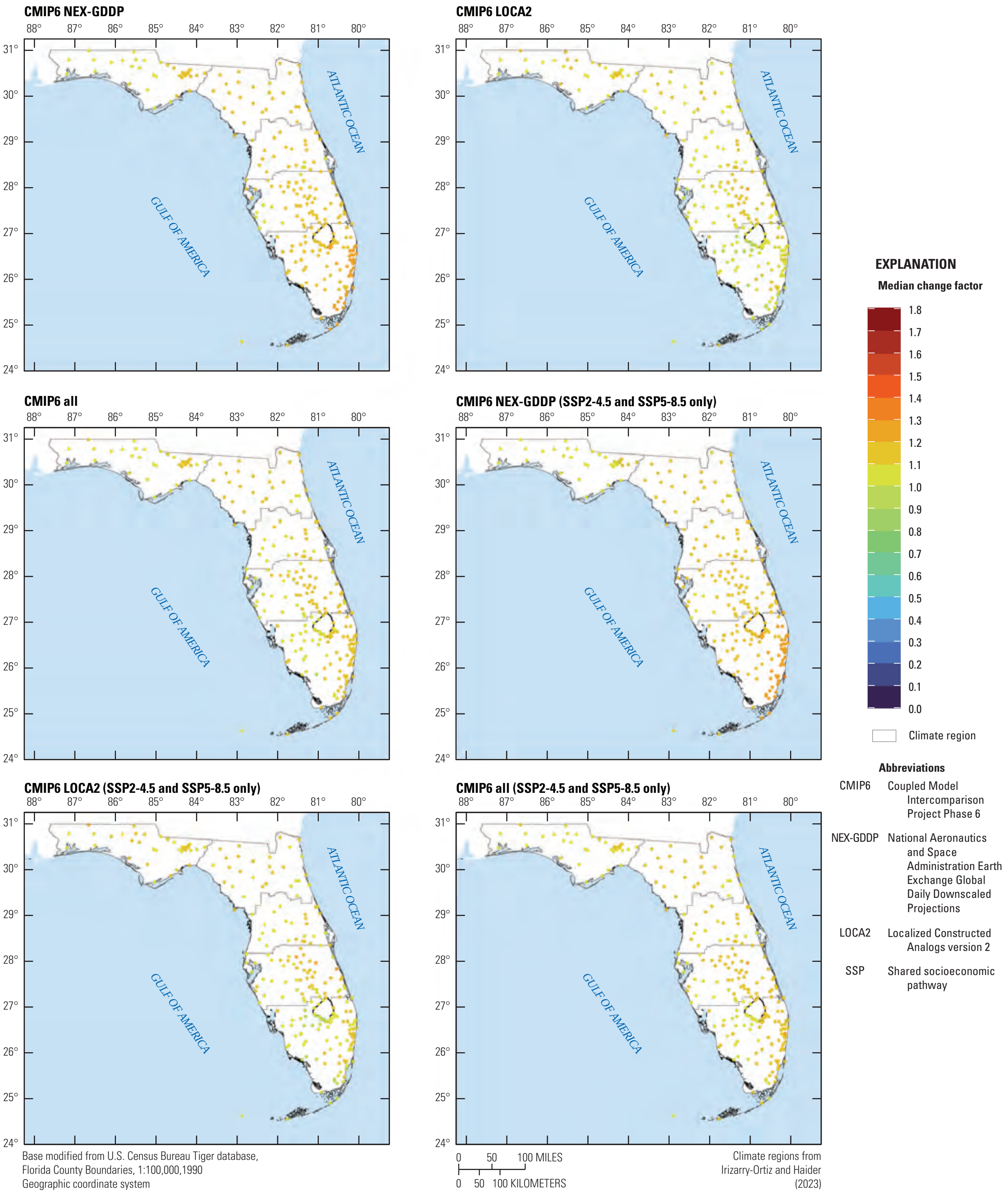

Base modified from U.S. Census Bureau Tiger database,
Florida County Boundaries, 1:100,000,1990
Geographic coordinate system
World Geodetic System 1984 datum

Climate regions from
Irizarry-Ortiz and Haider
(2023)

**Figure 32.** Median 1-day, 100-year change factors at National Oceanic and Atmospheric Administration Atlas 14 station locations across Coupled Model Intercomparison Project Phase 6 (CMIP6) downscaled climate datasets considering all models and all available shared socioeconomic pathways (SSPs) (unless otherwise indicated) for the period 2020–59. The panel labeled “CMIP6 all” considers all models from all CMIP6 downscaled climate datasets and SSPs. The panels including “(SSP2-4.5 and SSP5-8.5 only)” only consider those scenarios. The boundaries of the five climate regions shown in figure 2 are included for reference. Calculated median change factors from Irizarry-Ortiz and Haider (2023).

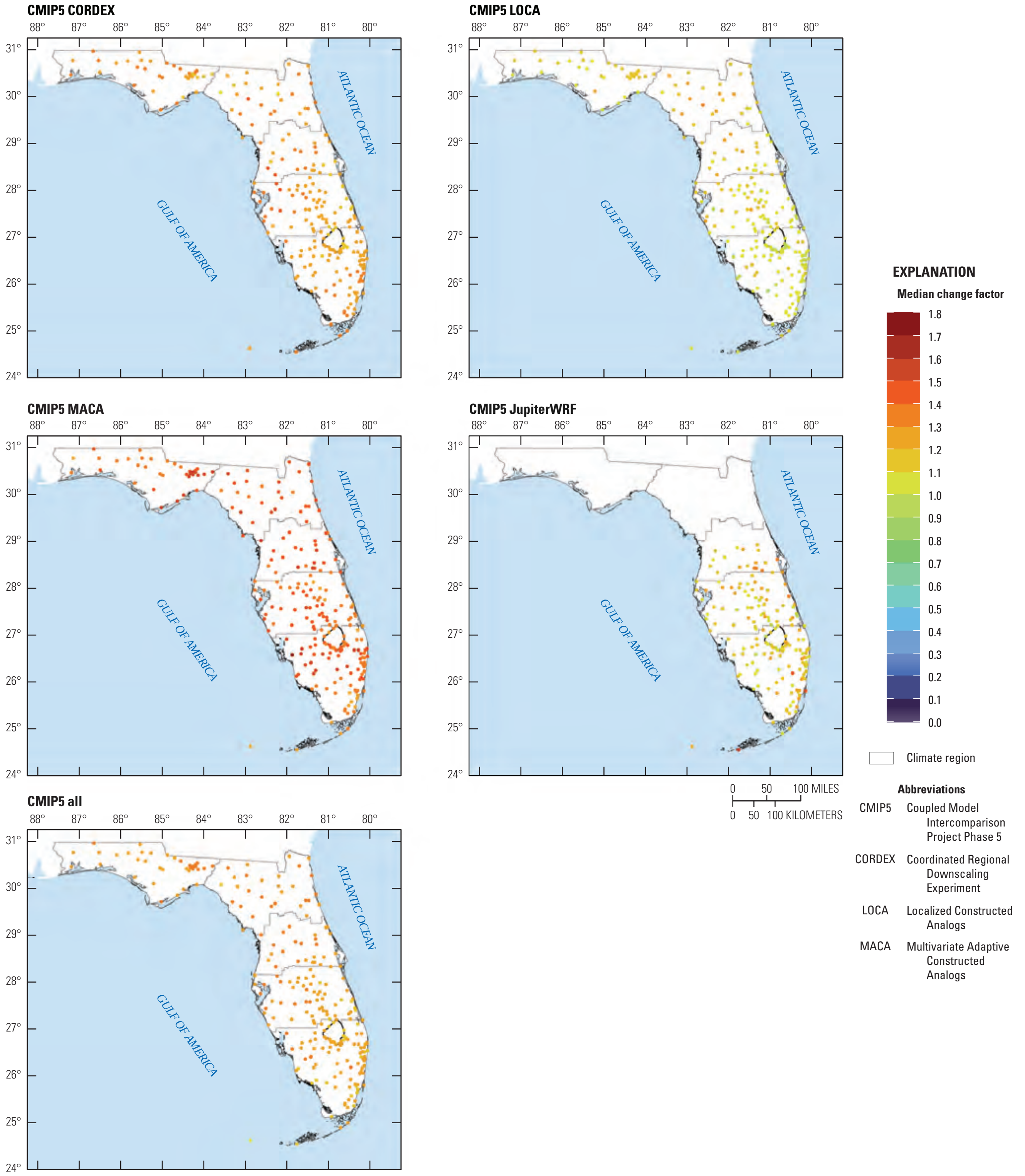

**Abbreviations**

| | |
|---|---|
| CMIP5 | Coupled Model Intercomparison Project Phase 5 |
| CORDEX | Coordinated Regional Downscaling Experiment |
| LOCA | Localized Constructed Analogs |
| MACA | Multivariate Adaptive Constructed Analogs |

Base modified from U.S. Census Bureau Tiger database,
Florida County Boundaries, 1:100,000,1990
Geographic coordinate system
World Geodetic System 1984 datum

Climate regions from
Irizarry-Ortiz and Haider
(2023)

**Figure 33.** Median 1-day, 100-year change factors at National Oceanic and Atmospheric Administration Atlas 14 station locations across Coupled Model Intercomparison Project Phase 5 (CMIP5) downscaled climate datasets considering all models and available representative concentration pathways (RCPs) for the period 2050–89. The panel labeled “CMIP5 all” considers all models from all CMIP5 downscaled climate datasets and RCPs. The boundaries of the five climate regions shown in figure 2 are included for reference. Calculated median change factors from Irizarry-Ortiz and Haider (2023).

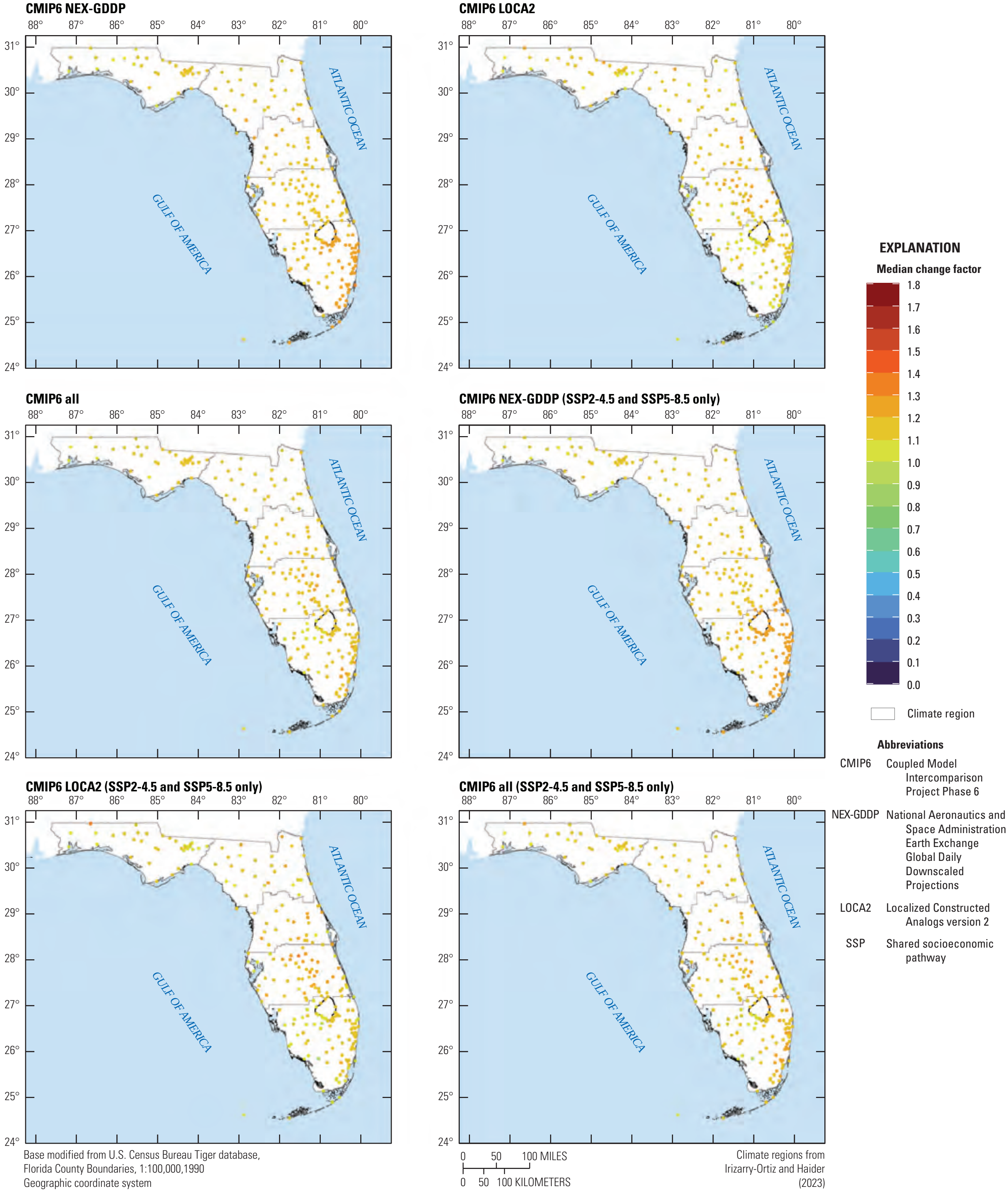
CMIP6 NEX-GDDP

CMIP6 LOCA2

CMIP6 all

CMIP6 NEX-GDDP (SSP2-4.5 and SSP5-8.5 only)

CMIP6 LOCA2 (SSP2-4.5 and SSP5-8.5 only)

CMIP6 all (SSP2-4.5 and SSP5-8.5 only)

**Abbreviations**

| | |
|---|---|
| CMIP6 | Coupled Model Intercomparison Project Phase 6 |
| NEX-GDDP | National Aeronautics and Space Administration Earth Exchange Global Daily Downscaled Projections |
| LOCA2 | Localized Constructed Analogs version 2 |
| SSP | Shared socioeconomic pathway |

Base modified from U.S. Census Bureau Tiger database,
Florida County Boundaries, 1:100,000,1990
Geographic coordinate system
World Geodetic System 1984 datum

Climate regions from
Irizarry-Ortiz and Haider
(2023)

**Figure 34.** Median 1-day, 100-year change factors at National Oceanic and Atmospheric Administration Atlas 14 station locations across Coupled Model Intercomparison Project Phase 6 (CMIP6) downscaled climate datasets considering all models and available shared socioeconomic pathways (SSPs) (unless otherwise indicated) for the period 2050–89. The panel labeled “CMIP6 all” considers all models from all CMIP6 downscaled climate datasets and SSPs. The panels including “(SSP2-4.5 and SSP5-8.5 only)” only consider those scenarios. The boundaries of the five climate regions shown in figure 2 are included for reference. Calculated median change factors from Irizarry-Ortiz and Haider (2023).

according to NOAA (2023). Over 20 in. of rainfall was recorded over a 72-hour period on June 11–13, 2024, in south Florida with some locations receiving over 27 in. of rainfall (Florida Climate Center, 2024). Areas in southwestern and southeastern Florida received the most rainfall, and hourly and daily rainfall records were broken during the event. A shift toward more frequent extremes, especially for rarer events, was documented in the IPCC's fifth assessment report (Collins and others, 2013) and further validated in a contributed section of their sixth assessment report (IPCC, 2021b). Attribution studies have determined that climate change has increased the likelihood and (or) intensity of these historical events. (See Reed and others [2020] for Hurricane Dorian, and Reed and Wehner [2023] for Hurricane Ian.)

Evidence of record-breaking precipitation extremes and their links to climate change, as referenced above, has been accumulating over the last few decades; however, given that the very high change factors computed here were generated by statistical downscaling or bias-corrected dynamical downscaling, the confidence in them is not as high as it would be if they had been generated by a purely physically based model. In addition, the highest change factors are associated with very long return periods, which are much longer than the number of years of data used in DDF fitting and are highly uncertain. High shape parameters of the GP distribution were fit especially for MACA because of isolated very large 1-day and multiday extremes, as discussed in Irizarry-Ortiz and others (2022). The quasi-stationary approach used in this study, whereby DDF curves are fit for a limited future 40-year projection period using local data, may also contribute in that it is possible that these very extreme precipitation events only happen once in a much longer period than the 40 years analyzed. These events, however, appear to be much more common in MACA than in the other downscaled climate datasets and may be, at least in part, a result of the downscaling method.

Wootten (2018) shows how subtle decisions performed in the process of statistical downscaling, such as tail adjustment, trace adjustment, and interpolation, can affect the accuracy of the prediction and increase the uncertainty in future projections, especially for extremes and event occurrence. Wang and others (2020) found that MACA projects significant increases in the 20-year daily event in New England compared to LOCA for which the projected changes are inconclusive over most of the area. In LOCA, model consensus is lacking over most of the region, but where models agree, the projected changes have a smaller magnitude than in MACA. Their finding is generally consistent with this study's findings for Florida. Wang and others (2020) note that projected changes in the mean annual maximum daily event are quite close between MACA-Livneh and MACA-gridMET but differ significantly between LOCA and MACA-Livneh. As a result, they conclude that differences in the projected changes are primarily caused by differences in the downscaling method, rather than by differences in the observational data used in training; however, LOCA and MACA used two different versions of the Livneh dataset for bias correction, which somewhat complicates the comparison.

The factors identified as potentially contributing to biases in DDF curves for the historical period, in addition to other factors such as scenario uncertainty and natural variability, contribute to the total uncertainty in derived change factors, as discussed in Irizarry-Ortiz and others (2022). Because of the large uncertainties in the derived change factors and associated future DDF curves, methods for decision making under deep uncertainty could be used to increase flexibility in the planning process. These methods are documented by Marchau and others (2019) and include decision scaling, robust decision making, and dynamic adaptive policy pathways, among others. Flexibility in the phasing and design of various flood control adaptation measures could reduce long-term costs while considering the evolution in climate science as well as local and global changes in climate and sea-level rise with consideration for potential tipping points. Research gaps and recommendations have also been outlined by Florida International University's Sea Level Solutions Center (Florida International University, 2021).

## Summary and Conclusions

Overall, a large variation in change factors was found across downscaled climate datasets, with change factors generally greater than 1 and generally increasing with return period. In general, median change factors were found to range within 1.01–1.58 for the period 2020–59 and 1.01–1.63 for 2050–89, depending on downscaled climate dataset, region, duration, and return period, indicating a projected overall increase in future extreme precipitation events. When data from all downscaled climate datasets are considered together, median change factors range within 1.04–1.18 for the period 2020–59 and within 1.04–1.23 for the period 2050–89, depending on region, duration, and return period. Spatial patterns in median change factors were found to vary by dataset.

The wide range of change factors computed in this study represent a set of plausible changes in extreme precipitation in the State of Florida. Given the wide range of change factors computed, users are encouraged to make application-specific judgments when deciding whether to use individual change factors or their central tendency for their projects. It is important to consider the many sources of uncertainty and that change factors obtained by statistical downscaling of general circulation model (GCM) output may not respect the physics of the precipitation-generating processes. For example, in statistical downscaling, precipitation amounts are neither limited by the amount of precipitable water in the atmosphere nor the presence or absence of moisture convergence. Statistical downscaling does not account for storm stalling from high-pressure system blocking or storm dynamics, including the potential for storm reinvigoration from additional latent heat release caused by warming and increasing atmospheric moisture, as well as enhanced cold-pool dynamics. Although the raw Coordinated Regional Downscaling Experiment (CORDEX) data (prior to bias correction) are generated by physically based dynamic downscaling of GCM output using regional climate models, some CORDEX models are not able to capture the annual cycle of precipitation in Florida, with some models either being completely out of phase or not able to capture the cycle amplitude. The bias-correction algorithm used by CORDEX generally fixes the seasonality problem, but the links to the physics are broken, also reducing confidence in the bias-corrected CORDEX output. This limits the use of some techniques for validating change factors, such as comparing whether they match or exceed expectations based on the Clausius-Clapeyron relationship, which requires local air-temperature projections that are physically consistent and concurrent and collocated with the extreme precipitation.

The National Aeronautics and Space Administration Earth Exchange Global Daily Downscaled Projections (NEX-GDDP) Coupled Model Intercomparison Project Phase 6 downscaled dataset followed by the Localized Constructed Analogs (LOCA) dataset perform the poorest in terms of being able to reproduce historical precipitation extremes indices. The NEX-GDDP, LOCA, and LOCA version 2 (LOCA2) datasets generally predict the lowest change factors. Conversely, the Multivariate Adaptive Constructed Analogs (MACA) dataset tends to better capture the historical precipitation extremes indices but results in the highest change factors, with median values of as much as ~1.6 for the 500-year return period in both future periods of interest. NEX-GDDP yields similar median change factors as the LOCA2 dataset, despite limitations with NEX-GDDP in terms of the training and bias-correction dataset and methods used, resulting in weak performance in terms of historical precipitation indices. The extremely high change factors obtained from MACA might be a result of the way the MACA procedure is known to amplify the change signal in the native GCMs. This issue is exacerbated by the extrapolation of high quantiles in the upper tail of the fitted probability distribution. Therefore, historical model and downscaled dataset performance may not be indicative of the quality of future projections and model culling may not be appropriate, especially when future extreme precipitation projections are developed using statistical methods and (or) bias correction of dynamically downscaled data without full consideration of physics. The extremely high change factors estimated from MACA occur at isolated stations instead of larger regions; therefore, confidence in their magnitude is low. Large differences exist between depth-duration-frequency (DDF) values derived from observations and DDF values derived from downscaled model precipitation for the historical period compared to the magnitude of the change from historical to future projection periods. Therefore, caution is advised when using these estimates because differences with respect to observations may be amplified in a nonmultiplicative manner in future projections.

The spatial patterns of median change factors are also quite different across the different downscaled climate datasets, which reduces confidence. Median change factors across climate regions and (or) datasets may be more reliable than values at individual stations from individual models or individual datasets. Because of the large uncertainties in the derived change factors and associated future DDF curves, users may decide to rely on the ensemble median of change factors. A benefit-risk analysis may help clarify a suitable range of change factors. Outliers at individual stations could be identified by comparison with change factors at other nearby locations and across models. It is well known that return levels and change factors for the longest return periods (100, 200, and 500 years) are the most uncertain and spatially variable. Confidence in a return level decreases rapidly when the return period is more than about twice the length of the original dataset. Even with the peaks-over-threshold approach used as part of this study, which increases the sample size used in fitting, change factors for the 100- to 500-year events remain highly uncertain and the most spatially variable. According to the World Meteorological Organization (2009), confidence in a return level decreases rapidly when the return period is more than about two times the period of record of the original dataset. The use of median change factors is recommended for these rarer events. For return periods above 100 years, an extension or adjustment of the percent change for lower return periods to higher return periods may need to be considered, as suggested by the National Oceanic and Atmospheric Administration (NOAA).

Code written in R language is provided as part of the data release associated with this report. The code allows users to be able to generate boxplots of change factors by station, for all stations in a hydrologic unit code 8 (HUC-8) basin, or by county in the State of Florida. The user has flexibility in defining the percentiles associated with the box and whiskers, including change factors based on all models or only the best models, and including data from one or more emissions scenarios. NOAA Atlas 14 stations in the Florida Keys are inactive in most of the downscaled model grids. As a result, data from the closest mainland grid cells to these four stations were often used in developing DDF curves at these four locations. Therefore, change factors developed for these four locations are highly uncertain and caution is advised.

When applying change factors to the historical NOAA Atlas 14 DDF curves to derive future precipitation DDF curves for the entire range of durations and return periods evaluated as part of this study, there is a possibility that the resulting future DDF curves may have fitted precipitation depths that decrease, rather than increase, for longer durations. Depending on the change factors used, this may happen in as much as 6 percent of cases. In such cases, the higher of the future precipitation depths derived for the duration of interest and the previous shorter duration may be a more conservative choice. Because of the large uncertainties in the derived change factors and associated future DDF curves, methods for decision making under deep uncertainty could be used to increase the flexibility in the planning process.

A high-resolution (1-kilometer) nonhydrostatic (convection-resolving) regional climate model is currently (as of 2026) being used for the State of Florida by the USGS to compute estimates of daily evapotranspiration. Such a convection-permitting model can better capture local microclimatic conditions including sea- and lake-breeze interactions, land use changes, and so forth, and could reduce some of the uncertainties associated with the existing coarse-resolution dynamically downscaled data products and especially with the statistical-downscaling methods. Higher-resolution convection-permitting models have been shown to improve the representation of extreme precipitation, especially on subdaily timescales and for summer high-intensity precipitation events compared to coarser-scale regional models with parameterized convection, such as those used by CORDEX, which tend to produce rainfall that is too light and widespread. In addition, the simulation of tropical cyclones has been shown to be improved when using convection-permitting models.

## References Cited

Abatzoglou, J.T., 2013, Development of gridded surface meteorological data for ecological applications and modelling: International Journal of Climatology, v. 33, no. 1, p. 121–131, accessed July 7, 2022, at https://doi.org/10.1002/joc.3413. [Data available at http://thredds.northwestknowledge.net:8080/thredds/reacch_climate_MET_aggregated_catalog.html.]

Abatzoglou, J.T., and Brown, T.J., 2012, A comparison of statistical downscaling methods suited for wildfire applications: International Journal of Climatology, v. 32, no. 5, p. 772–780, accessed July 7, 2022, at https://doi.org/10.1002/joc.2312.

Abatzoglou, J., and Hegewisch, K.C., 2016, Multivariate Adaptive Constructed Analogs (MACA) CMIP5 statistically downscaled data for coterminous USA: U.S. Geological Survey data release, https://doi.org/10.21429/kpm4-km13.

Akaike, H., 1973, Information theory and an extension of the maximum likelihood principle, *in* International Symposium on Information Theory, 2d, Tsahkadsor, Armenia, USSR, September 2–8, 1971, [Proceedings]: Budapest, Hungary, Akademiai Kiado, p. 267–281. [Reprinted in 1998. Also available at https://doi.org/10.1007/978-1-4612-1694-0_15.]

Asadieh, B., and Krakauer, N.Y., 2015, Global trends in extreme precipitation—Climate models versus observations: Hydrology and Earth System Sciences, v. 19, no. 2, p. 877–891, accessed July 7, 2022, at https://doi.org/10.5194/hess-19-877-2015.

Asquith, W.H., 1998, Depth-duration frequency of precipitation for Texas: U.S. Geological Survey Water Resources Investigations Report 98–4404, 107 p., accessed July 7, 2022, at https://doi.org/10.3133/wri984044.

Avery, C.W., Reidmiller, D.R., Kolian, M., Kunkel, K.E., Herring, D., Sherman, R., Sweet, W.V., Tipton, K., and Weaver, C., 2018, Data tools and scenario products, *in* Reidmiller, D.R., Avery, C.W., Easterling, D.R., Kunkel, K.E., Lewis, K.L.M., Maycock, T.K., and Stewart, B.C., eds., Impacts, risks, and adaptation in the United States, v. 2 *of* Fourth National Climate Assessment: Washington, D.C., U.S. Global Change Research Program, p. 1413–1430, accessed July 7, 2022, at https://doi.org/10.7930/NCA4.2018.AP3.

Avila-Diaz, A., Benezoli, V., Justino, F., Torres, R., and Wilson, A., 2020, Assessing current and future trends of climate extremes across Brazil based on reanalyses and earth system model projections: Climate Dynamics, v. 55, nos. 5–6, p. 1403–1426, accessed July 3, 2024, at https://doi.org/10.1007/s00382-020-05333-z.

Barnard, P.L., Befus, K.M., Danielson, J.J., Engelstad, A.C., Erickson, L.H., Foxgrover, A.C., Hayden, M.K., Hoover, D.J., Leijnse, T.W.B., Massey, C., McCall, R., Nadal-Caraballo, N.C., Nederhoff, K., O'Neill, A.C., Parker, K.A., Shirzaei, M., Ohenhen, L.O., Swarzenski, P.W., Thomas, J.A., van Ormondt, M., Vitousek, S., Vos, K., Wood, N.J., Jones, J.M., and Jones, J.L., 2024, Projections of multiple climate-related coastal hazards for the US Southeast Atlantic: Nature Climate Change, v. 15, p. 101−109, accessed February 13, 2026, at https://doi.org/10.1038/s41558-024-02180-2.

Basile, S., Crimmins, A.R., Avery, C.W., Hamlington, B.D., and Kunkel, K.E., 2023, Appendix 3. Scenarios and datasets, *in* Crimmins, A.R., Avery, C.W., Easterling, D.R., Kunkel, K.E., Stewart, B.C., and Maycock, T.K., eds., Fifth National Climate Assessment: Washington, D.C., U.S. Global Change Research Program, 10 p., accessed January 5, 2024, at https://doi.org/10.7930/NCA5.2023.A3.

Behnke, R., Vavrus, S., Allstadt, A., Albright, T., Thogmartin, W.E., and Radeloff, V.C., 2016, Evaluation of downscaled, gridded climate data for the conterminous United States: Ecological Applications, v. 26, no. 5, p. 1338–1351, accessed July 7, 2022, at https://doi.org/10.1002/15-1061.

Bukovsky, M.S., Gao, J., Mearns, L.O., and O’Neill, B.C., 2021, SSP-based land-use change scenarios—A critical uncertainty in future regional climate change projections: Earth’s Future, v. 9, no. 3, article e2020EF001782, accessed August 2, 2022, at https://doi.org/10.1029/2020EF001782.

Burnham, K.P., and Anderson, D.R., 2002, Model selection and multimodel inference—A practical information-theoretic approach (2d ed.): New York, Springer Science and Business Media, 488 p., accessed July 7, 2022, at https://doi.org/10.1007/b97636.

Burnham, K.P., Anderson, D.R., and Huyvaert, K.P., 2011, AIC model selection and multimodel inference in behavioral ecology—Some background, observations, and comparisons: Behavioral Ecology and Sociobiology, v. 65, no. 1, p. 23–35, accessed July 7, 2022, at https://doi.org/10.1007/s00265-010-1029-6.

Byrne, M.P., Pendergrass, A.G., Rapp, A.D., and Wodzicki, K.R., 2018, Response of the Intertropical Convergence Zone to climate change—Location, width, and strength: Current Climate Change Reports, v. 4, no. 4, p. 355–370, accessed July 7, 2022, at https://doi.org/10.1007/s40641-018-0110-5.

Campbell, J.D., Taylor, M.A., Bezanilla-Morlot, A., Stephenson, T.S., Centella-Artola, A., Clarke, L.A., and Stephenson, K.A., 2021, Generating projections for the Caribbean at 1.5, 2.0 and 2.5 °C from a high-resolution ensemble: Atmosphere (Basel), v. 12, no. 3, article 328, 27 p., accessed July 7, 2022, at https://doi.org/10.3390/atmos12030328.

Cannon, A.J., 2018, Multivariate quantile mapping bias correction—An N-dimensional probability density function transform for climate model simulations of multiple variables: Climate Dynamics, v. 50, nos. 1–2, p. 31–49, accessed July 7, 2022, at https://doi.org/10.1007/s00382-017-3580-6.

Cannon, A.J., Sobie, S.R., and Murdock, T.Q., 2015, Bias correction of GCM precipitation by quantile mapping—How well do methods preserve changes in quantiles and extremes?: Journal of Climate, v. 28, no. 17, p. 6938–6959, accessed July 7, 2022, at https://doi.org/10.1175/JCLI-D-14-00754.1.

Cardona, O.D., van Aalst, M.K., Birkmann, J., Fordham, M., McGregor, G., Perez, R., Pulwarty, R.S., Schipper, E.L.S., and Sihn, B.T., 2012, Determinants of risk—Exposure and vulnerability, *in* Field, C.B., Barros, V., Stocker, T.F., Qin, D., Dokken, D.J., Ebi, K.L., Mastrandrea, M.D., Mach, K.J., Plattner, G.-K., Allen, S.K., Tignor, M., and Midgley, P.M., eds., Managing the risks of extreme events and disasters to advance climate change adaptation—A special report of Working Groups I and II of the Intergovernmental Panel on Climate Change (IPCC): Cambridge, United Kingdom, and New York, Cambridge University Press, p. 65–108, accessed February 6, 2026, at https://doi.org/10.1017/CBO9781139177245.

Chen, C.-T., and Knutson, T., 2008, On the verification and comparison of extreme rainfall indices from climate models: Journal of Climate, v. 21, no. 7, p. 1605–1621, accessed July 7, 2022, at https://doi.org/10.1175/2007JCLI1494.1.

Chen, W., Jiang, Z., and Li, L., 2011, Probabilistic projections of climate change over China under the SRES A1B scenario using 28 AOGCMs: Journal of Climate, v. 24, no. 17, p. 4741–4756, accessed July 7, 2022, at https://doi.org/10.1175/2011JCLI4102.1.

Coles, S., 2001, An introduction to statistical modeling of extreme values: Springer-Verlag, 219 p. [Also available at https://doi.org/10.1007/978-1-4471-3675-0.]

Collins, M., Knutti, R., Arblaster, J., Dufresne, J.-L., Fichefet, T., Friedlingstein, P., Gao, X., Gutowski, W.J., Johns, T., Krinner, G., Shongwe, M., Tebaldi, C., Weaver, A.J., and Wehner, M., 2013, Long-term climate change—Projections, commitments and irreversibility, *in* Stocker, T.F., Qin, D., Plattner, G.-K., Tignor, M., Allen, S.K., Boschung, J., Nauels, A., Xia, Y., Bex, V., and Midgley, P.M., eds., Climate Change 2013—The physical science basis—Contribution of Working Group I to the Fifth Assessment Report of the Intergovernmental Panel on Climate Change: Cambridge, United Kingdom, and New York, Cambridge University Press, p. 1029–1136, accessed July 7, 2022, at https://doi.org/10.1017/CBO9781107415324.024.

Daly, C., Doggett, M.K., Smith, J.I., Olson, K.V., Halbleib, M.D., Dimcovic, Z., Keon, D., Loiselle, R.A., Steinberg, B., Ryan, A.D., Pancake, C.M., and Kaspar, E.M., 2021, Challenges in observation-based mapping of daily precipitation across the conterminous United States: Journal of Atmospheric and Oceanic Technology, v. 38, no. 11, p. 1979–1992, accessed July 7, 2022, at https://doi.org/10.1175/JTECH-D-21-0054.1.

Daly, C., Halbleib, M., Smith, J.I., Gibson, W.P., Doggett, M.K., Taylor, G.H., Curtis, J., and Pasteris, P.P., 2008, Physiographically sensitive mapping of climatological temperature and precipitation across the conterminous United States: International Journal of Climatology, v. 28, no. 15, p. 2031–2064, accessed July 7, 2022, at https://doi.org/10.1002/joc.1688.

Davison, A.C., and Smith, R.L., 1990, Models for exceedances over high thresholds: Journal of the Royal Statistical Society, Series B, Statistical Methodology, v. 52, no. 3, p. 393–425, accessed July 7, 2022, at https://doi.org/10.1111/j.2517-6161.1990.tb01796.x.

Decker, J.D., Hughes, J.D., and Swain, E.D., 2019, Potential for increased inundation in flood-prone regions of southeast Florida in response to climate and sea-level changes in Broward County, Florida, 2060–69: U.S. Geological Survey Scientific Investigations Report 2018–5125, 106 p., accessed February 13, 2026, at https://doi.org/10.3133/sir20185125.

Donat, M.G., Alexander, L.V., Yang, H., Durre, I., Vose, R., Dunn, R.J.H., Willett, K.M., Aguilar, E., Brunet, M., Caesar, J., Hewitson, B., Jack, C., Klein Tank, A.M.G., Kruger, A.C., Marengo, J., Peterson, T.C., Renom, M., Oria Rojas, C., Rusticucci, M., Salinger, J., Elrayah, A.S., Sekele, S.S., Srivastava, A.K., Trewin, B., Villarroel, C., Vincent, L.A., Zhai, P., Zhang, X., and Kitching, S., 2013, Updated analyses of temperature and precipitation extreme indices since the beginning of the twentieth century—The HadEX2 dataset: Journal of Geophysical Research, Atmospheres, v. 118, no. 5, p. 2098–2118, accessed July 7, 2022, at https://doi.org/10.1002/jgrd.50150.

Donat, M.G., Sillmann, J., Wild, S., Alexander, L.V., Lippmann, T., and Zwiers, F.W., 2014, Consistency of temperature and precipitation extremes across various global gridded in situ and reanalysis datasets: Journal of Climate, v. 27, no. 13, p. 5019–5035, accessed July 7, 2022, at https://doi.org/10.1175/JCLI-D-13-00405.1.

Durbin, J., 1960, The fitting of time-series models: Review of the International Statistical Institute, v. 28, no. 3, p. 233–244, accessed July 17, 2024, at https://doi.org/10.2307/1401322.

Ensor, L.A., and Robeson, S.M., 2008, Statistical characteristics of daily precipitation—Comparisons of gridded and point datasets: Journal of Applied Meteorology and Climatology, v. 47, no. 9, p. 2468–2476, accessed December 3, 2024, at https://doi.org/10.1175/2008JAMC1757.1.

Expert Team on Climate Change Detection and Indices, 2009, ETCCDI Climate Change Indices: Expert Team on Climate Change Detection and Indices (ETCCDI) web page, accessed February 13, 2026, at https://etccdi.pacificclimate.org/list_27_indices.shtml.

Eyring, V., Bony, S., Meehl, G.A., Senior, C.A., Stevens, B., Stouffer, R.J., and Taylor, K.E., 2016, Overview of the Coupled Model Intercomparison Project Phase 6 (CMIP6) experimental design and organization: Geoscientific Model Development, v. 9, no. 5, p. 1937–1958, accessed July 7, 2022, at https://doi.org/10.5194/gmd-9-1937-2016.

Falgout, J.T., Gordon, J., Williams, B., and Davis, M.J., 2023, USGS Advanced Research Computing—USGS Denali supercomputer: U.S. Geological Survey web page, accessed June 25, 2024, at https://doi.org/10.5066/P9PSW367.

Ferro, C.A.T., 2003, Statistical methods for clusters of extreme values: Lancaster, England, Lancaster University, Ph.D. dissertation, 180 p., accessed October 15, 2020, at https://empslocal.ex.ac.uk/people/staff/ferro/Publications/Thesis/thesis.pdf.

Ferro, C.A.T., and Segers, J., 2003, Inference for clusters of extreme values: Journal of the Royal Statistical Society, Series B, Statistical Methodology, v. 65, no. 2, p. 545–556, accessed July 7, 2022, at https://doi.org/10.1111/1467-9868.00401.

Fisher, R.A., and Tippett, L.H.C., 1928, Limiting forms of the frequency distribution of the largest or smallest member of a sample: Mathematical Proceedings of the Cambridge Philosophical Society, v. 24, no. 2, p. 180–190, accessed July 7, 2022, at https://doi.org/10.1017/S0305004100015681.

Florida Climate Center, 2023, Climate summary for Florida—April 2023: Florida State University web page, accessed July 9, 2024, at https://climatecenter.fsu.edu/products-services/summaries?view=article&id=629.

Florida Climate Center, 2024, Climate summary for Florida—June 2024: Florida State University web page, accessed July 9, 2024, at https://climatecenter.fsu.edu/products-services/summaries?view=article&id=645.

Florida Department of Environmental Protection, 2016, Water management district boundaries: Florida Geospatial Open Data Portal, accessed February 13, 2026, at https://geodata.floridagio.gov/datasets/sfwmd::water-management-district-boundaries/about. [Last modified October 31, 2021.]

Florida International University, 2021, DRAFT annual climate science report 2020—Implications for SFWMD's mission and recommendations: Florida International University, Sea Level Solutions Center, 43 p.

Florida Senate, 2021, CS/CS/SB 1954—Statewide flooding and sea level rise resilience: Florida Senate General Bill, accessed May 31, 2023, at https://www.flsenate.gov/Session/Bill/2021/1954/.

Fredriksen, H.-B., Smith, C.J., Modak, A., and Rugenstein, M., 2023, 21st century scenario forcing increases more for CMIP6 than CMIP5 models: Geophysical Research Letters, v. 50, no. 6, article e2023GL102916, accessed July 1, 2024, at https://doi.org/10.1029/2023GL102916.

Gibson, P., 2021, Python code to compute ETCCDI climate indices [ETCCDI_precip.py, CPC_ETCCDI_Wrapper.py]: National Center for Atmospheric Research (NCAR) web page, accessed February 12, 2021, at https://github.com/Peter-Gibson/climate/tree/CLIMATE-937/examples.

Gilleland, E., and Katz, R.W., 2016, extRemes 2.0—An extreme value analysis package in R: Journal of Statistical Software, v. 72, no. 8, accessed July 7, 2022, at https://doi.org/10.18637/jss.v072.i08.

Giorgi, F., Jones, C., and Asrar, G.R., 2009, Addressing climate information needs at the regional level—The CORDEX framework: World Meteorological Society Bulletin, v. 58, no. 3, p. 175–183, accessed July 7, 2022, at https://wmo.int/media/magazine-article/addressing-climate-information-needs-regional-level-cordex-framework.

Gleckler, P.J., Taylor, K.E., and Doutriaux, C., 2008, Performance metrics for climate models: Journal of Geophysical Research, v. 113, no. D6, article 2007JD008972, accessed July 7, 2022, at https://doi.org/10.1029/2007JD008972.

Guttman, N.B., and Quayle, R.G., 1996, A historical perspective of U.S. climate divisions: Bulletin of the American Meteorological Society, v. 77, no. 2, p. 293–303, accessed June 25, 2024, at https://doi.org/10.1175/1520-0477(1996)077<0293:AHPOUC>2.0.CO;2.

Hart, E.M., and Bell, K., 2015, prism—R package (ver. 0.06): Corvallis, Ore., Oregon State University, PRISM Climate Data project, accessed July 7, 2022, at https://github.com/ropensci/prism. [Data available at https://doi.org/10.5281/zenodo.33663.]

Hausfather, Z., and Peters, G.P., 2020, Emissions—The ‘business as usual’ story is misleading: Nature, v. 577, p. 618–620, accessed February 13, 2006, at https://doi.org/10.1038/d41586-020-00177-3.

Hersbach, H., Bell, B., Berrisford, P., Hirahara, S., Horányi, A., Muñoz-Sabater, J., Nicolas, J., Peubey, C., Radu, R., Schepers, D., Simmons, A., Soci, C., Abdalla, S., Abellan, X., Balsamo, G., Bechtold, P., Biavati, G., Bidlot, J., Bonavita, M., De Chiara, G., Dahlgren, P., Dee, D., Diamantakis, M., Dragani, R., Flemming, J., Forbes, R., Fuentes, M., Geer, A., Haimberger, L., Healy, S., Hogan, R.J., Hólm, E., Janisková, M., Keeley, S., Laloyaux, P., Lopez, P., Lupu, C., Radnoti, G., de Rosnay, P., Rozum, I., Vamborg, F., Villaume, S., and Thépaut, J.-N., 2020, The ERA5 global reanalysis: Quarterly Journal of the Royal Meteorological Society, v. 146, no. 730, p. 1999–2049, accessed August 2, 2025, at https://doi.org/10.1002/qj.3803.

Hershfield, D.M., 1961, Rainfall frequency atlas of the United States for durations from 30 minutes to 24 hours and return periods from 1 to 100 years: Washington, D.C., U.S. Department of Commerce, Weather Bureau Technical Paper No. 40, 115 p.

Hosking, J.R.M., 1990, L-moments—Analysis and estimation of distributions using linear combinations of order statistics: Journal of the Royal Statistical Society, Series B, Statistical Methodology, v. 52, no. 1, p. 105–124, accessed July 7, 2022, at https://doi.org/10.1111/j.2517-6161.1990.tb01775.x.

Hourdin, F., Mauritsen, T., Gettelman, A., Golaz, J.-C., Balaji, V., Duan, Q., Folini, D., Ji, D., Klocke, D., Qian, Y., Rauser, F., Rio, C., Tomassini, L., Watanabe, M., and Williamson, D., 2017, The art and science of climate model tuning: Bulletin of the American Meteorological Society, v. 98, no. 3, p. 589–602, accessed July 7, 2022, at https://doi.org/10.1175/BAMS-D-15-00135.1.

Infanti, J.M., Kirtman, B.P., Aumen, N.G., Stamm, J., and Polsky, C., 2020, Aligning climate models with stakeholder needs—Advances in communicating future rainfall uncertainties for South Florida decision makers: Earth and Space Science, v. 7, no. 7, article e2019EA000725, accessed February 13, 2026, at https://doi.org/10.1029/2019EA000725.

Intergovernmental Panel on Climate Change [IPCC], 2013, Summary for policymakers, *in* Stocker, T.F., Qin, D., Plattner, G.-K., Tignor, M., Allen, S.K., Boschung, J., Nauels, A., Xia, Y., Bex, V., and Midgley, P.M., eds., Climate Change 2013—The physical science basis—Contribution of Working Group I to the Fifth Assessment Report of the Intergovernmental Panel on Climate Change: Cambridge, United Kingdom, and New York, Cambridge University Press, p. 1029–1136, accessed October 1, 2022, at https://doi.org/10.1017/CBO9781107415324.004.

Intergovernmental Panel on Climate Change [IPCC], 2021a, Framing, context, and methods, chap. 1 *in* Masson-Delmotte, V., Zhai, P., Pirani, A., Connors, S.L., Péan, C., Berger, S., Caud, N., Chen, Y., Goldfarb, L, Gomis, M.I., Huang, M., Leitzell, K., Lonnoy, E., Matthews, J.B.R., Maycock, T.K., Waterfield, T., Yelekçi, O., Yu, R., and Zhou, B., eds., Climate Change 2021—The physical science basis. Contribution of Working Group I to the Sixth Assessment Report of the Intergovernmental Panel on Climate Change: Cambridge, United Kingdom, and New York, Cambridge University Press, p. 147–286, accessed July 1, 2024, at https://doi.org/10.1017/9781009157896.003.

Intergovernmental Panel on Climate Change [IPCC], 2021b, Summary for policymakers, *in* Masson-Delmotte, V., Zhai, P., Pirani, A., Connors, S.L., Péan, C., Berger, S., Caud, N., Chen, Y., Goldfarb, L, Gomis, M.I., Huang, M., Leitzell, K., Lonnoy, E., Matthews, J.B.R., Maycock, T.K., Waterfield, T., Yelekçi, O., Yu, R., and Zhou, B., eds., Climate Change 2021—The physical science basis. Contribution of Working Group I to the Sixth Assessment Report of the Intergovernmental Panel on Climate Change: Cambridge, United Kingdom, and New York, Cambridge University Press, p. 3–32, accessed July 7, 2022, at https://www.ipcc.ch/report/ar6/wg1/downloads/report/IPCC_AR6_WGI_SPM.pdf.

Intergovernmental Panel on Climate Change [IPCC], 2023, Core writing team, sec. 2 *in* Lee, H., and Romero, J., eds., Climate Change 2023—Synthesis report. Contribution of Working Groups I, II and III to the Sixth Assessment Report of the Intergovernmental Panel on Climate Change: Geneva, Switzerland, Intergovernmental Panel on Climate Change, p. 35–115, accessed July 1, 2024, at https://doi.org/10.59327/IPCC/AR6-9789291691647.

Irizarry-Ortiz, M.M., and Haider, S.M., 2023, Change factors to derive projected future precipitation depth-duration-frequency (DDF) curves at 242 National Oceanic and Atmospheric Administration (NOAA) Atlas 14 stations in Florida (ver. 3.0, August 2025): U.S. Geological Survey data release, https://doi.org/10.5066/P9Q3LEIL.

Irizarry-Ortiz, M.M., Stamm, J.F., Maran, C., and Obeysekera, J., 2022, Development of projected depth-duration frequency curves (2050–89) for south Florida: U.S. Geological Survey Scientific Investigations Report 2022–5093, 114 p., accessed May 30, 2023, at https://doi.org/10.3133/sir20225093.

Jenkinson, A.F., 1955, The frequency distribution of the annual maximum (or minimum) values of meteorological elements: Quarterly Journal of the Royal Meteorological Society, v. 81, no. 348, p. 158–171, accessed July 7, 2022, at https://doi.org/10.1002/qj.49708134804.

Jiang, Z., Li, W., Xu, J., and Li, L., 2015, Extreme precipitation indices over China in CMIP5 models—Part I. Model evaluation: Journal of Climate, v. 28, no. 21, p. 8603–8619, accessed July 7, 2022, at https://doi.org/10.1175/JCLI-D-15-0099.1.

Jupiter Intelligence, 2021, Future downscaled rainfall for south Florida: Florida International University and South Florida Water Management District, prepared by Jupiter Intelligence, 19 p.

Katz, R.W., Parlange, M.B., and Naveau, P., 2002, Statistics of extremes in hydrology: Advances in Water Resources, v. 25, nos. 8–12, p. 1287–1304, accessed July 7, 2022, at https://doi.org/10.1016/S0309-1708(02)00056-8.

Kendall, M.G., 1970, Rank correlation methods (4th ed.): London, Charles Griffin, 202 p.

Langbein, W.B., 1949, Annual floods and the partial-duration flood series: Transactions, American Geophysical Union, v. 30, no. 6, p. 879–881, accessed July 7, 2022, at https://doi.org/10.1029/TR030i006p00879.

Lanzante, J.R., Dixon, K.W., Adams-Smith, D., Nath, M.J., and Whitlock, C.E., 2021, Evaluation of some distributional downscaling methods as applied to daily precipitation with an eye towards extremes: International Journal of Climatology, v. 41, no. 5, p. 3186–3202, accessed July 7, 2022, at https://doi.org/10.1002/joc.7013.

Lawrence Berkeley Lab, 2023, Globus collection [LOCA2 collection]: Globus web page, accessed January 27, 2023, at https://app.globus.org/file-manager?origin_id=8b53db8a-d0e2-11ec-b95d-0f43df60473d&origin_path=%2F%7E%2Floca2-gdo%2F.

Lawrence Livermore National Laboratory, 2022a, PCMDI—Earth System Model Evaluation Project, CMIP5 data—Getting started: Lawrence Livermore National Laboratory web page, accessed February 25, 2025, at https://pcmdi.llnl.gov/mips/cmip5/data-access-getting-started.html.

Lawrence Livermore National Laboratory, 2022b, PCMDI—Earth System Model Evaluation Project, a guide to CMIP6 participation: Lawrence Livermore National Laboratory web page, accessed February 25, 2025, at https://pcmdi.llnl.gov/CMIP6/Guide/index.html.

Leadbetter, M.R., Lindgren, G., and Rootzen, H., 1983, Extremes and related properties of random sequences and processes: Springer Series in Statistics, 348 p., accessed July 7, 2022, at https://doi.org/10.1007/978-1-4612-5449-2.

Liu, C., Ikeda, K., Rasmussen, R., Barlage, M., Newman, A.J., Prein, A.F., Chen, F., Chen, L., Clark, M., Dai, A., Dudhia, J., Eidhammer, T., Gochis, D., Gutmann, E., Kurkute, S., Li, Y., Thompson, G., and Yates, D., 2017, Continental-scale convection-permitting modeling of the current and future climate of North America: Climate Dynamics, v. 49, nos. 1–2, p. 71–95, accessed July 7, 2022, at https://doi.org/10.1007/s00382-016-3327-9.

Livneh, B., Bohn, T.J., Pierce, D.W., Munoz-Arriola, F., Nijssen, B., Vose, R., Cayan, D.R., and Brekke, L., 2015, A spatially comprehensive, hydrometeorological data set for Mexico, the U.S., and southern Canada 1950–2013: Scientific Data, v. 2, no. 1, article 150042, accessed July 7, 2022, at https://doi.org/10.1038/sdata.2015.42. [Data available at https://www.ncei.noaa.gov/access/metadata/landing-page/bin/iso?id=gov.noaa.nodc:0129374.]

Livneh, B., Rosenberg, E.A., Lin, C., Nijssen, B., Mishra, V., Andreadis, K.M., Maurer, E.P., and Lettenmaier, D.P., 2013, A long-term hydrologically based dataset of land surface fluxes and states for the conterminous United States—Update and extensions: Journal of Climate, v. 26, no. 23, p. 9384–9392, accessed July 7, 2022, at https://doi.org/10.1175/JCLI-D-12-00508.1. [Data available at http://thredds.northwestknowledge.net:8080/thredds/catalog/NWCSC_INTEGRATED_SCENARIOS_ALL_CLIMATE/macav2livneh/livneh_CANv1.1_USv1.0/catalog.html.]

Lopez-Cantu, T., Prein, A.F., and Samaras, C., 2020, Uncertainties in future U.S. extreme precipitation from downscaled climate projections: Geophysical Research Letters, v. 47, no. 9, article e2019GL086797, accessed July 7, 2022, at https://doi.org/10.1029/2019GL086797.

Lusher, W.R., Jackson, J.L., and Morgan, K.T., 2008, The Florida Automated Weather Network: Ten years of providing weather information for Florida growers: Proceedings of the Florida State Horticultural Society, v. 121, p. 69−74, accessed February 6, 2026, at https://journals.flvc.org/fshs/article/view/87350/84130.

Madaus, L., McDermott, P., Hacker, J., and Pullen, J., 2020, Hyper-local, efficient extreme heat projection and analysis using machine learning to augment a hybrid dynamical-statistical downscaling technique: Urban Climate, v. 32, article 100606, accessed July 7, 2022, at https://doi.org/10.1016/j.uclim.2020.100606.

Mann, H.B., 1945, Non-parametric tests against trend: Econometrica, v. 13, no. 3, p. 245–259, accessed July 17, 2024, at https://doi.org/10.2307/1907187.

Marchau, V.A.W.J., Walker, W.E., Bloemen, P.J.T.M., and Popper, S.W., eds., 2019, Decision making under deep uncertainty from theory to practice (1st ed.): Cham, Switzerland, Springer, 405 p., accessed July 7, 2022, at https://doi.org/10.1007/978-3-030-05252-2.

Marvel, K., Su, W., Delgado, R., Aarons, S., Chatterjee, A., Garcia, M.E., Hausfather, Z., Hayhoe, K., Hence, D.A., Jewett, E.B., Robel, A., Singh, D., Tripati, A., and Vose, R.S., 2023, Climate trends, chap. 2 *in* Crimmins, A.R., Avery, C.W., Easterling, D.R., Kunkel, K.E., Stewart, B.C., and Maycock, T.K., eds., Fifth National Climate Assessment: Washington, D.C., U.S. Global Change Research Program, p. 24–25, accessed January 5, 2024, at https://doi.org/10.7930/NCA5.2023.CH2.

Maurer, E.P., and Hidalgo, H.G., 2008, Utility of daily vs. monthly large-scale climate data—An intercomparison of two statistical downscaling methods: Hydrology and Earth System Sciences, v. 12, no. 2, p. 551–563, accessed May 30, 2023, at https://doi.org/10.5194/hess-12-551-2008.

Mauritsen, T., Stevens, B., Roeckner, E., Crueger, T., Esch, M., Giorgetta, M., Haak, H., Jungclaus, J., Klocke, D., Matei, D., Mikolajewicz, U., Notz, D., Pincus, R., Schmidt, H., and Tomassini, L., 2012, Tuning the climate of a global model: Journal of Advances in Modeling Earth Systems, v. 4, no. 3, article M00A01, accessed July 7, 2022, at https://doi.org/10.1029/2012MS000154.

Max Planck Institute for Meteorology, 2022a, Climate data operators: Max Planck Institute for Meteorology web page, accessed August 1, 2022, at https://code.mpimet.mpg.de/projects/cdo.

Max Planck Institute for Meteorology, 2022b, CDO{rb,py}: Max Planck Institute for Meteorology web page, accessed August 1, 2022, at https://code.mpimet.mpg.de/projects/cdo/wiki/Cdo%7Brbpy%7D.

Max Planck Institute for Meteorology, 2022c, CDO Users Guide: Max Planck Institute for Meteorology web page, accessed February 10, 2026, at https://code.mpimet.mpg.de/projects/cdo/embedded/index.html#x1-7310002.12.3.

Mearns, L.O., and others, 2017, The NA-CORDEX dataset (ver. 1.0): Boulder, Colo., National Center for Atmospheric Research (NCAR) Climate Data Gateway web page, accessed January 2022 at https://doi.org/10.5065/D6SJ1JCH. [Bias correction error documented at https://na-cordex.org/bias-correction-error.html.]

Misra, V., Carlson, E., Craig, R.K., Enfield, D., Kirtman, B., Landing, W., Lee, S.-K., Letson, D., Marks, F., Obeysekera, J., Powell, M., and Shin, S.-I., 2011, Climate scenarios—A Florida-centric view: Florida Climate Change Task Force, 71 p., accessed July 7, 2022, at https://www.ces.fau.edu/publications/pdfs/climate_scenario.pdf.

Moloney, N.R., Faranda, D., and Sato, Y., 2019, An overview of the extremal index: Chaos, v. 29, 022101, accessed February 13, 2020, at https://doi.org/10.1063/1.5079656.

National Aeronautics and Space Administration [NASA] Center for Climate Simulation, 2022, NCCS THREDDS data catalog—AMES NEX GDDP for CMIP6: National Aeronautics and Space Administration (NASA) database, accessed June 6, 2022, at https://ds.nccs.nasa.gov/thredds/catalog/AMES/NEX/GDDP-CMIP6/catalog.html.

National Center for Atmospheric Research [NCAR], 2021, Climate Data Gateway at NCAR—NA-CORDEX search [variable, prec, pr; experiment, hist; frequency, day; grid, NAM-22i, NAM-44i; bias correction, mbcn-gridMET, mbcn-Daymet]: National Center for Atmospheric Research (NCAR) database, accessed November 22, 2021, at https://www.earthsystemgrid.org/search/cordexsearch.html.

National Center for Atmospheric Research [NCAR], 2022, Climate Data Gateway—NA-CORDEX search [variable, prec, pr; experiment, rcp45, rcp85; frequency, day; grid, NAM-22i, NAM-44i; bias correction, mbcn-gridMET, mbcn-Daymet]: National Center for Atmospheric Research (NCAR) database, accessed January 13, 2022, at https://www.earthsystemgrid.org/search/cordexsearch.html.

National Oceanic and Atmospheric Administration [NOAA], 2011, NOAA/NCEI U.S. climate division data plotting page—Division boundaries and county relationships: National Oceanic and Atmospheric Administration (NOAA) National Centers for Environmental Information web page, accessed April 21, 2021, at https://psl.noaa.gov/data/usclimdivs/boundaries.html. [Data available at ftp://ftp.ncdc.noaa.gov/pub/data/cirs/climdiv/CONUS_CLIMATE_DIVISIONS.shp.zip.]

National Oceanic and Atmospheric Administration [NOAA], 2017, National Hurricane Center tropical cyclone report, Hurricane Irma (AL112017): National Oceanic and Atmospheric Administration (NOAA) web page, accessed July 9, 2024, at https://www.nhc.noaa.gov/data/tcr/AL112017_Irma.pdf.

National Oceanic and Atmospheric Administration [NOAA], 2020a, National Hurricane Center tropical cyclone report, Hurricane Dorian (AL052019): National Oceanic and Atmospheric Administration (NOAA) web page, accessed February 9, 2022, at https://www.nhc.noaa.gov/data/tcr/AL052019_Dorian.pdf.

National Oceanic and Atmospheric Administration [NOAA], 2020b, National Hurricane Center tropical cyclone report, Hurricane Eta (AL292020): National Oceanic and Atmospheric Administration (NOAA) web page, accessed July 9, 2024, at https://www.nhc.noaa.gov/data/tcr/AL292020_Eta.pdf.

National Oceanic and Atmospheric Administration [NOAA], 2022a, Analysis of impact of nonstationary climate on NOAA Atlas 14 estimates—Assessment report: National Oceanic and Atmospheric Administration (NOAA), National Weather Service, Office of Water Prediction, 275 p., accessed February 11, 2022, at https://hdsc.nws.noaa.gov/pfds/files25/NA14_Assessment_report_202201v1.pdf.

National Oceanic and Atmospheric Administration [NOAA], 2022b, National Hurricane Center tropical cyclone report, Hurricane Ian (AL092022): National Oceanic and Atmospheric Administration (NOAA) web page, accessed July 9, 2024, at https://www.nhc.noaa.gov/data/tcr/AL092022_Ian.pdf.

National Oceanic and Atmospheric Administration [NOAA], 2023, April 2023 National Climate Report: National Oceanic and Atmospheric Administration (NOAA) web page, accessed July 8, 2024, at https://www.ncei.noaa.gov/access/monitoring/monthly-report/national/202304.

National Weather Service, 2020, Precipitation Frequency Data Server: National Oceanic and Atmospheric Administration (NOAA) database, accessed December 10, 2020, at https://hdsc.nws.noaa.gov/pfds.

Northwest Knowledge Network [NKN], 2021, THREDDS aggregated data catalog [climatic modeling MACAv2Livneh]: NKN database, accessed February 3, 2021, at http://thredds.northwestknowledge.net:8080/thredds/nw.csc.climate-macav2livneh.aggregated.html.

Nover, D.M., Witt, J.W., Butcher, J.B., Johnson, T.E., and Weaver, C.P., 2016, The effects of downscaling method on the variability of simulated watershed response to climate change in five U.S. basins: Earth Interactions, v. 20, no. 11, p. 1–27, accessed July 7, 2022, at https://doi.org/10.1175/EI-D-15-0024.1.

Overeem, A., Buishand, A., and Holleman, I., 2008, Rainfall depth-duration-frequency curves and their uncertainties: Journal of Hydrology, v. 348, nos. 1–2, p. 124–134, accessed July 7, 2022, at https://doi.org/10.1016/j.jhydrol.2007.09.044.

Panofsky, H.W., and Brier, G.W., 1968, Some applications of statistics to meteorology: Philadelphia, Pennsylvania State University Press, 244 p.

Pavlovic, S., Perica, S., St. Laurent, M., and Mejía, A., 2016, Intercomparison of selected fixed-area areal reduction factor methods: Journal of Hydrology, v. 537, p. 419–430, accessed July 7, 2022, at https://doi.org/10.1016/j.jhydrol.2016.03.027.

Perica, S., Martin, D., Pavlovic, S., Roy, I., St. Laurent, M., Trypaluk, C., Unruh, D., Yekta, M., and Bonnin, G., eds., 2013, Precipitation-frequency atlas of the United States, southeastern States (ver. 2.0): National Weather Service, National Oceanic and Atmospheric Administration Atlas 14, v. 9, 163 p., accessed July 7, 2022, at https://www.weather.gov/media/owp/oh/hdsc/docs/Atlas14_Volume9.pdf.

Pickands, J., 1975, Statistical inference using extreme order statistics: Annals of Statistics, v. 3, no. 1, p. 119–131, accessed July 7, 2022, at https://doi.org/10.1214/aos/1176343003.

Pierce, D.W., 2025, LOCA statistical downscaling: Scripps Institute of Oceanography website, accessed February 13, 2026, at https://loca.ucsd.edu/.

Pierce, D.W., Cayan, D.R., Feldman, D.R., and Risser, M.D., 2023, Future increases in North American extreme precipitation in CMIP6 downscaled with LOCA: Journal of Hydrometeorology, v. 24, no. 5, p. 951–975, accessed July 27, 2023, at https://doi.org/10.1175/JHM-D-22-0194.1.

Pierce, D.W., Cayan, D.R., Maurer, E.P., Abatzoglou, J.T., and Hegewisch, K.C., 2015, Improved bias correction techniques for hydrological simulations of climate change: Journal of Hydrometeorology, v. 16, no. 6, p. 2421–2442, accessed July 7, 2022, at https://doi.org/10.1175/JHM-D-14-0236.1.

Pierce, D.W., Cayan, D.R., and Thrasher, B.L., 2014, Statistical downscaling using Localized Constructed Analogs (LOCA): Journal of Hydrometeorology, v. 15, no. 6, p. 2558–2585, accessed July 7, 2022, at https://doi.org/10.1175/JHM-D-14-0082.1.

Pierce, D.W., Su, L., Cayan, D.R., Risser, M.D., Livneh, B., and Lettenmaier, D.P., 2021, An extreme-preserving long-term gridded daily precipitation data set for the conterminous United States: Journal of Hydrometeorology, v. 22, no. 7, p. 1883–1895, accessed July 7, 2022, at https://doi.org/10.1175/JHM-D-20-0212.1.

Rahmstorf, S., Foster, G., and Cahill, N., 2017, Global temperature evolution—Recent trends and some pitfalls: Environmental Research Letters, v. 12, no. 5, article 054001, accessed July 7, 2022, at https://doi.org/10.1088/1748-9326/aa6825.

Rasmussen, K.L., Prein, A.F., Rasmussen, R.M., Ikeda, K., and Liu, C., 2020, Changes in the convective population and thermodynamic environments in convection-permitting regional climate simulations over the United States: Climate Dynamics, v. 55, nos. 1–2, p. 383–408, accessed July 7, 2022, at https://doi.org/10.1007/s00382-017-4000-7.

R Core Team, 2020, R—A language and environment for statistical computing: Vienna, Austria, R Foundation for Statistical Computing software release, accessed July 7, 2022, at https://www.R-project.org/.

Reed, K.A., Stansfield, A.M., Wehner, M.F., and Zarzycki, C.M., 2020, Forecasted attribution of the human influence on Hurricane Florence: Science Advances, v. 6, no. 1, article eaaw9253, accessed July 7, 2022, at https://doi.org/10.1126/sciadv.aaw9253.

Reed, K.A., and Wehner, M.F., 2023, Real-time attribution of the influence of climate change on extreme weather events—A storyline case study of Hurricane Ian rainfall: Environmental Research, Climate, v. 2, no. 4, article 043001, accessed July 17, 2024, at https://doi.org/10.1088/2752-5295/acfd4e.

Ren, H., Hou, Z.J., Wigmosta, M., Liu, Y., and Leung, L.R., 2019, Impacts of spatial heterogeneity and temporal non-stationarity on intensity-duration-frequency estimates—A case study in a mountainous California-Nevada watershed: Water (Basel), v. 11, no. 6, article 1296, accessed July 7, 2022, at https://doi.org/10.3390/w11061296.

Riahi, K., van Vuuren, D.P., Kriegler, E., Edmonds, J., O’Neill, B.C., Fujimori, S., Bauer, N., Calvin, K., Dellink, R., Fricko, O., Lutz, W., Popp, A., Cuaresma, J.C., Kc, S., Leimbach, M., Jiang, L., Kram, T., Rao, S., Emmerling, J., Ebi, K., Hasegawa, T., Havlik, P., Humpenöder, F., Da Silva, L.A., Smith, S., Stehfest, E., Bosetti, V., Eom, J., Gernaat, D., Masui, T., Rogelj, J., Strefler, J., Drouet, L., Krey, V., Luderer, G., Harmsen, M., Takahashi, K., Baumstark, L., Doelman, J.C., Kainuma, M., Klimont, Z., Marangoni, G., Lotze-Campen, H., Obersteiner, M., Tabeau, A., and Tavoni, M., 2017, The shared socioeconomic pathways and their energy, land use, and greenhouse gas emissions implications—An overview: Global Environmental Change, v. 42, p. 153–168, accessed July 1, 2024, at https://doi.org/10.1016/j.gloenvcha.2016.05.009.

Rigby, R.A., and Stasinopoulos, D.M., 2005, R package gamlss—Generalized additive models for location, scale and shape (ver. 5.2.0): R Foundation for Statistical Computing software release, accessed July 7, 2022, at https://cran.r-project.org/web/packages/gamlss/index.html.

Schurer, A.P., Mann, M.E., Hawkins, E., Tett, S.F.B., and Hegerl, G.C., 2017, Importance of the pre-industrial baseline for likelihood of exceeding Paris goals: Nature Climate Change, v. 7, no. 8, p. 563–567, accessed August 1, 2022, at https://doi.org/10.1038/nclimate3345.

Seneviratne, S.I., Nicholls, N., Easterling, D., Goodess, C.M., Kanae, S., Kossin, J., Luo, Y., Marengo, J., McInnes, K., Rahimi, M., Reichstein, M., Sorteberg, A., Vera, C., and Zhang, X., 2012, Changes in climate extremes and their impact on the natural physical environment, *in* Field, C.B., Barros, V., Stocker, T.F., Qin, D., Dokken, D.J., Ebi, K.L., Mastrandrea, M.D., Mach, K.J., Plattner, G.-K., Allen, S.K., Tignor, M., and Midgley, P.M., eds., Managing the Risks of Extreme Events and Disasters to Advance Climate Change Adaptation—A Special Report of Working Groups I and II of the Intergovernmental Panel on Climate Change (IPCC): Cambridge, United Kingdom, and New York, Cambridge University Press, p. 109–230, accessed February 6, 2026, at https://doi.org/10.1017/CBO9781139177245.

Serinaldi, F., and Kilsby, C.G., 2014, Rainfall extremes—Toward reconciliation after the battle of distributions: Water Resources Research, v. 50, no. 1, p. 336–352, accessed July 7, 2022, at https://doi.org/10.1002/2013WR014211.

Serinaldi, F., and Kilsby, C.G., 2015, Stationarity is undead—Uncertainty dominates the distribution of extremes: Advances in Water Resources, v. 77, p. 17–36, accessed July 7, 2022, at https://doi.org/10.1016/j.advwatres.2014.12.013.

Sheffield, J., Goteti, G., and Wood, E.F., 2006, Development of a 50-year high-resolution global dataset of meteorological forcings for land surface modeling: Journal of Climate, v. 19, no. 13, p. 3088–3111, accessed August 2, 2025, at https://doi.org/10.1175/JCLI3790.1.

South Florida Water Management District [SFWMD], 2005, Documentation of the South Florida Water Management Model—Version 5.5: South Florida Water Management District, 325 p., accessed July 7, 2022, at https://www.sfwmd.gov/sites/default/files/documents/sfwmm_final_121605.pdf.

South Florida Water Management District [SFWMD], 2016, Environmental resource permit applicant's handbook—Volume 2: South Florida Water Management District, 58 p., accessed February 12, 2026, at https://www.sfwmd.gov/sites/default/files/documents/swerp_applicants_handbook_vol_ii.pdf.

South Florida Water Management District [SFWMD], 2020, DBHYDRO browser user's guide, September 2020 (revised): South Florida Water Management District, 102 p., accessed February 12, 2026, at https://www.sfwmd.gov/sites/default/files/documents/dbhydrobrowseruserdocumentation.pdf.

St. Johns River Water Management District, 2018, Permit information manual: St. Johns River Water Management District, 652 p., accessed February 12, 2026, at https://www.sjrwmd.com/static/permitting/PIM-20180601.pdf.

Sillmann, J., Kharin, V.V., Zhang, X., Zwiers, F.W., and Bronaugh, D., 2013a, Climate extremes indices in the CMIP5 multimodel ensemble—Part 1. Model evaluation in the present climate: Journal of Geophysical Research, Atmospheres, v. 118, no. 4, p. 1716–1733, accessed July 7, 2022, at https://doi.org/10.1002/jgrd.50203.

Sillmann, J., Kharin, V.V., Zwiers, F.W., Zhang, X., and Bronaugh, D., 2013b, Climate extremes indices in the CMIP5 multimodel ensemble—Part 2. Future climate projections: Journal of Geophysical Research, Atmospheres, v. 118, no. 6, p. 2473–2493, accessed July 7, 2022, at https://doi.org/10.1002/jgrd.50188.

Simmons, A., Uppala, S., Dee, D., and Kobayashi, S., 2007, ERA-Interim—New ECMWF reanalysis products from 1989 onwards: European Centre for Medium-Range Weather Forecasts, ECMWF Newsletter, v. 110, p. 25–35, accessed July 7, 2022, at https://doi.org/10.21957/pocnex23c6.

Skamarock, W.C., Klemp, J.B., Dudhia, J., Gill, D.O., Liu, Z., Berner, J., Wang, W., Powers, J.G., Duda, M.G., Barker, D.M., and Huang, X.-Y., 2019, A description of the Advanced Research WRF version 4: National Center for Atmospheric Research, NCAR Technical Notes, NCAR/TN–556+STR, 145 p., accessed July 7, 2022, at https://doi.org/10.5065/1dfh-6p97.

Srivastava, A., Grotjahn, R., and Ullrich, P.A., 2020, Evaluation of historical CMIP6 model simulations of extreme precipitation over contiguous US regions: Weather and Climate Extremes, v. 29, article 100268, accessed July 7, 2022, at https://doi.org/10.1016/j.wace.2020.100268.

Srivastava, A.K., Grotjahn, R., Ullrich, P.A., and Zarzycki, C., 2022, Evaluation of precipitation indices in suites of dynamically and statistically downscaled regional climate models over Florida: Climate Dynamics, v. 58, nos. 5–6, p. 1587–1611, accessed July 7, 2022, at https://doi.org/10.1007/s00382-021-05980-w.

Taylor, K.E., Stouffer, R.J., and Meehl, G.A., 2012, An overview of CMIP5 and the experiment design: Bulletin of the American Meteorological Society, v. 93, no. 4, p. 485–498, accessed July 7, 2022, at https://doi.org/10.1175/BAMS-D-11-00094.1.

Taylor, M.A., Clarke, L.A., Centella, A., Bezanilla, A., Stephenson, T.S., Jones, J.J., Campbell, J.D., Vichot, A., and Charlery, J., 2018, Future Caribbean climates in a world of rising temperatures—The 1.5 vs 2.0 dilemma: Journal of Climate, v. 31, no. 7, p. 2907–2926, accessed July 7, 2022, at https://doi.org/10.1175/JCLI-D-17-0074.1.

Terando, A., Reidmiller, D., Hostetler, S.W., Littell, J.S., Beard, T.D., Jr., Weiskopf, S.R., Belnap, J., and Plumlee, G.S., 2020, Using information from global climate models to inform policymaking—The role of the U.S. Geological Survey: U.S. Geological Survey Open-File Report 2020–1058, 25 p., accessed July 7, 2022, at https://doi.org/10.3133/ofr20201058.

Thornton, P.E., Thornton, M.M., Mayer, B.W., Wei, Y., Devarakonda, R., Vose, R.S., and Cook, R.B., 2016, Daymet-Daily surface weather data on a 1-km grid for North America, version 3: Oak Ridge, Tenn., Oak Ridge National Laboratory Distributed Active Archive Center (ORNL DAAC) database, accessed January 31, 2022, at https://doi.org/10.3334/ORNLDAAC/1328. [Data available at https://daac.ornl.gov/cgi-bin/dsviewer.pl?ds_id=1328.]

Thrasher, B., Maurer, E.P., McKellar, C., and Duffy, P.B., 2012, Technical note—Bias correcting climate model simulated daily temperature extremes with quantile mapping: Hydrology and Earth System Sciences, v. 16, no. 9, p. 3309–3314, accessed May 31, 2023, at https://doi.org/10.5194/hess-16-3309-2012.

Thrasher, B., Wang, W., Michaelis, A., Melton, F., Lee, T., and Nemani, R., 2022, NASA Global Daily Downscaled Projections, CMIP6: Scientific Data, v. 9, no. 1, article 262, accessed May 30, 2023, at https://doi.org/10.1038/s41597-022-01393-4.

Thrasher, B., Wang, W., Michaelis, A., and Nemani, R., 2021, NEX-GDDP-CMIP6: National Aeronautics and Space Administration (NASA) Center for Climate Simulation web page, accessed June 6, 2022, at https://doi.org/10.7917/OFSG3345.

Ullrich, P., 2023, Validation of LOCA2 and STAR-ESDM statistically downscaled products: Lawrence Livermore National Laboratory, Program for Climate Model Diagnosis and Intercomparison, 20 p., https://eesm.science.energy.gov/sites/default/files/2023-10/Validation%20of%20LOCA2%20and%20STAR-ESDM%20Statistically%20Downscaled%20Products.pdf.

University of California Merced, 2026, Multivariate Adaptive Constructed Analog (MACA) datasets: University of California Merced website, accessed February 13, 2026, at https://climate.northwestknowledge.net/MACA/index.php.

University of Florida IFAS Extension, 2026, FAWN Florida Automated Weather Network: University of Florida IFAS Extension website, accessed February 13, 2026, at https://fawn.ifas.ufl.edu/.

U.S. Geological Survey Center for Integrated Data Analytics [USGS CIDA], 2024, USGS Geo Data Portal and THREDDS data server retirement: U.S. Geological Survey web page, accessed February 17, 2026, at https://waterdata.usgs.gov/blog/gdp-moving.

Ushey, K., 2018, R package RcppRoll—Efficient rolling/windowed operations (ver. 0.3.0): R Foundation for Statistical Computing software release, accessed July 7, 2022, at https://cran.r-project.org/web/packages/RcppRoll/index.html.

van Vuuren, D.P., Edmonds, J., Kainuma, M., Riahi, K., Thomson, A., Hibbard, K., Hurtt, G.C., Kram, T., Krey, V., Lamarque, J.F., Masui, T., Meinshausen, M., Nakicenovic, N., Smith, S.J., and Rose, S.K., 2011, The representative concentration pathways—An overview: Climatic Change, v. 109, no. 5, p. 5–31, accessed March 18, 2026, at https://doi.org/10.1007/s10584-011-0148-z.

Vogel, R.M., and Fennessey, N.M., 1993, *L* moment diagrams should replace product moment diagrams: Water Resources Research, v. 29, no. 6, p. 1745–1752, accessed July 7, 2022, at https://doi.org/10.1029/93WR00341.

Wallace, J.M., and Hobbs, P.V., 2006, Atmospheric science—An introductory survey (2d ed.): New York, Elsevier, 483 p.

Walton, D.B., Sun, F., Hall, A., and Capps, S., 2015, A hybrid dynamical–statistical downscaling technique—Part I. Development and validation of the technique: Journal of Climate, v. 28, no. 12, p. 4597–4617, accessed July 7, 2022, at https://doi.org/10.1175/JCLI-D-14-00196.1.

Wang, D., Hagen, S.C., and Alizad, K., 2013, Climate change impact and uncertainty analysis of extreme rainfall events in the Apalachicola River basin, Florida: Journal of Hydrology, v. 480, p. 125–135, accessed July 7, 2022, at https://doi.org/10.1016/j.jhydrol.2012.12.015.

Wang, G., Kirchhoff, C.J., Seth, A., Abatzoglou, J.T., Livneh, B., Pierce, D.W., Fomenko, L., and Ding, T., 2020, Projected changes of precipitation characteristics depend on downscaling method and training data—MACA versus LOCA using the U.S. Northeast as an example: Journal of Hydrometeorology, v. 21, no. 12, p. 2739–2758, accessed July 7, 2022, at https://doi.org/10.1175/JHM-D-19-0275.1.

Weiss, L.L., 1964, Ratio of true to fixed-interval maximum rainfall: Journal of the Hydraulics Division, v. 90, no. 1, p. 77–82, accessed July 7, 2022, at https://doi.org/10.1061/JYCEAJ.0001008.

Wilby, R.L., and Wigley, T.M.L., 1997, Downscaling general circulation model output—A review of methods and limitations: Progress in Physical Geography, v. 21, no. 4, p. 530–548, accessed July 7, 2022, at https://doi.org/10.1177/030913339702100403.

Wilby, R.L., Wigley, T.M.L., Conway, D., Jones, P.D., Hewitson, B.C., Main, J., and Wilks, D.S., 1998, Statistical downscaling of general circulation model output—A comparison of methods: Water Resources Research, v. 34, no. 11, p. 2995–3008, accessed July 7, 2022, at https://doi.org/10.1029/98WR02577.

Winsberg, M.D., 2020, Anticipating heavy rain in Florida: Tallahassee, Fla., Florida State University, Florida Climate Center web page, accessed December 21, 2020, at https://climatecenter.fsu.edu/topics/specials/anticipating-heavy-rain-in-florida.

Wood, A.W., Leung, L.R., Sridhar, V., and Lettenmaier, D.P., 2004, Hydrologic implications of dynamical and statistical approaches to downscaling climate model outputs: Climatic Change, v. 62, nos. 1–3, p. 189–216, accessed May 30, 2023, at https://doi.org/10.1023/B:CLIM.0000013685.99609.9e.

Wood, A.W., Maurer, E.P., Kumar, A., and Lettenmaier, D.P., 2002, Long-range experimental hydrologic forecasting for the eastern United States: Journal of Geophysical Research, Atmospheres, v. 107, no. D20, p. ACL 6-1–ACL 6-15, accessed May 30, 2023, at https://doi.org/10.1029/2001JD000659.

Wootten, A.M., 2018, The subtle processes in statistical downscaling and the potential uncertainty: U.S. Climate Variability and Predictability (CLIVAR) Project Office, Variations, v. 16, no. 3, p. 8–13, accessed July 7, 2022, at https://doi.org/10.5065/D62N513R.

Wootten, A.M., Dixon, K.W., Adams-Smith, D.J., and McPherson, R.A., 2021, Statistically downscaled precipitation sensitivity to gridded observation data and downscaling technique: International Journal of Climatology, v. 41, no. 2, p. 980–1001, accessed July 7, 2022, at https://doi.org/10.1002/joc.6716.

World Meteorological Organization, 2009, Guidelines on analysis of extremes in a changing climate in support of informed decisions for adaptation: World Meteorological Organization, Climate Data and Monitoring WCDMP–No. 72, 55 p., accessed July 7, 2022, at https://www.ecad.eu/documents/WCDMP_72_TD_1500_en_1.pdf.

Wuebbles, D., Meehl, G., Hayhoe, K., Karl, T.R., Kunkel, K., Santer, B., Wehner, M., Colle, B., Fischer, E.M., Fu, R., Goodman, A., Janssen, E., Kharin, V., Lee, H., Li, W., Long, L.N., Olsen, S.C., Pan, Z., Seth, A., Sheffield, J., and Sun, L., 2014, CMIP5 climate model analyses—Climate extremes in the United States: Bulletin of the American Meteorological Society, v. 95, no. 4, p. 571–583, accessed July 7, 2022, at https://doi.org/10.1175/BAMS-D-12-00172.1.

Zhang, X., Alexander, L., Hegerl, G.C., Jones, P., Tank, A.K., Peterson, T.C., Trewin, B., and Zwiers, F.W., 2011, Indices for monitoring changes in extremes based on daily temperature and precipitation data: Wiley Interdisciplinary Reviews, Climate Change, v. 2, no. 6, p. 851–870, accessed July 7, 2022, at https://doi.org/10.1002/wcc.147.

**For more information about this publication, contact**
Director, Caribbean-Florida Water Science Center
U.S. Geological Survey
7595 SW 33d St.
Davie, FL 33314

For additional information, visit
https://www.usgs.gov/centers/car-fl-water

Publishing support provided by
U.S. Geological Survey Science Publishing Network,
Lafayette Publishing Service Center

Irizarry-Ortiz—**Development of Projected Depth-Duration-Frequency Curves for Precipitation in Florida, 2020–59 and 2050–89**—SIR 2025–5111

ISSN 2328-0328 (online)
https://doi.org/10.3133/sir20255111